# Ferrocene Functionalized Chiral Amines: Synthesis, Characterization, *In-silico* study and Evaluation of as Cytotoxic Agents

## Abstract


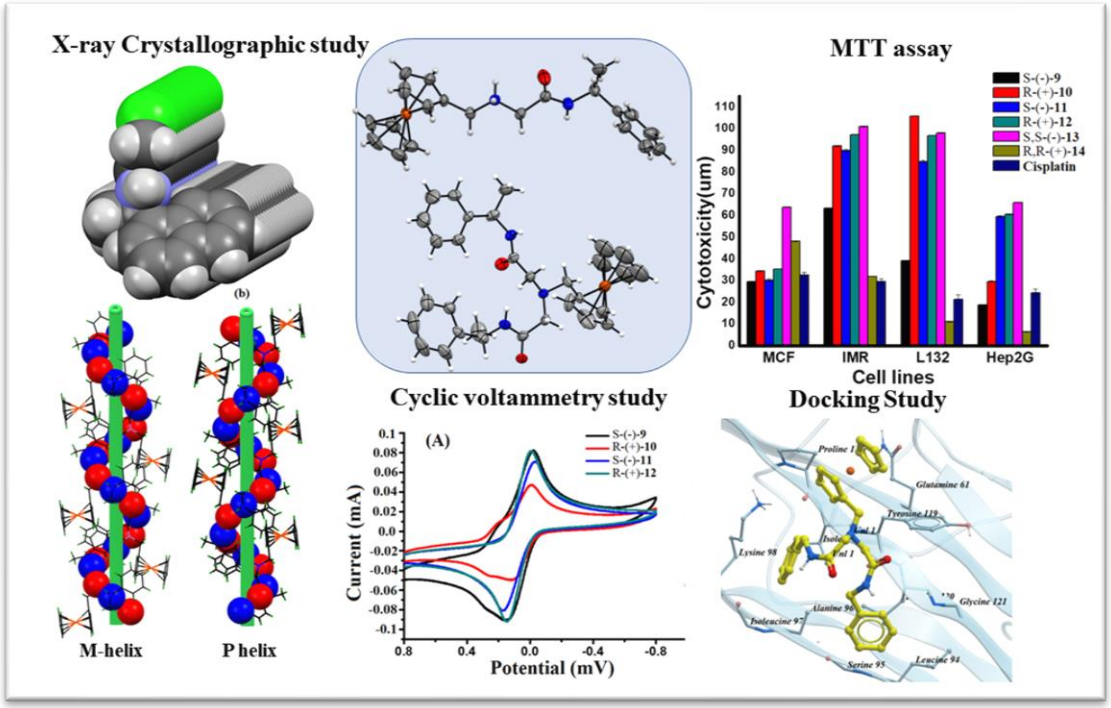


Ferrocene functionalized chiral secondary and tertiary amines S-(-)-**9,** R-(+)-**10,** S-(-)-**11,** R-(+)-**12,** S,S-(-)-**13** and R,R-(+)-**14** have been synthesized from ferrocenylmethylamine to probe the influence of chirality and the redox potential on their anti-proliferative activity. Compounds were characterized by microanalysis, $^{1}H$, $^{13}C$ NMR, UV-visible, fluorescence, FTIR, thermogravimetric and crystallographic techniques. The single crystal X-ray diffraction (SCXRD) study revealed that the molecules of R-(+)-**10** holding R chirality **,** S,S-(-)-**13** holding S, S-chirality at benzylic carbons forms a fascinating *M*-helix while R,R-(+)-**14** holding R,R-chirality at benzylic carbons forms *P*-helix by involving intra- and intermolecular H-bonding interactions as verified by Hirshfeld surface analysis. Chirality-related influence was observed on the antiproliferative activity of enantiomeric pair and at the supramolecular level. For instance, enantiomer R,R-(+)-**14** is found to be highly active against all the investigated human carcinoma cell lines MCF 7, IMR 32,

HepG2, and immortal L132 cell lines. In particular, R,R-(+)-**14** exhibited more than 10 folds better antiproliferation (IC $_{50}$: 6.35±0.19 μM) than other enantiomer S,S-(-)-**13 (**$IC_{50}$: 65.96±0.12 μM**)** and four folds better activity than highly successful anticancer drug, cisplatin ($IC_{50}$: 24.3±1.7 μM) against Hep G2 cell line. R-enantiomers are found to be superior than S-enantiomers against all the studied cell lines MCF 7, IMR 32, HepG2 and immortal L132. Particularly, secondary amines R-(+)-**10** has shown optimum activity against MCF 7 (IC $_{50}$: 31.38±0.24 μM) and HepG2 (IC $_{50}$: 18.78±0.14 μM) and these are found to be superior than cisplatin. The electrochemical, DFT calculations and molecular docking study have been performed to justify the experimental outcomes.

## 3.1 Introduction

The interest in developing novel organic,[1] inorganic[2] and organometallic[3] compounds as antitumor agents has been continued because cancer has become the second leading cause of death globally and this burden continues to increase day by day. An estimated 9.6 million deaths have been recorded due to cancer in the year 2018.[4] This has created a growing interest to explore chiral metal-based drugs with their unique properties and potential selectivity toward nucleic acids and protein based chiral biomolecules.[5] Chirality has become an important tool in modern drug development because one of the enantiomers may be beneficial, while other may be harmful and thus their therapeutic activity can differ severely in terms of toxicity and pharmacokinetics.[6] For instance, a Pt(II) antineoplastic drug in clinical use "oxaliplatin" contains the chiral ligand (R, R)-cyclohexane-1,2-diamine showed more biological activity and chemical reactivity than its enantiomer containing the ligand (S, S)-cyclohexane-1, 2-diamine.[7] There has been an immense increase in the research on chiral metal-based compounds for anticancer application, in recent years. [8] Along the line, ferrocene containing compounds have been emerged as a novel class of anticancer drugs. To attain better medicinal properties, biologically relevant groups have been methodically attached into the cyclo-pentadienyl ring of ferrocene,[9] which may offer chirality into the molecule, or chemotherapeutic agents were attached to the ferrocene moiety. [10] For instance, Kater et al. have reported enantiomerically pure ferrocene–amino acid derivative showing a pronounced

anticancer activity against leukemia and lymphoma cancer cell lines, which has overcome multiple drug resistance. [11]

Recently, we have tested the scope of a new series of analogous achiral tertiary amines for apoptotic potentials against various human cancer cell lines in low μM concentration. Further, the apoptotic regulatory influence of various substituents at the amidic nitrogen of these compounds on TNFα inhibition discloses an optimal substitution of *N*-benzyl group. [9a] Thus, a remarkable increase in anticancer activity with benzyl swapped at the amidic nitrogen of analogous achiral tertiary amines has encouraged us to carry out further structural modification by introducing chirality at the benzylic carbon to achieve chiral secondary and tertiary amines enantiomeric pair S-(-)-**9** and R-(+)-**10,** S-(-)-**11** and R-(+)-**12,** S,S-(-)-**13** and R,R-(+)-**14**. In the light of the fact that DNA is chiral by itself and by anticipating our enantiomeric pair to operate by a pathway similar to that of chiral-drug, [7a] we selected to probe the influence of chirality on anticancer properties.

This work presents the synthesis of optically pure enantiomeric pair *viz.* ferrocene functionalized secondary and tertiary amines enantiomeric pair S-(-)-**9** and R-(+)-**10,** S-(-)-**11** and R-(+)-**12,** S,S-(-)-**13** and R,R-(+)-**14** synthesized from ferrocenylmethylamine. Compounds were characterized by microanalysis, $^{1}H$, $^{13}C$ NMR, UV-visible, fluorescence, FTIR, thermogravimetric and crystallographic techniques. Chirality-dependent formation of left- (M type) and right- (P type) handed helices, confirmed by SCXRD, and its dependency on the antiproliferative activity of enantiomeric pair was verified by MTT assay. The results on anticancer potential of enantiomers have been well supported by molecular docking, DFT and electrochemical study. The synthesized enantiomer R,R-(+)-**14** contained an optimal anticancer potential in low micro molar concentration. This allows us to probe the chirality-influence on anticancer potentials of enantiomers and their secondary interactions with the 2AZ5 and 1TNF proteins.

## 3.2 Experimental

### 3.2.1 General procedure for the synthesis of (S/R) -2- chloro-N-(1-phenylethyl)acetamide and (S/R)-2-chloro-N-(1-(naphthalen-1-yl)ethyl)acetamide (1-4)

Solid $NaHCO_3$ (0.252mg, 3 mmol) was added to a clear solution of (S)-1-phenylethan-1-amine (127 µl , 1 mmol, density 0.95 g/cm$^3$), (R)-1-phenylethan-1-amine(127 µl , 1 mmol, density 0.95 g/cm$^3$), (S)-1-(naphthalen-1-yl)ethan-1-amine(160 µl, 1 mmol, density 1.067 g/cm$^3$) and (R)-1-(naphthalen-1-yl)ethan-1-amine(160 µl, 1 mmol, density 1.067 g/cm$^3$) in chloroform and the reaction mixture was stirred for 30 minutes. To this solution, 2-chloroacetyl chloride (159 µl, 2 mmol) was added carefully at 0 ˚C over a period of 1 hour and then allowed to stir at room temperature for 3-4 hours. The progress of reaction was monitored by TLCs. The reaction mixture was dried under high vacuum and product are extract with ethyl acetate to yield the white coloured (S) -2- chloro-N-(1-phenylethyl)acetamide, (R) -2-chloro-N-(1-phenylethyl)acetamide, (S)-2-chloro-N-(1-(naphthalen-1-yl)ethyl)acetamide and (R)-2-chloro-N-(1-(naphthalen-1-yl)ethyl)acetamide Yield is 90-95 %.

### 3.2.2 General procedure for the synthesis of (S/R) -2- iodo-N-(1-phenylethyl)acetamide and (S/R)-2-iodo-N-(1-(naphthalen-1-yl)ethyl)acetamide (5-8)

(S) -2- chloro-N-(1-phenylethyl)acetamide (197mg, 1mmol), (R) -2-chloro-N-(1-phenylethyl)acetamide (197mg, 1mmol), (S)-2-chloro-N-(1-(naphthalen-1-yl)ethyl)acetamide (247mg, 1mmol) and (R)-2-chloro-N-(1-(naphthalen-1-yl)ethyl)acetamide (247mg, 1mmol) are dissolved in acetone and added KI (332mg,1.5mmol) then reaction mixture was reflux in oil bath at 80-100 ˚C. The progress of reaction was monitored by TLC. After Complete reaction mixture was cool down up to room temperature then dried and extracted with ethyl acetate to yield the light yellow coloured products (S) -2- iodo-N-(1-phenylethyl)acetamide, (R) -2-iodo-N-(1-phenylethyl)acetamide (S)-2-iodo-N-(1-(naphthalen-1-yl)ethyl)acetamide and (R)-2-iodo-N-(1-(naphthalen-1-yl)ethyl)acetamide in 80-90 Yield %.

### 3.2.3 General procedure for the synthesis of (R/S) 2-(ferrocenylmethylamino)-N-alrylacetamide (9-12)

The synthesis of corresponding (R/S) 2-(ferrocenylmethylamino)-N-alrylacetamide (9-12) ca (S)-2-iodo-N-(1-phenylethyl)acetamide (0.304 g, 1.05 mmol), (R)-2-iodo-N-(1-phenylethyl)acetamide (0.304 g, 1.05 mmol), (S)-2-iodo-N-

(1-(naphthalen-1-yl)ethyl)acetamide (0.356 g, 1.05 mmol) and (R)-2-iodo-N-(1-(naphthalen-1-yl)ethyl)acetamide (0.356 g, 1.05 mmol) was added portion wise to the solution of amino methyl ferrocene (0.215 g, 1.0 mmol) in 25 ml of $CHCl_3$ containing 3-4 drops of $Et_3N$. The reaction mixture was reflux for 3 hours. The progress of the reaction was monitored by thin layer chromatography and ninhydrin. The reaction mixture was cooled at room temperature and solvent was removed under vacuum. Distilled water was added in the solid residue and the crude product was extracted by using dichloromethane. It was dried over $Na_2SO_4$ for 4 hours and the solvent was removed by rotator evaporator. The residue was column chromatographed to give pale yellow-coloured thick liquid products in 60-70 % yield. The reaction could not complete even after prolonged refluxing which leads to decomposition.

### 3.2.4 General procedure for the synthesis of (R/S) 2, 2'-(ferrocenylmethylazanediyl)bis(N-benzyl acetamide) (13-14)

(S)-2-iodo-N-(1-phenylethyl)acetamide (0.608 g, 2.1 mmol), (R)-2-iodo-N-(1-phenylethyl)acetamide (0.608 g, 2.1 mmol), (S)-2-iodo-N-(1-(naphthalen-1-yl)ethyl)acetamide (0.712 g, 2.1 mmol) and (R)-2-iodo-N-(1-(naphthalen-1-yl)ethyl)acetamide (0.712 g, 2.1 mmol) was added portion wise to the solution of amino methyl ferrocene (0.215 g, 1 mmol) in 25 ml of $CH_3CN$ containing $Na_2CO_3$ (0.265g, 2.5 mmol) but (S)-2-iodo-N-(1-(naphthalen-1-yl)ethyl)acetamide and (R)-2-iodo-N-(1-(naphthalen-1-yl)ethyl)acetamide not completely consumed so not formed treasury amine because naphthyl is bulky group. The reaction mixture was reflux for 6 hours. The similar workup procedure was adopted as descried earlier to give yellow-coloured solid products in 85-90 % yield. This is outlined in scheme1.

**Table 1.** Micro-, mass- and IR analysis data for compounds **5-14**.

| Entry | Molecular Formula | Molecular Weight | Yield (%) | MP (°C) | Elemental Analysis % Found (calculated) | | | IR data (KBr disc) $\upsilon_{max}$/cm$^{-1}$ |
|---|---|---|---|---|---|---|---|---|
| | | | | | C | H | N | |
| **(S)-(-)-5** | $C_{10}H_{12}INO$ | 289 | 85 | 121 | 41.54<br>41.20 | 4.18<br>4.38 | 4.84<br>4.98 | 3276 (N-H), 3067 (C-H), 3024 (C-H), 1633 (C=O), 1542, 1448, 1423, 1170, 970, 789, 697 |
| **(R)-(+)-6** | $C_{10}H_{12}INO$ | 289 | 87 | 121 | 41.54<br>41.27 | 4.18<br>4.40 | 4.84<br>4.96 | 3264 (N-H), 3057(C-H), 3024(C-H), 1633(C=O), 1545, 1445, 1417, 1169, 969, 751, 696 |
| **(S)-(-)-7** | $C_{14}H_{14}INO$ | 339 | 89 | 129 | 49.58<br>49.96 | 4.16<br>4.29 | 4.13<br>4.29 | 3293(N-H), 3021(C-H), 2973(C-H), 1632(C=O), 1537, 1449, 1416, 1170, 779 |
| **(R)-(+)-8** | $C_{14}H_{14}INO$ | 339 | 89 | 129 | 49.58<br>49.89 | 4.16<br>4.27 | 4.13<br>4.35 | 3293(N-H), 3021(C-H), 2972(C-H), 1633(C=O), 1537, 1449, 1416, 1170, 779 |
| **(S)-(-)-9** | $C_{21}H_{24}FeN_2O$ | 376 | 89 | - | 67.03<br>68.29 | 6.43<br>6.29 | 7.44<br>7.59 | 3240(N-H), 3055 (C-H), 1643 (C=O), 1550, 1442, 1242, 1126 |
| **(R)-(+)-10** | $C_{21}H_{24}FeN_2O$ | 376 | 90 | - | 67.03<br>68.51 | 6.43<br>6.29 | 7.44<br>7.59 | 3240(N-H), 2939(C-H), 1651 (C=O), 1597, 1384, 1234, 1103 |
| **(S) -(-)-11** | $C_{25}H_{26}FeN_2O$ | 429 | 87 | - | 70.43<br>70.48 | 6.15<br>6.19 | 6.57<br>6.85 | 3276 (N-H), 3049 (C-H), 2974 (C-H), 1650 (C=O), 1525, 1238, 1123 |
| **(R)-(+)-12** | $C_{25}H_{26}FeN_2O$ | 429 | 85 | - | 70.43<br>70.35 | 6.15<br>6.15 | 6.57<br>6.75 | 3273 (N-H), 3048 (C-H), 2974 (C-H), 1649 (C=O), 1512, 1238, 1123, 1104 |
| **(S, S)-(-)-13** | $C_{31}H_{35}FeN_3O_2$ | 537 | 89 | 141 | 69.27<br>69.51 | 6.56<br>6.28 | 7.82<br>7.65 | 3240 (N-H), 1666(C=O), 1639 (C=O), 1543, 1238, 1103, 1022 |
| **(R, R)-(+)-14** | $C_{31}H_{35}FeN_3O_2$ | 537 | 90 | 142 | 69.27<br>69.47 | 6.56<br>6.65 | 7.82<br>7.56 | 3240 (N-H), 3032(C-H), 2924(C-H), 1658(C=O), 1639 (C=O), 1550, 1242, 1103, 1022 |

**Table 2.** NMR spectral data for compounds **5-14**.

| Entry | NMR Data (ppm) | |
|---|---|---|
| | **$^{1}$H NMR ($CDCl_3$)** | **$^{13}$C NMR ($CDCl_3$)** |
| **(S)-(-)-5** | 7.26-7.38(m, 5H, Ph); 6.60(s, 1H, -N*H*CO); 5.00(m, 1H, -C*H*); 3.67(s, 2H, -C$H_2$CO); 1.49(s, 3H, -C$H_3$). | 166.4, 142.5, 128.5, 127.5, 126.1, 49.7, 21.5 |
| **(R)-(+)-6** | 7.27-7.38(m, 5H, Ph); 6.65(s, 1H, -N*H*CO); 5.06(m, 1H, -C*H*); 3.67(s, 2H, -C$H_2$CO); 1.49(s, 3H, -C$H_3$) | 166.4, 142.5, 128.7, 127.5, 126.1, 49.76, 21.56 |
| **(S)-(-)-7** | 7.28-8.07(m, 5H, Ph); 6.31(s, 1H, -N*H*CO); 5.88(m, 1H, -C*H*); 3.67(s, 2H, -C$H_2$CO); 1.69(s, 3H, -C$H_3$) | 165.9, 137.5, 133.9, 131.0, 128.8, 126.7, 125.2, 123.3, 122.5, 45.7, 20.3 |
| **(R)-(+)-8** | 7.28-8.06(m, 5H, Ph); 6.38(s, 1H, -N*H*CO); 5.87(m, 1H, -C*H*); 3.65(s, 2H, -C$H_2$CO); 1.69(s, 3H, -C$H_3$) | 165.9, 137.4, 133.9, 131.0, 128.8, 126.7, 125.2, 123.3, 122.5, 45.7, 20.3 |
| **(S)-(-)-9** | 7.57(s, 1H, -N*H*CO); 7.26-7.58 (m, 5H, Ph); 5.12(m, 1H, -*CH*); 4.07-4.17 (m, 9H, *Fc*); 3.53(s, 2H, -C$H_2$*CO*); 3.36 (2H, s, –C$H_2$ Fc); 2.04(s, 1H, -N*H*); 1.42(s, 3H, -C$H_3$). | 169.8, 143.2, 128.7, 128.6, 127.4, 126.1 68.3, 68.6, 58.3, 51.4, 48.5, 21.8 |
| **(R)-(+)-10** | 7.56(s, 1H, -N*H*CO); 7.26-7.37 (m, 5H, Ph); 5.12(m, 1H,-*CH*); 4.13-4.19 (m, 9H, *Fc*); 3.57(s, 2H, -C$H_2$*CO*); 3.39 (2H, s, –C$H_2$ Fc); 2.06(s, 1H, -N*H*); 1.49(s, 3H, -C$H_3$) | 169.1, 143.1, 128.7, 127.46, 126.1 69.9, 68.7, 58.1, 51.1, 48.5, 21.8. |
| **(S) -(-)-11** | 7.28-8.06 (m, 7H); 6.75(s, 1H, -N*H*CO); 5.83(m, 1H, -*CH*); 3.85-3.98 (m, 9H, *Fc*); 3.22(s, 2H, -C$H_2$*CO*); 3.19(2H, s, –C$H_2$ Fc); 2.06(s, 1H, -N*H*); 1.38(s, 3H, -C$H_3$). | 168.8, 138.1, 133.9, 131.0, 128.9, 126.7, 125.2, 123.5, 122.6, 69.9, 68.6, 58.2, 54.8, 44.0, 29.7 |
| **(R)-(+)-12** | 7.28-8.06 (m, 7H); 6.74(s, 1H, -N*H*CO); 5.84(m, 1H, -*CH*); 3.85-3.98 (m, 9H, *Fc*); 3.25(s, 2H, -C$H_2$*CO*); 3.18(2H, s, –C$H_2$ Fc); 2.05(s, 1H, -N*H*); 1.38(s, 3H, -C$H_3$). | 168.8, 138.0, 133.9, 131.4, 128.9, 126.7, 125.0, 123.2, 122.5, 81.3, 69.9, 68.6, 58.2, 54.9, 43.9, 20.3 |
| **(S, S)-(-)-13** | 7.28-7.35 (m, 10H, Ph); 6.84(s, 2H, -N*H*CO); 5.13(m, 2H, -*CH*); 4.07-4.54 (m, 9H, *Fc*); 3.52(s, 4H, -C$H_2$*CO*); 3.18 (2H, s, –C$H_2$ Fc); 1.42(s, 6H, -C$H_3$) | 168.1, 143.1, 128.7, 127.4, 126.1, 69.9, 68.8, 58.2, 55.2, 48.5, 21.8 |
| **(R, R)-(+)-14** | 7.28-7.37 (m, 10H, Ph); 6.80(s, 2H, -N*H*CO); 5.12(m, 2H, -*CH*); 4.07-4.14 (m, 9H, *Fc*); 3.50(s, 4H, -C$H_2$*CO*); 3.16 (2H, s, –C$H_2$ Fc); 1.43(s, 6H, -C$H_3$) | 168.1, 143.1, 128.7, 127.4, 126.1, 69.9, 68.6, 58.1, 55.1, 48.5, 21.8 |

### 3.2.5 Biological assay

### 3.2.5.1 In vitro Cytotoxicity Assay

MTT assay was performed to observe *in vitro* cytotoxicity of newly synthesized chiral secondary and tertiary amines S-(-)-**9,** R-(+)-**10,** S-(-)-**11,** R-(+)-**12,** S,S-(-)-**13** and R,R-(+)-**14** inhibitors holding biologically relevant ferrocene, amino-, and amidic- groups in the molecular Skelton. Carcinoma cell lines *viz.* Breast cancer cell line (MCF 7), Neuroblastoma cell line (IMR 32), Hepatocellular carcinoma cell line (HepG2) and immortal lung cell line (L132) were procured from the NCCS, Pune. Cells were cultured in required culture medium with supplementation of 10% FBS and incubated at 37℃. For cytotoxicity determination, cells were seeded in 96 well plate (8000 cells per well) and incubated overnight for adhesion then treated by synthesized ligands for 24 hours with five different concentrations. These cells were exposed to MTT solution (5mg/ml) for 5 hours at 37℃. The formazon crystals, formed by mitochondrial activity of live cell, were dissolved in 200µl of DMSO. Optical density was measured at 540nm using plate reader. Percent inhibition due to exposure of synthesized enantiomers at each concentration was calculated and $IC_{50}$ values (50 % inhibition concentration) were derived. Metal based drug cisplatin was used as a reference

### 3.2.6 Molecular docking study

### 3.2.6.1 Ligand preparation

Co-crystal ligand (Ligand ID: 307) of protein 2AZ5 (Fig. S22) was downloaded from Pubchem database. The designed ligand molecules were sketched using Chemdraw 19.0. All the ligands were energy minimised using MM2 force field and saved in CDX format and converted into PDB format using Open Babel Graphical User Interface OBGUI software. [12a] All the Ligands were assigned charges and torsions and converted to PDBQT in AutoDock 4.0 (The Scripps Research Institute) with CYGWIN-64.

### 3.2.6.2 Protein preparation and Grid Parameters

The protein Tumor Necrosis Factor Alpha with PDB ID: 1TNF & 2AZ5 were downloaded from RCSB Protein Data Bank (Fig. S22). The protein preparation was executed using Swiss PDB Viewer (SPDBV 4.10). The crystal contacts and hydrophobicity were studied using Ramachandran Plot generated using Schrodinger Maestro. The grid co-ordinates were assigned within the 3D space of co-crystallized ligand for 2AZ5 and with the aid of Super Computing

Facility-SCF IIT-Delhi for 1TNF. Co-crystallized ligands are removed from the grid space prior to docking. The docking protocol is validated by re docking the co-crystal ligand onto the active site of receptor pocket.[12b]

### 3.2.6.3 Validation of Docking

The docking of ligands onto the binding site of protein is executed using AutoDock vina. Docking was performed using auto dock 4.0[12b] using CYGWIN-64. All the ligands were screened for their efficient fitting into the receptor (minimized) grid. The docking protocol is validated by redocking of co-crystal ligand onto the active site of receptor with an RMSD of 0.03 Å. The ligands were screened with 10 possible minimum energy confirmations. The non-bonding interactions within 6 Å of active site of receptor pocket is explored using Discover Studio Visualizer 21.

### 3.2.6.4 Visualization of residues Interaction

Non-bonding interactions of enantiomers S-(-)-**9** and R-(+)-**10,** S-(-)-**11** and R-(+)-**12,** S,S-(-)-**13** and R,R-(+)-**14** with protein were elucidated using Discovery Studio Client 20.[12c] The binding interactions of ligands with active site of protein were compared with that of co-crystal ligand with binding energy and RMSD.

## 3.2.7 X-ray Crystallography and Data Collection

Intensity data for R-(+)-**10,** S,S-(-)-**13** and R,R-(+)-**14,** were collected on 'X-calibur, Eos, Gemini' X-ray diffractometer equipped with Eos CCD detector at 298 K for [$C_{23}H_{28}FeN_2O_3$] R-(+)-**10**, [$C_{62}H_{69}Fe_2N_6O_4$] S,S-(-)-**13** and [$C_{62}H_{70}Fe_2N_6O_4$] R,R-(+)-**14** respectively. Monochromatic Cu-*Kα* X-ray (λ=1.54184 Å for R,R-(+)-**14**) and MoKα (λ = 0.71073 for R-(+)-**10** and R-(+)-**10**) radiations were used for the measurements. Data was collected and reduced by using the ''CrysAlispro'' program (Version 1.171.37.33 Agilent Technologies, 2014). [13] All the crystal structure were solved by the direct methods, and the refinement was carried out by full-matrix least squares against $F^2$ using SHELXL program package[14] and Olex2 (version 1.2.5) program package. [15] All non-hydrogen atoms were refined anisotropically.

## 3.3 RESULTS AND DISCUSSION

### 3.3.1 Synthesis and Characterization

α-chloroamide precursors were prepared from S/R-1-phenylethylamine or S/R-1-(1-naphthyl)ethylamine by following literature procedures. [9a, 16] α-iodoamides (S)-**5**, (R)-**6**, (S)-**7** and (R)-**8** were synthesized conveniently in high yields by reacting corresponding α-chloroamides with KI in acetone under reflux condition. One of the α-iodoamides *viz.* (S)-2-iodo-N-(1-phenylethyl) acetamide (S)-**5** is known,[17] however the present methos is found to be superior than earlier method which involves expansive organolithium reagents and -78º temperature. Under control reaction conditions, α-iodoamides (S)-**5**, (R)-**6**, (S)-**7** and (R)-**8** reacted smoothly with aminomethylferrocene to give ferrocene functionalized chiral 2º-amines or 3º-amines S-(-)-**9,** R-(+)-**10,** S-(-)-**11,** R-(+)-**12,** S,S-(-)-**13** and R,R-(+)-**14**, selectively, in good yields as per the Scheme 1. Iodo- being a good leaving group compare to chloro-, we tested the scope of this method and established the best reaction conditions for the selective synthesis of new ferrocene functionalized chiral 2º-amines and 3º-amines. After column chromatography the products were obtained as yellow powders in 87−90% isolated yield.

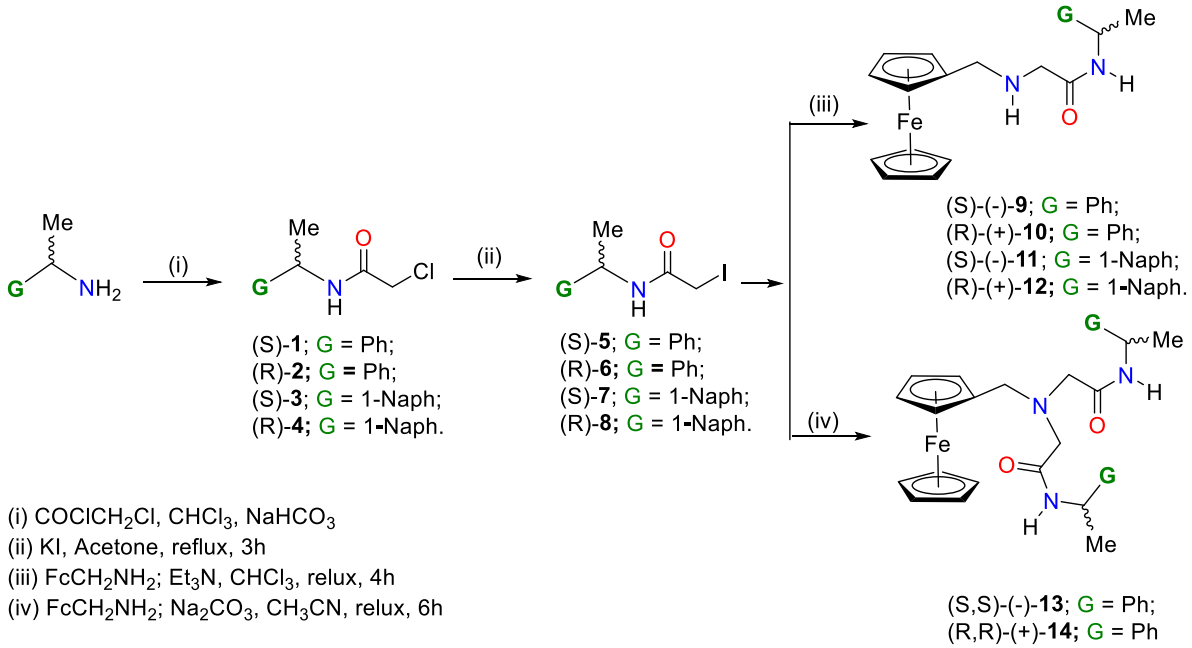


**Scheme 1.** General synthetic strategies adopted for 2-(ferrocenylmethylamino)-N-alkylacetamide (**9-12**) and 2, 2'-(ferrocenylmethylazanediyl)-bis-(*N*-alkylacetamide) (**13-14**).

All the compounds are soluble in common organic solvents and stable in the solution over days. The composition and purity of these compounds were established by $^{1}H$ and $^{13}C$ NMR, IR spectroscopy and elemental analyses. (Annaxure1-30) The presence of amidic, methylene, methyl and aromatic groups in (S)-**5**, (R)-**6**, (S)-**7**, (R)-**8** are confirmed by NMR and IR spectral data, summarized in the experimental section. (Table 1,2) The ferrocene functionalized chiral 2º amines and 3º amines (S)-(-)-**9**, (R)-(+)**10**, (S)- (-)-**11**, (R)- (+)**12,** (S, S)-(-)-**13**, (R, R)-(+)-**14** gave $^{1}H$ NMR signals in the range of ~ 4 ppm corresponding to ferrocenyl group[9a] which is further confirmed by their $^{13}C$ NMR spectral study.

The UV-visible spectrum of all compounds (9-14) shown in Figure. 1 gives three absorption bands in the region of ~250 nm, ~370 nm and 400-500 nm, mainly attributed to the locally excited intra-ligand π→ π*, n→ π* and ligand to metal (LMCT) charge transfer transitions,[9a] respectively (Table 1).

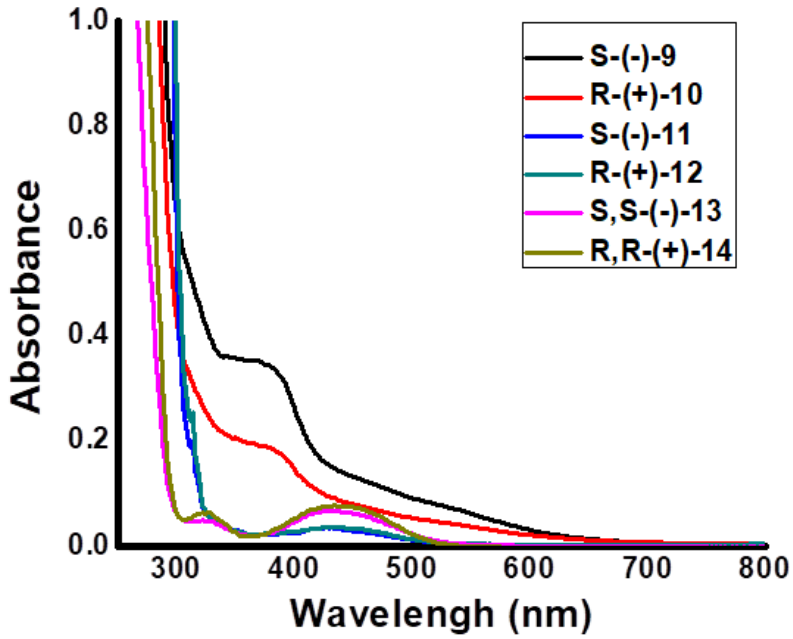


**Figure 1.** UV-visible absorption spectrum of the compounds under investigation at room temperature in $10^{-5}$ M $CH_3CN$.

**Table 1.** UV-visible absorbance bands for compounds under investigation.

| Entry | Selected IR Bands (KBr, $cm^{-1}$) | | UV-Visible data ($10^{-5}$ $CH_3CN$) $\lambda_{max}$ nm (ε L $Mol^{-1}$ $cm^{-1}$) |
|---|---|---|---|
| | υ(NH) | υ(CO) | |
| **S-(-)-9** | 3240 | 1643 | 254 (15786) π→ π* |

| | | | |
|---|---|---|---|
| | | | 376 (8462) n→ π*<br>478(6254) charge transfer |
| **R-(+)-10** | 3441 | 1697 | 256 (14787) π→ π*<br>325 (14569) n→ π*<br>477(7554) charge transfer |
| **S-(-)-11** | 3276 | 1650 | 313 (6669) n→ π*<br>440(7354) charge transfer |
| **R-(-)-12** | 33173 | 1649 | 314 (6359) n→ π*<br>441(7254) charge transfer |
| **S,S-(-)-13** | 3313, 3240 | 1666, 1639 | 253 (14787) π→ π*<br>325 (6469) n→ π*<br>435(7254) charge transfer |
| **R,R-(+)14** | 3397, 3236 | 1658, 1639 | 243 (33613) π→ π*<br>325(2756) n→ π*<br>437(4628) charge transfer |

### 3.3.2 Thermogravimetric Analysis of S,S-(-)-13 and R,R-(+)-14.

Thermogravimetric study of the compounds was performed under $N_2$ atmosphere. It was observed that the Enantiomers S,S-(-)-13 and R,R-(+)-14 showed an endothermic peak at 141.1 °C,and142.3 °C respectively on DTA curves (Figure 2), without any mass loss on DTG curves, and these peaks attributes to the melting point of the compounds. Notably, TGA curves of these show one-step decomposition in the 250−550 °C temperature range with weight loss of 61.0, and 75.8 respectively, however we could not observe a stable residual mass on TG curve and weight loss continues till 550 °C.

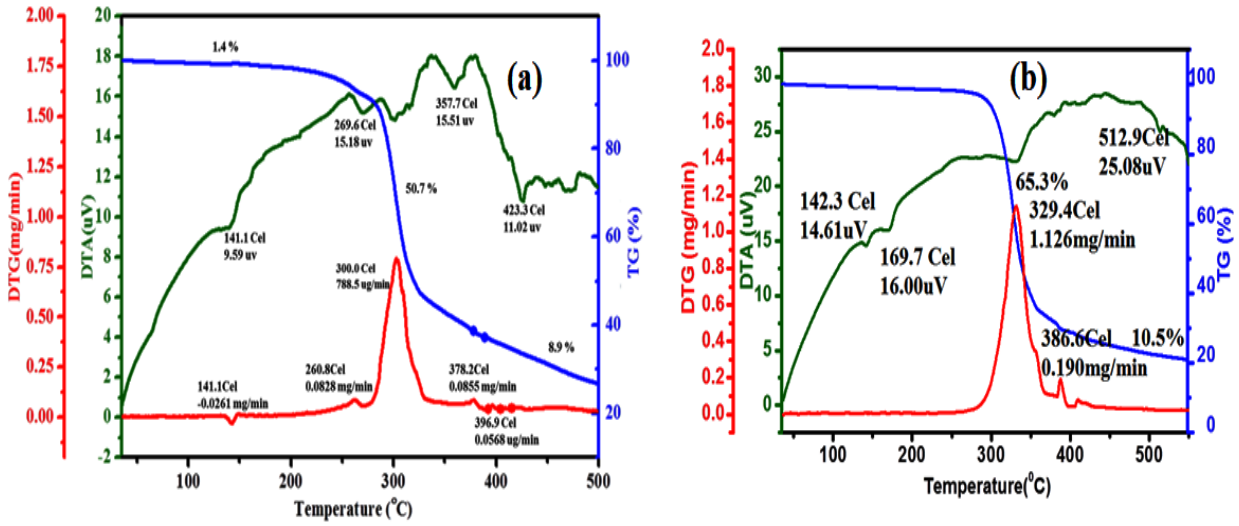


**Figure 2.** TG/DTA curves for (a) S,S-(-)-**13** , (b) R,R-(+)-**14** .

Notably, Tertiary amines S,S-(-)-**13** and R,R-(+)-**14** compounds show two different CO stretching frequencies in 1658-1639 $cm^{-1}$ region (Table 1, Annaxure 29,30) due to the involvement of both the CO in diverse H-bonding interactions as verified by SCXRD study.

### 3.3.3 X-ray crystallographic study

Solid samples crystallize in monoclinic $P2_1$, S, S-(-)-**13** and R, R-(+)-**14** and orthorhombic R-(+)-**10**, centrosymmetric space groups. The *ORTEP* view at 50 % probability for these compounds R-(+)-**10,** S, S-(-)-**13** and R, R-(+)-**14** are shown in Figure 3. Details about data collection, refinement, and structure solution are recorded in (Table 2), and selected geometrical parameters are tabulated in Table 3. The structural parameters are found to be in the normal range[9a], except, the N-C bond lengths and C-N-C bond angles associated with secondary amino groups of compounds R-(+)-**10 and** the N-C bond lengths and C-N-C bond angles associated with tertiary amino groups of compounds S, S-(-)-**13** and R, R-(+)-**14**. Notably, the average N-C bond lengths associated with tertiary amino groups in enantiomeric pair S, S-(-)-**13** and R, R-(+)-**14** (ca 1.44 Å) is found to be slightly shorter than the corresponding average N-C bond lengths of 1.47 Å in analogous compound R-(+)-**10**. Further, the average C-N-C bond angles in S,S-(-)-**13** and R,R-(+)-**14** (ca 119.9°) deviates mostly from the normal range and found to be significantly larger than the corresponding average C-N-C bond angle of 111.4° in R-(+)-**10**. The experimentally obtained structural parameters are comparable with the similar parameters obtained theoretically by DFT level calculations.

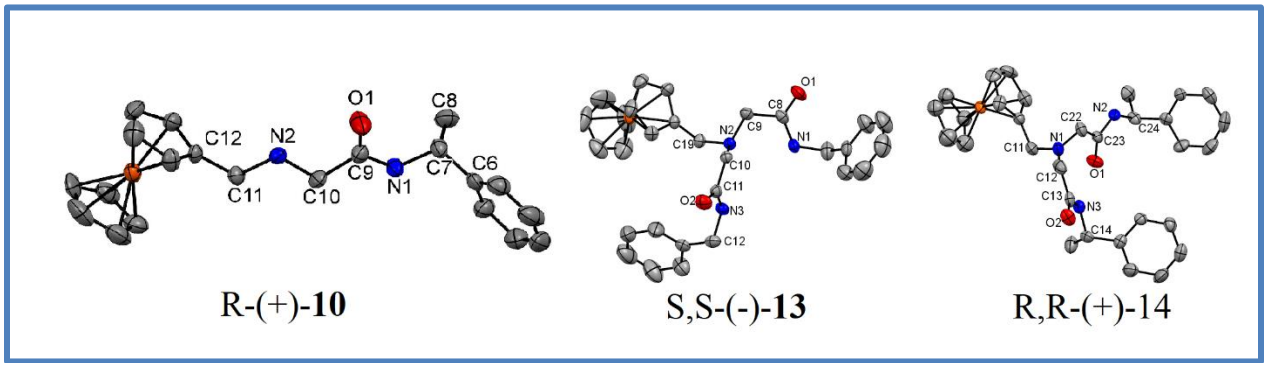


**Figure 3.** The ORTEP diagram with partial atom numbering showing 50 % probability ellipsoid; (hydrogen atoms are omitted for clarity).

**Table 2**. Crystal data and structure refinement for the compounds under investigation.

| **Identification code** | R-(+)-**10** | S,S-(-)-**13** | R,R-(+)-14 |
|---|---|---|---|
| Formula | $C_{23}H_{28}FeN_2O_3$ | $C_{62}H_{69}Fe_2N_6O_4$ | $C_{62}H_{70}Fe_2N_6O_4$ |
| Formula weight | 436.32 | 1073.93 | 1072.959 |
| Temperature/K | 293(2) | 298 | 298 |
| Crystal system | orthorhombic | monoclinic | monoclinic |
| Space group | $P2_12_12_1$ | $P2_1$ | $P2_1$ |
| a/Å | 6.3126(12) | 10.2806(3) | 10.3301(7) |
| b/Å | 11.5552(13) | 12.0852(5) | 12.1767(11) |
| c/Å | 29.272(2) | 22.0865(8) | 22.3149(19) |
| α/° | 90 | 90 | 90 |
| β/° | 90 | 100.475(3) | 100.786(7) |
| γ/° | 90 | 90 | 90 |
| Cell volume/$Å^3$ | 2135.2(5) | 2698.36(17) | 2757.3(4) |
| Z | 4 | 2 | 2 |
| $\rho_{calc}g/cm^3$ | 1.357 | 1.322 | 1.2922 |
| $\mu/mm^{-1}$ | 0.732 | 4.734 | 0.579 |
| F(000) | 920 | 1134 | 1133.9 |
| Radiation | Mo Kα (λ = 0.71073) | CuKα (λ = 1.54184) | Mo Kα (λ = 0.71073) |
| 2Θ range for data collection/° | 7.36 to 52.74° | 8.14 to 129.98 | 6.5 to 52.74 |
| Index ranges | $-2 \le h \le 7$, $-14 \le k \le 6$, $-19 \le l \le 34$ | $-12 \le h \le 12$, $-13 \le k \le 14$, $-25 \le l \le 25$ | $-13 \le h \le 13$, $-16 \le k \le 12$, $-20 \le l \le 29$ |
| Reflections collected | 3427 | 22827 | 14531 |
| Independent reflections | 3096[R(int) = 0.0261] | 8210 [$R_{int}$ = 0.1085, $R_{sigma}$ = 0.0992] | 9020 [$R_{int}$ = 0.0294, $R_{sigma}$ = 0.0609] |
| Data/restraints/parameters | 3096/0/264 | 8210/61/671 | 9020/36/629 |
| Goodness-of-fit on $F^2$ | 1.032 | 1.027 | 1.078 |
| Final R indexes [I>=2σ (I)] | $R_1$ = 0.0550, $wR_2$ = 0.0908 | $R_1$ = 0.0722, $wR_2$ = 0.1811 | $R_1$ = 0.0701, $wR_2$ = 0.1639 |
| R indexes [all data] | $R_1$ = 0.0759, $wR_2$ = 0.1007 | $R_1$ = 0.0903, $wR_2$ = 0.1983 | $R_1$ = 0.0902, $wR_2$ = 0.1820 |
| Larg. diff. peak/hole /$eÅ^{-3}$ | 0.44/-0.42 | 0.94/-0.56 | 0.89/-0.59 |
| Flack parameter | 0.01(3) | -0.013(6) | -0.02(2) |

**Table 3.** Selected bond length and bond angles of R-(+)-**10,** S,S-(-)-**13** and R,R-(+)-**14** .

| Selected Bond Lengths(Å) | Selected Bond angles(º) |
|---|---|
| R-(+)-**10** | |
| N1-C7 = 1.464(6); N1-C9 = 1.334(6); O1-C9 = 1.212(6); C9-C10= 1.510(6); N2-C10 = 1.468(6); N2-C11= 1.487(6) | O1-C9-N1 = 124.9(5); O1-C9-C10 = 121.4(5); N1-C9-C10 = 113.6(5); C9-C10-N2 = 111.5(4); C10-N2-C11 = 111.4(4) |
| S,S-(-)-**13** | |
| N3-C14 = 1.441(9); N3-C13 = 1.352(8); O2-C13 = 1.235(9); C12-C13 = 1.534(11); N1-C12 = 1.409(10); N1-C11 = 1.474(10); N1-C22 = 1.395(9); C22-C23 = 1.535(9); O1-C23 = 1.230(8); N2-C23 = 1.340(9); N2-C24 = 1.478(8) | O1-C23-N2 = 124.5(6); O1-C23-C22 = 121.7(6);N2-C23-C22 = 113.8(6); O2-C13-C12 = 121.2(6); O2-C13-N3 = 123.2(7); N3-C13-C12 = 115.6(7); C11-N1-C22 = 117.5(6); C11-N1-12 = 121.3(6); C12-N1-C22 = 121.1(6). |
| R,R-(+)-**14** | |
| N2-C13 = 1.326(7); N2-C14 = 1.458(9); C12-C13 = 1.523(11); O2-C13 = 1.228(8); N1-C11 = 1.464(9); N1-C12 = 1.425(10); N1-C22 = 1.411(8); C22-C23 = 1.509(9); O1-C23 = 1.230(8); N3-C23 = 1.320(8); N3-C24 = 1.472(8). | O1-C23-N3 = 124.6(6); O1-C23-C22 = 121.0(6); N3-C23-C22 = 114.3(6); O2-C13-C12 = 120.3(5); O2-C13-N2 = 123.5(7); N2-C13-C12 = 116.1(6); C11-N1-C22 = 117.1(7); C11-N1-C12 = 122.2(6); C12-N1-C22 = 120.6(6). |

Notably, two molecules present in the asymmetric unit cell of enantiomeric pair S,S-(-)-**13** and R,R-(+)-**14** adopt different alignments. For instance, in S,S-(-)-**13**, ferrocenyl groups are found to be far from each other **(**Figure. 4**)** whereas they are in the close vicinity in R,R-(+)-**2 (**Figure 5**)**.

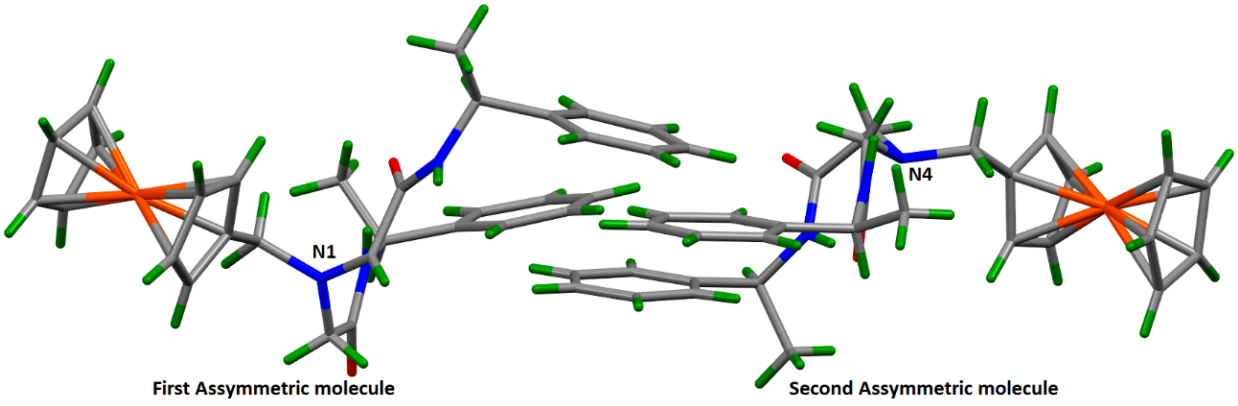


**Figure 4.** Alignment of molecules of S,S-(-)-**13** present in asymmetric unit cell.

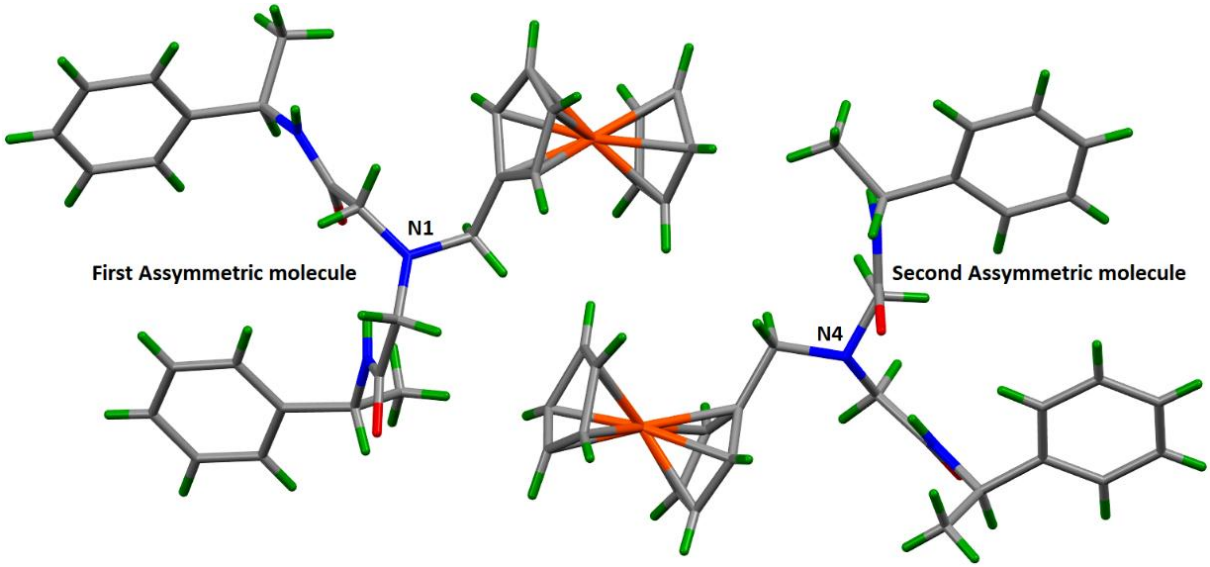


**Figure 5.** Alignment of molecules of R,R-(+)-**14** present in asymmetric unit cell.

Besides, the dihedral angles formed by two phenyl ring planes of first asymmetric molecule in S,S-(-)-**13** (24.03°) and R,R-(+)-**14** (23.61°) deviates largely from the similar angles found in the second asymmetric molecule of S,S-(-)-**13** (1.99°) and R,R-(+)-**14** (1.70°) (Figure. 6).

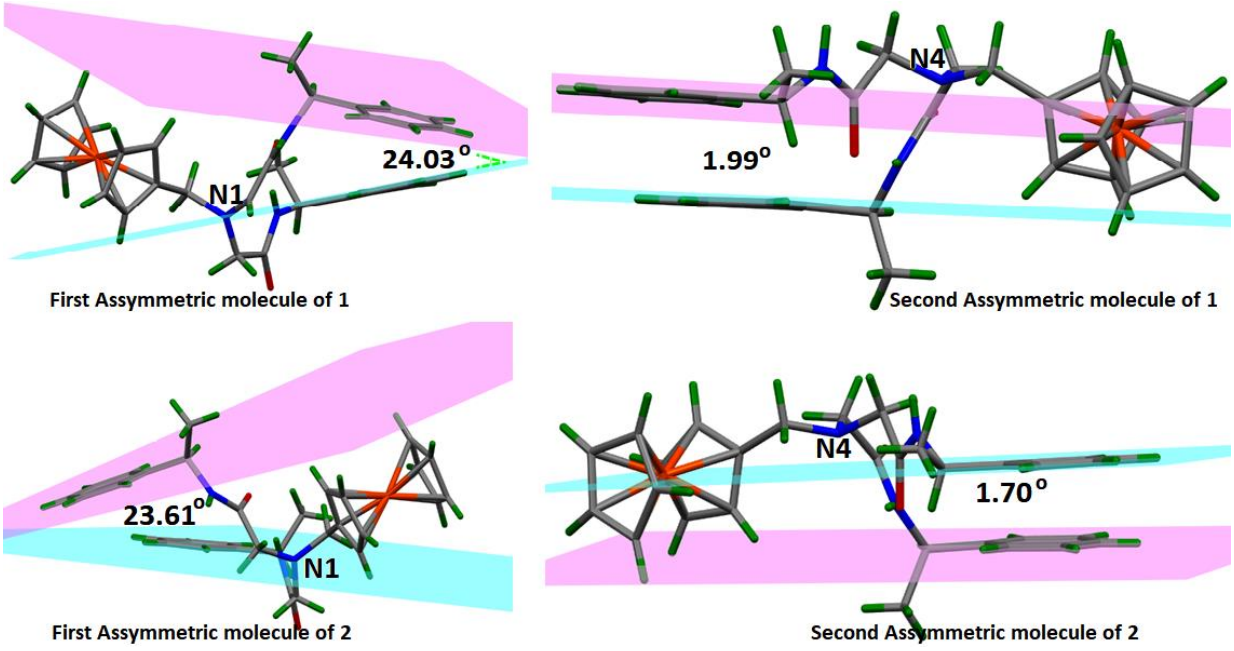


**Figure 6.** Dihedral angles formed by the phenyl ring planes of both the asymmetric molecules **1** and **2**.

The different conformational modes adopted by amidic groups in both the asymmetric molecules of enantiomeric pair S,S-(-)-**13** and R,R-(+)-**14**, they are involved in varied supramolecular packings. For instance, first asymmetric molecule of S,S-(-)-**13** is primarily engaged in the formation of intra- and intermolecular hydrogen bonding interaction involving N2H2…O1 (2.041 Å, intra-molecular) and donor-acceptor N3H3…O2 (2.024 Å, intermolecular) H-bonding interactions. This leads to a fascinating 1D helical (M-type, left-handed) supramolecular arrangement of molecules with helical pitch of 12.085 Å as shown in Figure. 7. Interestingly, first asymmetric molecule of R,R-(+)-**14** with similar intermolecular contacts vis. N2H2…O1 (2.094 Å, intra-molecular) and donor-acceptor N3H3…O2 (2.050 Å, intermolecular) H-bonding contacts lead to the formation of opposite 1D helical (P-type, right-handed) supramolecular structure with helical pitch of 12.177 Å (Figure 8). Lack of intra-molecular H-bonding interactions in the second asymmetric molecule of enantiomeric pair S,S-(-)-**13** and R,R-(+)-**14**, leading to 1D zig-zag molecular arrangements through donor-acceptor N5H5…O4 (2.013Å) and N6H6…O4 (2.042Å) intermolecular H-bonding interactions as shown in Figure. 9 and Figure 10.

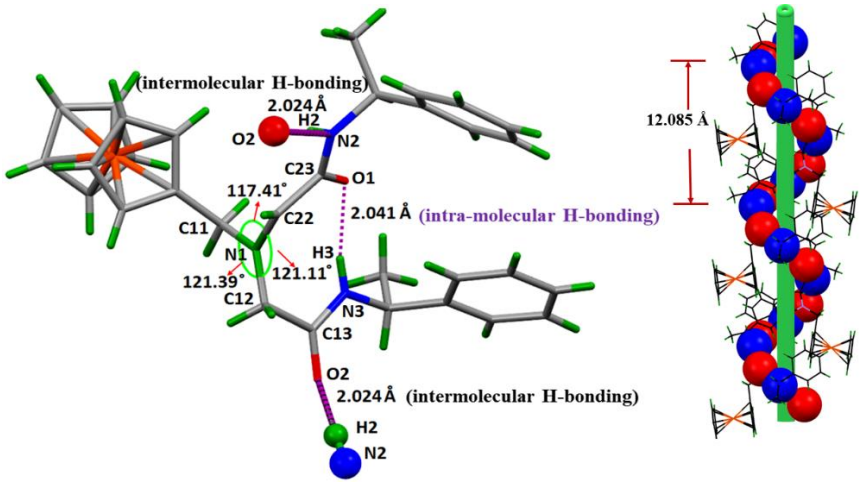


**(a)** **(b)**

**Figure 7.** First asymmetric molecule of S,S-(-)-**13** showing propensity to form (a) intra- and intermolecular H-bonding, (b) S,S-(-)-**13** forming fascinating 1D M-helix through NH-O (inter) and NH-O (intra) with helical pitch of 12.085 Å.

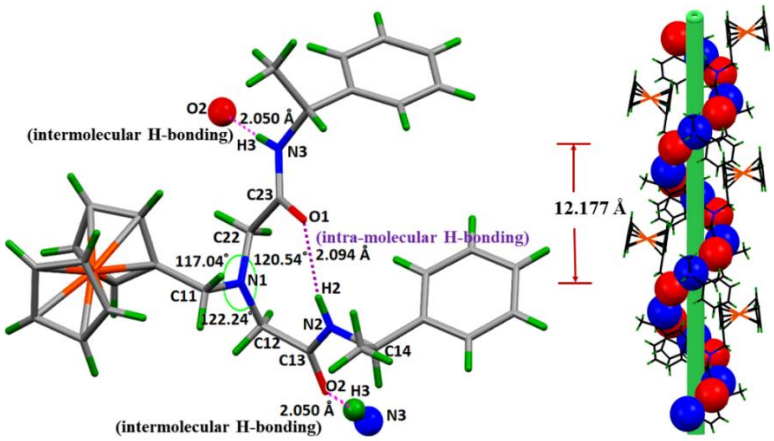


**(a)** **(b)**

**Figure 8.** First asymmetric molecule of R,R-(+)-**14** showing propensity to form (a) intra- and intermolecular H-bonding, (b) R,R-(+)-**14** forming fascinating 1D P-helix through NH-O (inter) and NH-O (intra) with helical pitch of 12.177 Å.

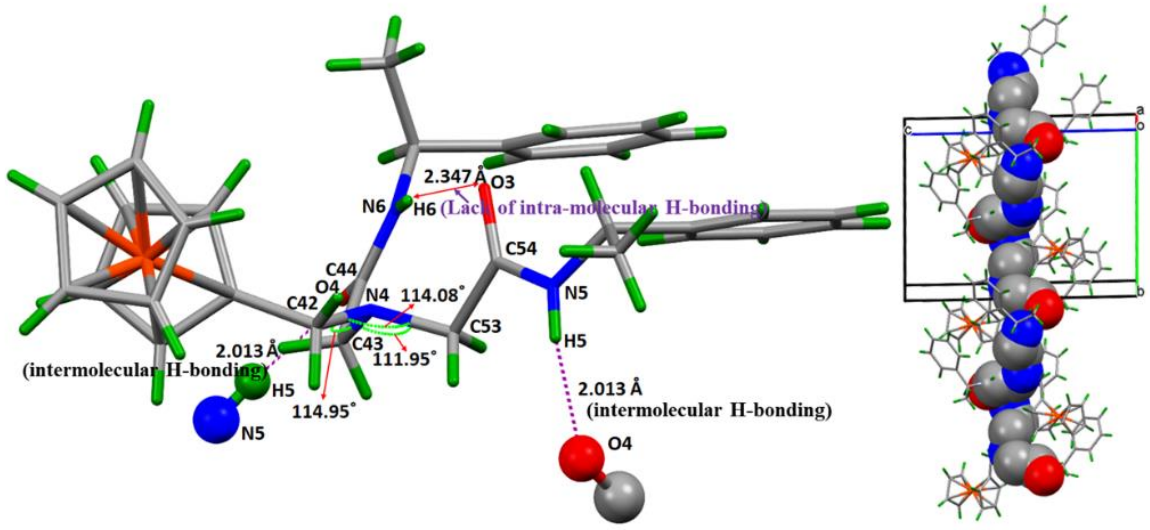


**(a)** **(b)**

**Figure 9.** Second asymmetric molecule of S,S-(-)-13 shows propensity to form (a) only intermolecular H-bonding, (b) zig-zag arrangements of the molecules along *b*-axis.

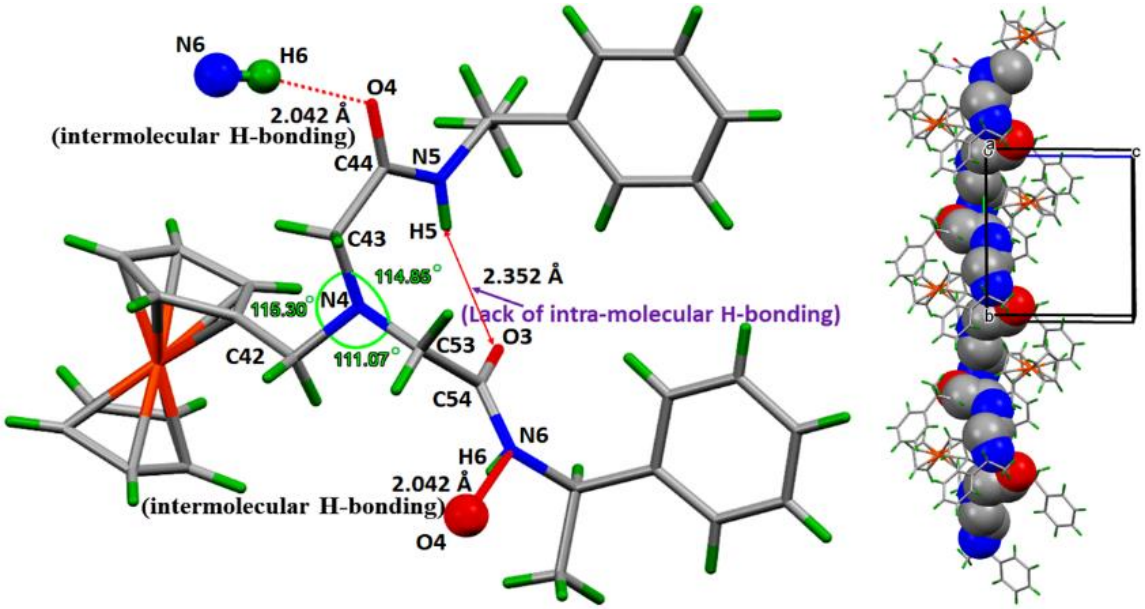


**(a)** **(b)**

**Figure 10.** Second asymmetric molecule of R,R-(+)-**14** shows propensity to form (a) only intermolecular H-bonding, (b) zig-zag arrangements of the molecules along *b*-axis.

The acetate ion is playing a crucial role in the supramolecular packing of ferrocene functionalized 2º amine (R)-FA-**6** (Figure 11a). One of the CO groups of acetate is involved in the bifurcated hydrogen bonding molecules through N1-H1…O2 (2.190 Å) and N2-H2B…O2 (1.935 Å), connecting two molecules of (R)-FA-**6** along *a*-axis**.** However, the other oxygen atom of acetate connects the third molecule through N2-H2A…O2 (1.886 Å) in the same direction but in a antiparallel fashion (Figure 11b). These hydrogen bonding forces along with several other weak interactions led the 3D supramolecular packing of (R)-FA-**6** displaying opening of approx 4.5 × 7.9 Å dimensions as shown in the Figure 11c.

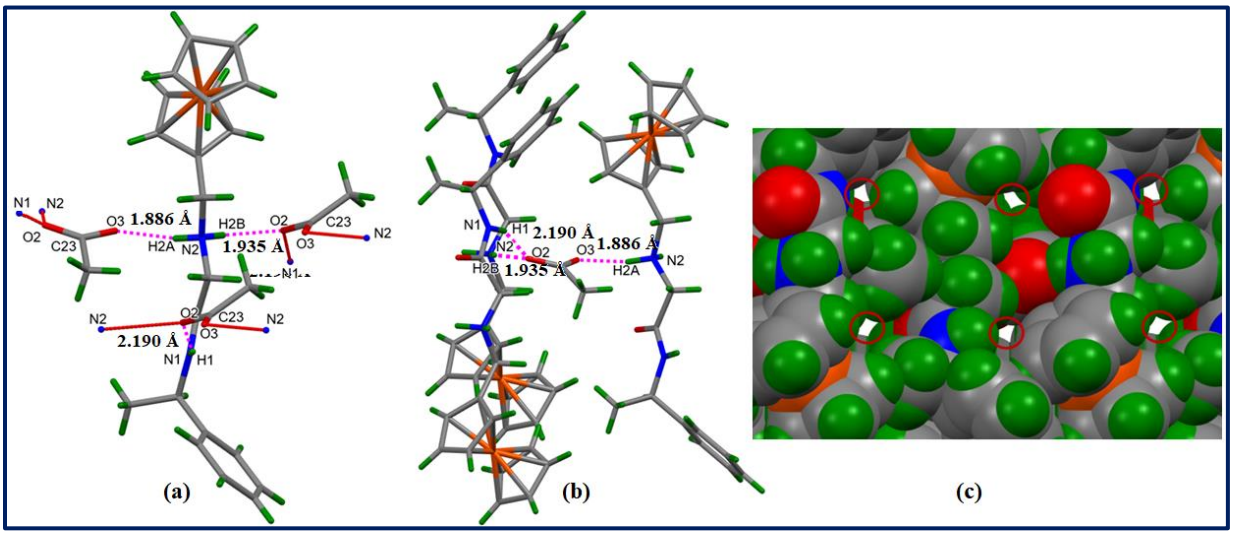


**Figure 11**. (a) Involvement acetate ions in connecting molecules via hydrogen bonding interactions. (b) parallel and antiparallel alignments of molecules of (R)-FA-**6** via N1-H1…O2, N2-H2B…O2 and N2-H2A…O2 hydrogen bonding; (c) Spacefill model illustrating 3D supramolecular packing with opening of approx 4.5 × 7.9 Å dimensions.

## 3.3.4 Hirshfeld surface analysis

Hirshfeld surface analysis[18a] was employed to quantify these noncovalent intermolecular interactions such as H-bonding, π-forces (Figure12). The relative contributions of the intermolecular interactions to the Hirshfeld surface for the compounds R-(+)-**10,** S,S-(-)-**13** and R,R-(+)-**14** [%] are shown in Table 4. For instance, tertiary amine S,S-(-)-**13** exhibits; H/H (67.3%), C/H (23.3%), O/H (8.7%), R,R-(+)-**4** exhibits; H/H (64.0%), C/H (25.2%), O/H (9.6%) while secondary amine R-(+)-**10** molecules exhibits; H/H (64%), C/H (19.7%), O/H (15.4%) weak intermolecular interactions. Apparently, this shows the ability of these molecules to inhibit cell growth by offering secondary interaction in the biological system.

The control of helicity at the supramolecular level is a charming test for chemists. Helicity in supramolecular constructions apparently induced by conformation limits of molecules, inter, intra-molecular hydrogen bonds, or coordination to metal ions. Reportedly, a majority of helical molecular assemblies in the crystalline phase based on the use of achiral building blocks.[19] Thus, chirality induced formation of left-handed (M-type) and right-handed (P-type) helices and their influences on the anti-proliferative activity of the enantiomers (discussed later) adds merit to this work.

'CrystalExplorer17' was assessed to explore and visualize the inter molecular contacts within the crystal lattice.[18b] The percentages of inter-contacts were calculated (Table 4) and the 2D-finger print plots for R-(+)-**10,** S,S-(-)-**13** and R,R-(+)-**14** are shown in Figure 11, respectively. The short contacts between the protons on carbon, nitrogen, and oxygen atoms to the O atom of the amidic group result in two sharp donors and acceptor "spikes," highlighted in Figure 12. In the crystalline lattice, all hydrogen bond interactions are maximized with the carbonyl O-atom of the amide, acting as an acceptor for a number of weak N-H donors. These spikes are indicative of existence of intermolecular short contact. On the Hirshfeld surfaces, the H…H interactions appear as the largest region of the fingerprint plot in all the compounds R-(+)-**10,** S,S-(-)-**13** and R,R-(+)-**14.** The relative contributions of the intermolecular interactions to the Hirshfeld surface for the the compounds R-(+)-**10,** S,S-(-)-**13** and R,R-(+)-**14** [%] are shown in Table 4.

**Table 4.** Relative contributions of the intermolecular interactions to the Hirshfeld surface for the compounds R-(+)-**10,** S,S-(-)-**13** and R,R-(+)-**14** [%].

| **Nature of contacts** | R-(+)-**10** | S,S-(-)-**13** | R,R-(+)-**14** |
|---|---|---|---|
| H-H interaction (%) | 64 | 67.3 | 64.0 |
| C-H interaction (%) | 19.7 | 23.3 | 25.2 |
| O-H interaction (%) | 15.4 | 8.7 | 9.6 |
| Other (%) | 0.9 | 0.7 | 1.2 |

This finding, therefore, indicates the significance of these contacts in the packing arrangement of the crystal structure. Based on these findings, a detailed model was constructed showing the most prominent short range intermolecular contacts that are responsible for the packing arrangement and formation of interesting supramolecular structures as described in the main text of this chapter.

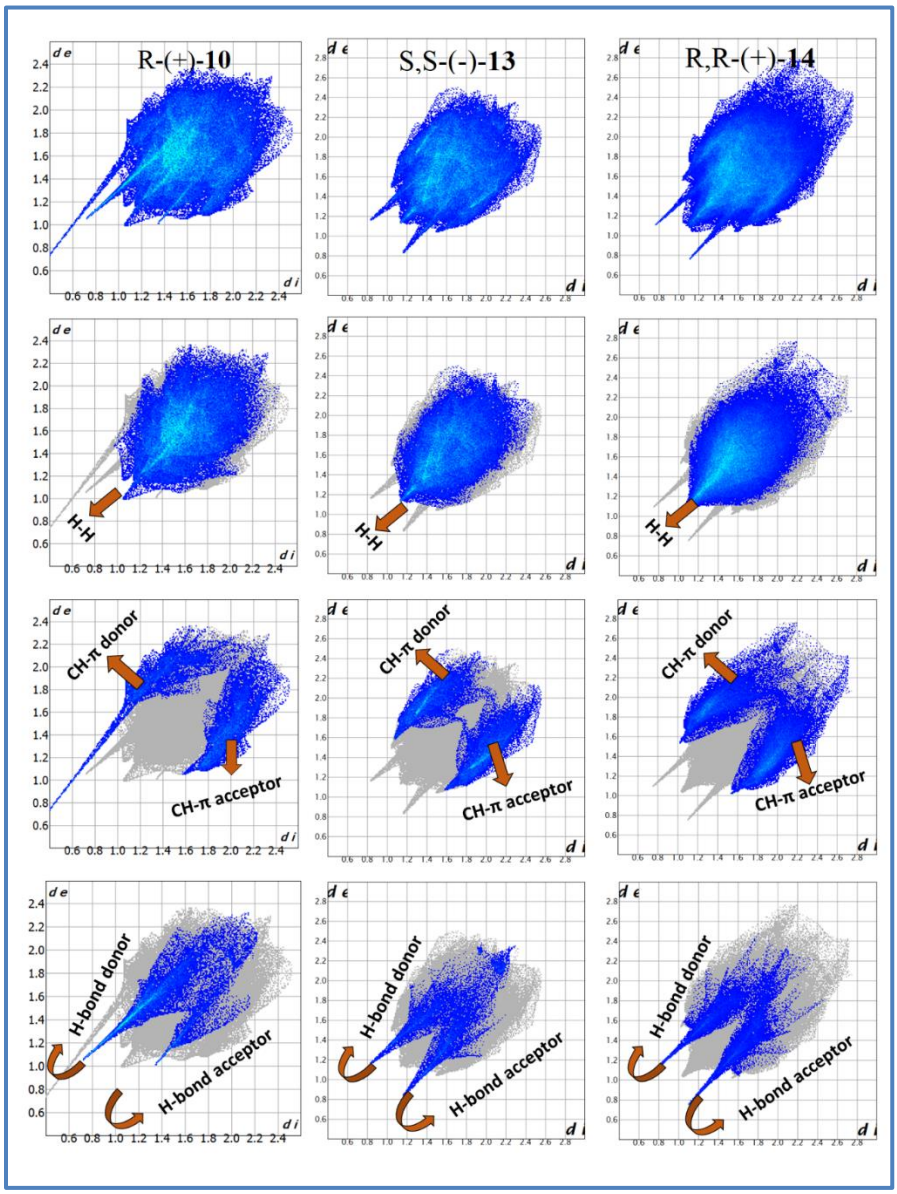


**Figure. 12.** Decomposed Hirshfeld fingerprint plots showing the contributions of atoms within specific interacting pairs (blue areas). Specific contacts are highlighted, while the entire 2D fingerprint is shown in gray. Close contacts and their reciprocal are labelled.

## 3.3.5 Theoretical Investigations.

### 3.3.5.1 Density functional theory calculations

All the calculations were carried out using the Gaussian 16 program suite and molecular orbitals were generated by GaussView 6.0 program.[20] Full geometry optimizations of S-(-)-**9,** R-(+)-**10,** S-(-)-**11,** R-(+)-**12,** S,S-(-)-**13** and R,R-(+)-**14** were performed using density functional theory (DFT) at B3LYP/Lanl2dz basis sets. These calculations were used to analyses frontier molecular orbitals, HOMO–LUMO energy gap and mapping of electrostatic potential surface to get insights of structural details. An optimized geometry for the minimum energy conformation for S-(-)-**9,** R-(+)-**10,** S-(-)-**11,** R-(+)-**12,** S,S-(-)-**13** and R,R-(+)-**14** are shown in Figure. 13. The structural parameters such as bond lengths and bond angles calculated for these compounds theoretically were found to be consistent with the similar parameters obtained experimentally by X-ray study (Table 5). The HOMO-LUMO gaps (Figure 14) and the energy of optimized geometry for compounds S-(-)-**9,** R-(+)-**10,** S-(-)-**11,** R-(+)-**12,** S,S-(-)-**13** and R,R-(+)-**14** have been summarized in Table 5.

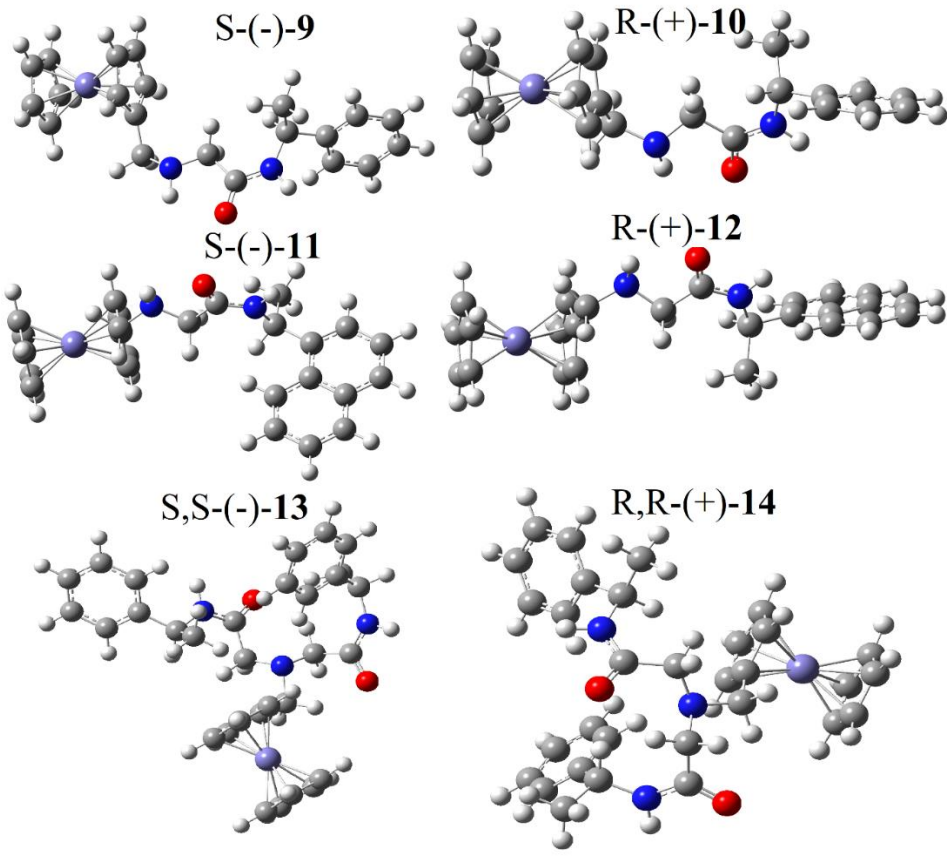


**Figure 13.** An optimized geometry for the minimum energy conformation of compounds 1-3 at B3LYP/LanL2DZ level.

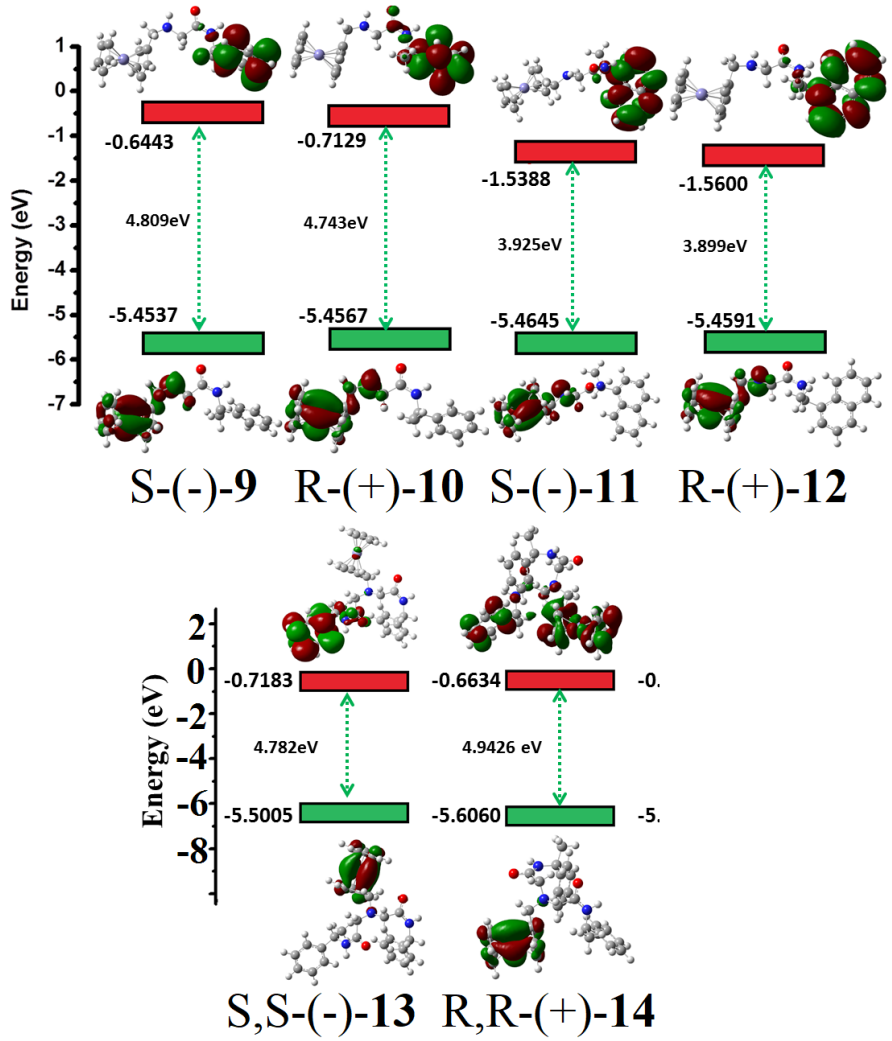


**Figure 14.** Determination of HOMO-LUMO gaps for S-(-)-**9,** R-(+)-**10,** S-(-)-**11,** R-(+)-**12,** S,S-(-)-**13** and R,R-(+)-**14** in eV.

**Table 5.** Summary of computational study performed on S-(-)-**9,** R-(+)-**10,** S-(-)-**11,** R-(+)-**12,** S,S-(-)-**13** and R,R-(+)-**14**.

| Entry | Energy of optimized geometry (Hartree) | Average N—CH2 (Å) | Average N—CH (Å) | $E_{HOMO}$, $E_{LUMO}$ (eV) | $\Delta E_{HOMO-LUMO}$ (eV) | $\lambda_{max}$ calc. (expt.) nm |
|---|---|---|---|---|---|---|
| S-(-)-**9** | -1122.68 | 1.462 | 1.483 | -5.4537, -0.6443 | 4.8093 | 257 (254) |
| R-(+)-**10** | -1122.68 | 1.465 | 1.487 | -5.4560, -0.7129 | 4.7437 | 261(256) |
| S-(-)-**11** | -1276.30 | 1.462 (1.487) | 1.488 (1.464) | -5.4645, -1.5388 | 3.9257 | 316(313) |
| R-(+)-**12** | -1276.30 | 1.465 | 1.488 | -5.4591, -1.5600 | 3.8991 | 317(314) |

| | | | | | | |
|---|---|---|---|---|---|---|
| S,S-(-)-**13** | -1640.27 | 1.496 (1.426 exp) | 1.489 (1.409 exp) | -5.50051, -0.71838 | 4.7821 | 259 (253) |
| R,R-(+)-**14** | -1640.28 | 1.492 (1.433 exp) | 1.486 (1.392 exp) | -5.60609, -0.66341 | 4.949679 | 250 (243) |

The value of $\lambda_{max}$ calculated theoretically (Table 5) matches well with the experimental value obtained from UV-visible spectral study which validate the optimized geometries.

### 3.3.5.2 Molecular electrostatic potential

The molecular electrostatic potential (MESP) of chemical species plays a decisive factor for determining the properties and potential sites associated to the reactivity in biological systems and processes. In the mapping of electrostatic potential surface (Figure. 15), the occurrence of negative potential over the amide oxygen and positive potential is around the amide proton are mainly responsible for the existence of donor-acceptor intermolecular contacts involving amidic groups in S-(-)-**9,** R-(+)-**10,** S-(-)-**11,** R-(+)-**12,** S,S-(-)-**13** and R,R-(+)-**14**.

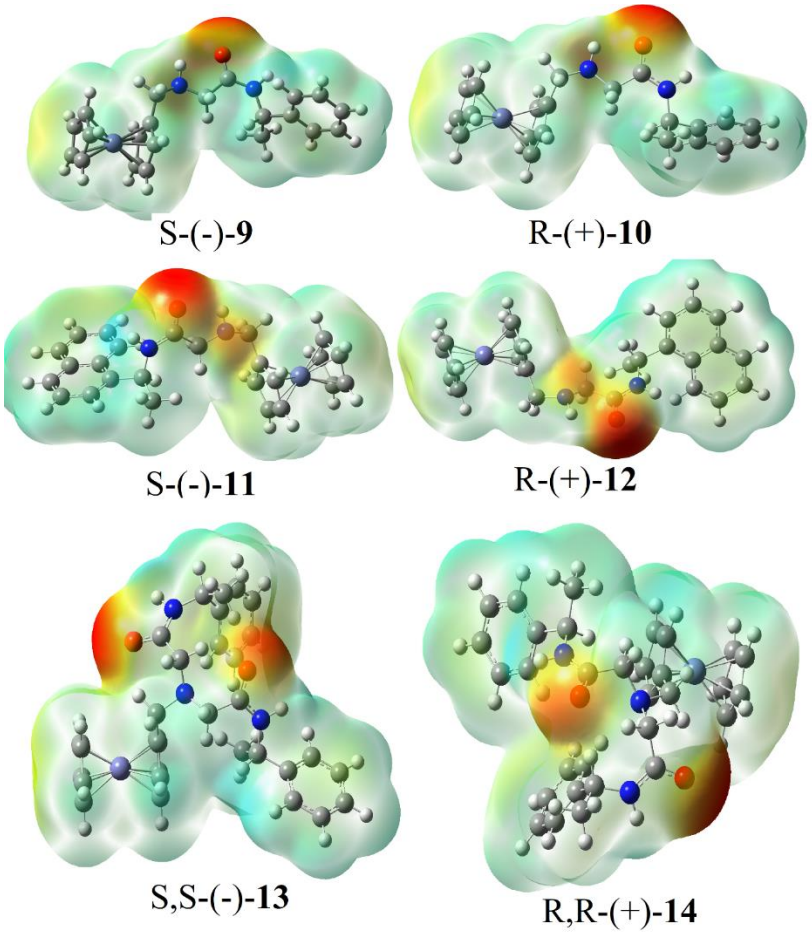


**Figure 15.** Representations of electron density from total SCF density (Isovalue= 0.0004; mapped with ESP)

## 3.3.6 Biological study

### 3.3.6.1 Inhibitory activity and structure activity relationships (SAR).

Ferrocene is involved in the generation of reactive oxygen species (ROS) within the cells, improvement of biological activity, overcome resistance barriers, lipophilic character, redox activity, and enabling easier passage through cell membranes.[3b, 21] Moreover, the incorporation of amino groups into the molecular skeleton benefits in an active transport process through the formation of organic cation transporter and thereby improves biological activity.[22] Besides, therapeutic activities of many drugs available in the market viz. penicillin G, mociobemide, acetazolamide, arimethobenzamide, etc. have been connected with amide linkage in the nucleus.[23] In the light of these observations, we have recently tested the apoptotic potentials of ferrocene functionalized chiral secondary and tertiary amines against several human cancer cell lines MCF 7, IMR 32, L132 and Hep G2 in low μM concentration. [9a] A remarkable increase in anticancer activity of these compounds with *N*-benzyl substitution at the amidic nitrogen has encouraged us to introduce chirality at the *N*-benzylic carbon to probe the chirality-related influence on the antiproliferative activity of enantiomeric pair S-(-)-**9,** R-(+)-**10** and S-(-)-**11,** R-(+)-**12** and S,S-(-)-**13,** R,R-(+)-**14**.

Expectedly, [7] one of our enantiomer R-(+)-**10** (optical rotation = +44°) displayed enhanced cytotoxic activity against all the investigated cell lines (MCF 7, IMR 32, HepG2, and immortal L132) compared to the other S-(-)-**9** (optical ration = - 42°) and our enantiomer R-(+)-**12** (optical rotation = +39°) displayed enhanced cytotoxic activity against all the investigated cell lines (MCF 7, IMR 32, HepG2, and immortal L132) compared to the other S-(-)-**11** (optical ration = - 42°) while one of our enantiomer R,R-(+)-**14** (optical rotation = +89°) displayed enhanced cytotoxic activity against all the investigated cell lines (MCF 7, IMR 32, HepG2, and immortal L132) compared to the other S,S-(-)-**13** (optical ration = - 87°) as shown in Table 6, Figure16.

The $IC_{50}$ values of synthesized inhibitors were found to be most effective on HepG2 and MCF amongst other the investigated cell line cells. In particular, R,R-(+)-**14** exhibited more than 10 folds better cytotoxic activity ($IC_{50}$: 6.35±0.19 μM) against human hepatoma cancer cells Hep G2 than S,S-(-)-**13 (**$IC_{50}$: 65.96±0.12 μM**)** and four folds better activity than highly successful anticancer drug, cisplatin ($IC_{50}$: 24.3±1.7 μM). Thus chirality-dependent formation of left- (M type) and right- (P type) handed helices and its influence on the antiproliferative activity of enantiomeric pair has been validated. The significant differences in

antiproliferative activity of the enantiomeric pair may be arises due to differences in their helicity as well as in their helical pitches (vide supra).

**Table 6.** *In vitro* cytotoxicity on cell line after 24 hours of enantiomers S-(-)-**9,** R-(+)-**10** and S-(-)-**11,** R-(+)-**12** and S,S-(-)-**13,** R,R-(+)-**14**.

| | **Ligand** | **$IC_{50}$ values (μM)[a]** | | | |
|---|---|---|---|---|---|
| | | **MCF 7** | **IMR 32** | **L132** | **HepG2** |
| 1 | S-(-)-**9** | 34.36±0.26 | 91.97±0.16 | 105.81±0.08 | 29.62±0.22 |
| 2 | R-(+)-**10** | 31.38±0.24 | 63.30±0.06 | 39.13±0.07 | 18.78±0.14 |
| 3 | S-(-)-**11** | 35.36±0.06 | 97.25±0.15 | 96.81±0.08 | 60.62±0.22 |
| 4 | R-(+)-**12** | 30.26±0.56 | 89.97±0.56 | 84.88±0.58 | 48.51±0.42 |
| 5 | S,S-(-)-**13** | 63.91±0.08 | 101.10±0.12 | 97.98±0.13 | 65.96±0.12 |
| 6 | R,R-(+)-**14** | 48.16±0.20 | 31.91±0.08 | 11.08±0.20 | 6.35±0.19 |
| 7 | Cisplatin[b] | 32.41±1.5 | 29.6±1.26 | 21.4±2.2 | 24.3±1.7 |

[a] Values are represented as Mean ± SEM. [b] IC50 value retrieved from reference [9a].

The presence of R,R-chirality is found to be crucial for enhanced activity in the biological system. A strong anticancer potential of enantiomer R,R-(+)-**14** has been well supported by molecular docking study (discussed later). Evidently, the introduction of R,R-chirality at both the *N*-benzylic groups in R,R-(+)-**14** offering a great number of H-bonding interactions with 2AZ5 and TNFR1 proteins and thus providing stability to the R,R-(+)-**2** inhibitor which apparently resulted into enhanced bioactivity. Moreover, mapping of electrostatic potential surface (Figure 13) of R,R-(+)-**2** inhibitor demonstrates that polar amide subunits are projected in such a way that it provides H-bond donor-acceptor sites to facilitate an effective H-bonding interactions with the protein molecules (discussed latter), leading to adequate cellular membrane transportation, [24] causing increased concentration at the active site.

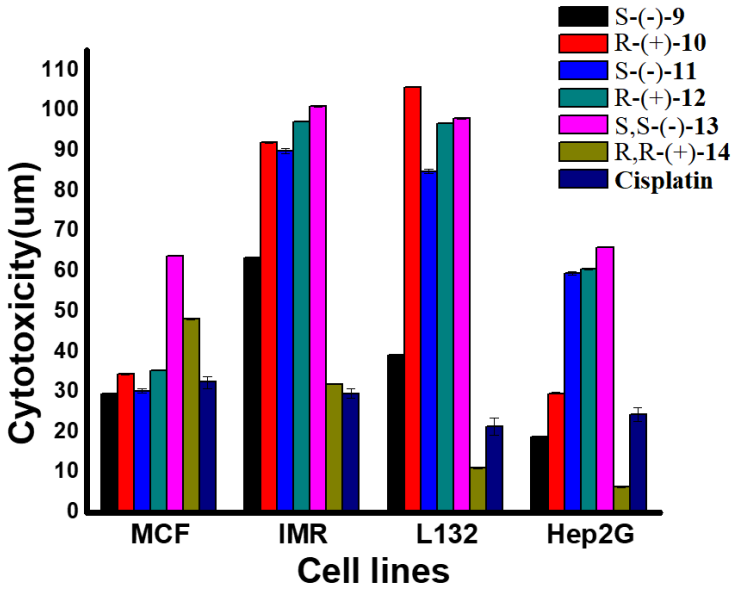


**Figure 16.** Cytotoxicity (μM) of ferrocene functionalized enantiomers S-(-)-**9,** R-(+)-**10** and S-(-)-**11,** R-(+)-**12** and S,S-(-)-**13,** R,R-(+)-**14**.

The lower cytotoxic activity of hydroxyferrocifens against both hormone-independent (ER-) and hormone-dependent (ER+) cancer cells, compared to hydroxytamoxifen, arises from the *in situ* oxidation of $Fe^{2+}$ to $Fe^{3+}$ ions and thus cell death has been linked with the oxidation of ferrocene to ferrocenium cation. The ferrocenium group appears to play the role of an intramolecular electron acceptor in the *in vitro* cytotoxicity as evidenced by the transience of the electrochemically produced $Fe^{3+}$ centre in the presence of pyridine.[25] We have used electrochemistry further to establish the structure-activity relationship and the influence of redox potential of these compounds on their cytotoxic activity.

Interestingly, the observed cytotoxicity of the enantiomers S-(-)-**9,** R-(+)-**10** and S-(-)-**11,** R-(+)-**12** and S,S-(-)-**13,** R,R-(+)-**14** (Figure 17, Table 7) appeared to follow the opposite order to their half-cell potentials E1/2 (Table 7). Similar dependences of cytotoxicity on redox potentials have been observed earlier in a series of 2-arylidenebenzocycloalkanones, 1,3-diarylidene-2-tetralones, 3,5-bis-arylidene-4-piperidones and ferrocene pyrazole conjugates.[26]

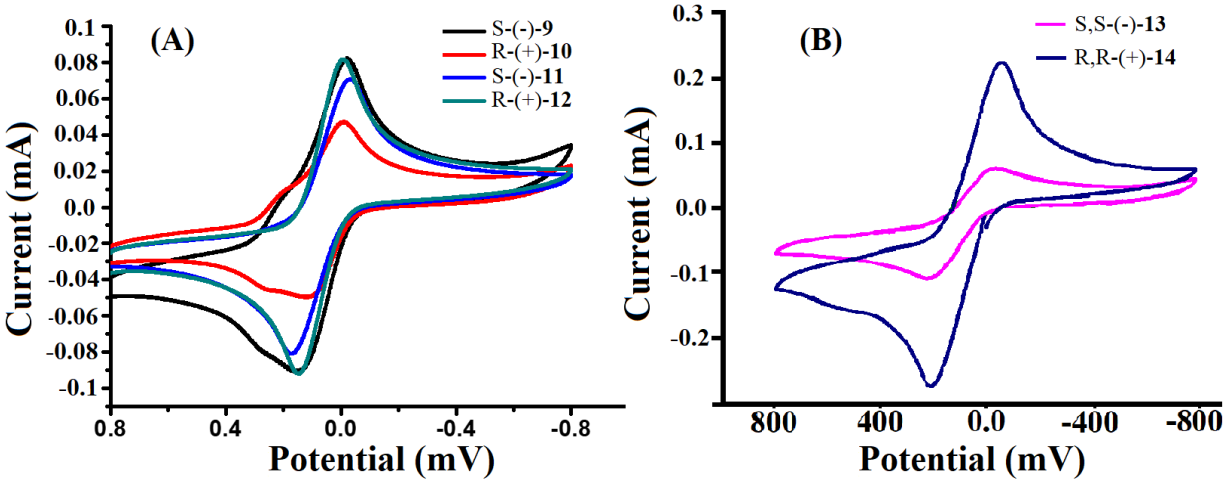


**Figure 17**. (A)Cyclic voltammograms of a 2.0 mM solution of the ferrocene functionalized chiral secondary amines S-(-)-**9,** R-(+)-**10,** S-(-)-**11** and R-(+)-**12** in $CH_3CN$ containing 0.2 M TBAP, glassy carbon (BAS) working electrode, Pt counter, Ag/AgCl reference electrode; CV: scan rate = 500 $mVs^{-1}$(B) Cyclic voltammograms of a 2.0 mM solution of the ferrocene functionalized chiral tertiary amines S,S-(-)-**13** and R,R-(+)-**14** in $CH_3CN$ containing 0.2 M TBAP, glassy carbon (BAS) working electrode, Pt counter, Ag/AgCl reference electrode; CV: scan rate = 1000 $mVs^{-1}$

It may be anticipated that the biologically active enantiomer undergoes oxidative metabolism, which is enhanced by the easier oxidation of ferrocene. The redox active ferrocene moiety may be oxidized by the biological target and might serve as a transporter of the hole while the

activated drug finds its way to reach to the target.[25] A small degree of coupling between the ferrocenium-centered radical with other radical species may lead to a relatively high energy transition state, which may stabilize the ferrocenium species on its path to the target.[26]

**Table 7** Electrochemical data for of the ferrocene functionalized chiral secondary and tertiary amines S-(-)-**9,** R-(+)-**10,** S-(-)-**11,** R-(+)-**12,** S,S-(-)-**13** and R,R-(+)-**14** at a scan rate of 500 or 1000 $mVs^{-1}$.

| Entry | Compounds | Scan rate/ $mVS^{-1}$ | $E_{Pc}$ (mV) | $E_{Pa}$ (mV) | $E_{1/2}$ (mV) | Ep(mV) |
|---|---|---|---|---|---|---|
| **1** | S,S-(-)-9 | 500 | -20.0 | 15.0 | -2.5 | +35 |
| **2** | R-(+)-**10** | 500 | -9.0 | 13.0 | +2.0 | +22 |
| **3** | S-(-)-**11** | 500 | -32.0 | 16.0 | -8.0 | +48 |
| **4** | R-(+)-**12** | 500 | -8.0 | 15.0 | +3.5 | +23 |
| **5** | S,S-(-)-**13** | 1000 | -34 | 214 | 90 | 248 |
| **6** | R,R-(+)-**14** | 1000 | -60 | 205 | 72.5 | 265 |

## 3.3.7 Protein- ligand molecular docking.

Pharmacophoric Interactions of S-(-)-**9,** R-(+)-**10,** S-(-)-**11,** R-(+)-**12,** S,S-(-)-**13** and R,R-(+)-**14** with TNFα (PDB ID: 1TNF and 2AZ5) Molecular docking for protein-ligand interactions have been performed to determine the binding mode of synthesized inhibitors S-(-)-**9,** R-(+)-**10,** S-(-)-**11,** R-(+)-**12,** S,S-(-)-**13** and R,R-(+)-**14** with the active sites of TNFα (PDB ID: 1TNF and 2AZ5) protein. The designed lead molecules on docking on to both the proteins showed complementary H-bonding and hydrophobic interaction with active site of the protein (**Annexure 31-38**). The dock scores for each inhibitor with different poses have been represented in Table 8. The dock score clearly showed that inhibitor R,R-(+)-**14** selectively bind to both the proteins with maximum number of H-bonding interactions than the other inhibitors i.e. the most potent enantiomer R,R-(+)-**14** has prominent H-bonding interactions with both 2AZ5 (via Leu-120 and Gly-121) and 1TNF (via Lys-98, Tyr-119 and Ile-118) in addition to several hydrophobic interactions within 6 Å space of receptor pocket (active site) with optimum dock scores. Although, inhibitor R,R-(+)-**14** has shown the ability to interact with 1TNF through a common H-bonding site of Tyr-119, however bonding of inhibitor R,R-(+)-**14** is found to be significantly stronger than other inhibitor as shown in Figure 18 Thus chirality-influence on ligand-protein interactions (Table 8) is consistent with the observed cytotoxicity of these inhibitors. It has been shown that derivatives of TNFα target effect on angiogenesis as well as show reduced toxicity, as an antitumor agent in comparison to

cisplatin, doxorubicin, paclitaxel and melphalan on some cancer like lymphoma, breast cancer.[27]

**Table 8.** Non-bonding interactions within 6 Å of Active site 2AZ5 & 1TNF

| Ligand | PDB | Hydrogen Bonding Interaction (within 6 Å) | Hydrophobic Interaction (within 6 Å ) | Binding Energy Kcal/mol |
|---|---|---|---|---|
| S-(-)-**9** | 2AZ5 | Tyr-151 & Gln-61 | Tyr-59 & Tyrosine-119 | -5.6 |
| R-(+)-**10** | 2AZ5 | Leu-120 | Tyr-59 | -5.4 |
| S-(-)-**11** | 2AZ5 | Tyr-151 | Tyr-59 | -5.9 |
| R-(+)-**12** | 2AZ5 | ----- | Tyr-59, Tyrosine-119 & Leu-57 | -5.7 |
| S,S-(-)-**13** | 2AZ5 | ----- | Tyr-59, Ile 155, Leu-57 | -5.7 |
| R,R-(+)-**14** | 2AZ5 | Leu-120 & Gly-121 | Tyr 59, Tyr 119, Leu 57, Ile 155, | -6.5 |
| Co-Crystal | 2AZ5 | Tyr-59 | Leu-57, Tyr-59, Gly-121, Tyr-119 & Le- 120 | -7.0 |
| S,S-(-)-**13** | 1TNF | Gly-121 | Lue-120, Pro-117, Ala96, Lys-98, Ile-118, Lue-94, Ala96 | -5.9 |
| R,R-(+)-**14** | 1TNF | Lys-98, Tyr-119, Ile-118 | Ala-96 | -6.0 |

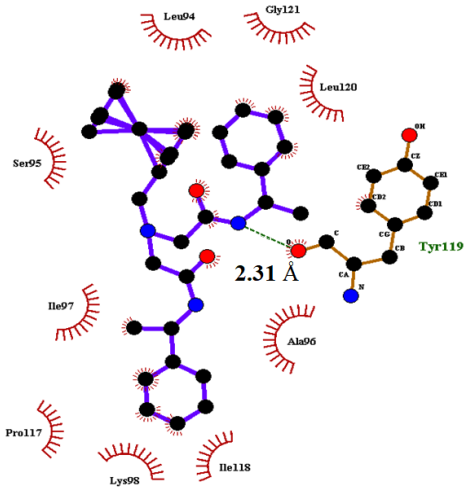


**Figure 18** Binding of R,R-(+)-**14** with TNFα receptor plotted using Ligplot+: multiple ligand-protein interaction diagrams .[28]

Pharmacokinetic profiling (computational prediction) of these compounds revealed that all the molecules under investigation have optimum cell permeability are within the range < 140 $Å^2$ and AlogP98 < 5 . [29] Drug-likeness prediction of S,S-(-)-**13** and R,R-(+)-**14** has been

ascertained by using radial plot of Flare Viewer (Annexure 39), radial plot using Swiss Adme (Annexure 40) and Molsoft (Annexure 41). All the molecules exhibited best fit with all the models and possesses lead-likeness characteristics.

## 3.4 Conclusions

A remarkable increase in anticancer activity with benzyl swapped at the amidic nitrogen of analogous ferrocene functionalized achiral tertiary amines [9a] has encouraged us to introduce diverse chirality at the *N*-benzylic carbon and to probe their influence on photophysical, electrochemical, ligand-protein bonding efficacy and anticancer properties of ferrocene functionalized chiral secondary and tertiary amine enantiomers S-(-)-**9,** R-(+)-**10,** S-(-)-**11,** R-(+)-**12,** S,S-(-)-**13** and R,R-(+)-**14**. The results showed that optically pure enantiomer R,R-(+)-**14** forming the right-handed helical motif at supramolecular level, displayed stronger inhibition against all the investigated cell lines MCF 7, IMR 32, HepG2, and immortal L132 cell lines of human origin as compared to enantiomer S,S-(-)-**13**. The chirality in the molecules at the atomic level guiding the self-assembly at supramolecular level in a similar way as the proteins, we observe in living organisms. Results suggest that a change in chirality changes the redox potential, fluorescence, ligand-protein bonding efficacy and the bio-activity of the molecules, considerably. For instance, the enantiomer R,R-(+)-**14** prominent H-bonding interactions with 2AZ5 (through Leu-120 and Gly-121) and 1TNF (through Lys-98, Tyr-119 and Ile-118) showed many folds ca 10 folds better cytotoxicity ($IC_{50}$: 6.35±0.19 μM) than other enantiomer S,S-(-)-**13 (**$IC_{50}$: 65.96±0.12 μM**)** against Hep G2 cell line. The biological characterization of these compounds provides convincing sign to recommend that enantiomer R,R-(+)-**14** has potentials for further development as anticancer agent with high efficacy against multiple cancer types.

## 3.5 Reference

[1] R. A. Casero, Jr., P. M. Woster, *J. Med. Chem*., **2001**, 44, 1.

[2] N. P. Farrell, *Chem. Soc. Rev*. 2015, 44, 8773.

[3] (a) G. Gasser, I. Ott, N. Metzler-Nolte, *J. Med. Chem.* **2011**,54, 3; (b) C. G. Hartinger, P. J. Dyson, *Chem. Soc. Rev*., **2009**, 38, 391; (C) G. Jaouen, A. Vessieres, S. Top, *Chem. Soc. Rev*., **2015**, 44, 8802.

[4] F. Bray, J. Ferlay, I. Soerjomataram, R. L. Siegel, L. A. Torre, A. Jemal, *Cancer J. Clin*. **2018**, 68, 394.

[5] Y. Wang, H. Huang, Q. Zhang, P. Zhang, *Dalton Trans*., **2018**, 47, 4449**.**

[6] (a) J. H. Kim, A. R. Scialli, *Toxicol. Sci.*, **2011**, 122, 1; (b) E. L. Izake, *J. Pharm. Sci*., **2007**, 96,1659.

[7] (a) J. F. Vollano, S. Al-Baker J. C. Dabrowiak, J. E. Schurig, *J. Med. Chem.* **1987**, 30, 716; (b) F. Arnesano, A. Pannunzio, M. Coluccio, G. Natile, *Coord. Chem. Rev*. **2015**, 284, 286.

[8] D. L. Ma, M. Wang, C. Liu, X. Miao, T. S. Kang, C. H. Leung, Coord. *Chem. Rev*. **2016**, 324, 90.

[9] (a) C. J. Savani, H. Roy, S. K. Verma, D. R. Vennapu, V. K. Singh, *Appl. Organomet. Chem*. **2021**, 35, e6137; (b) D. R. V. Staveren, N. Metzler-Nolte, *Chem. Rev*. **2004**, 104, 5931.

[10] (a) G. Jaouen, S. Top, A. VessiEres, G. Leclercq, M. McGlinchey, *J. Curr. Med. Chem.*, **2004**, 11, 2505; (b) Q. Michard, G. Jaouen, A. Vessieres, B. A. Bernard, *J. Inorg. Biochem*., **2008**, 102, 980. (c) P. Pigeon, S. Top, O. Zekri, E. A. Hillard, A. Vessieres, M. A. Plamont, O. Buriez, E. Labbe, M. Huche, S. Boutamine, C. Amatore, G. Jaouen, *J. Organomet. Chem*., **2009**, 694, 895.

[11] B. Kater, A. Hunold, H. G. Schmalz, L. Kater, B. Bonitzki, P. Jesse, A. Prokop, *J. Cancer Res. Clin. Oncol*., **2011**, 137, 639.

[12] (a) O'Boyle, N. M. et al. Open Babel: An open chemical toolbox. *Journal of Cheminformatics*, **2016**, 3, 33; (b) Darpan et al. *RSC Adv*. **2016**, 6, 14880; (c) BIOVIA, Dassault Systèmes, [Discovery Stuidos Visualiser], [2021], San Diego: Dassault Systèmes, **2021**.

[13] CrysAlispro program (Version 1.171.37.33) Agilent Technologies, **2014**.

[14] G. M. Sheldrick, Acta Cryst., **2015**, C71, 3.

[15] (a) O. V. Dolomanov, L. J. Bourhis, R. J. Gildea, J. A. K. Howard, H. Puschmann, *J. Appl. Cryst.*, **2009**, 42, 339; (b) L. J. Bourhis, O. V. Dolomanov, R. J. Gildea, J. A. K. Howard, H. Puschmann, *Acta Cryst*., **2015**, A71, 59.

[16] S. Cui, T. Wang, X. Hu, *Molecular and Biomolecular Spectroscopy*, **2014**, 133, 778.

[17] V. Pace, L. Castoldi, A. D. Mamuye, W. Holzer, *Synthesis*, **2014**, 46, 2897.

[18] (a) R. Kadu, N. A. Wani, C. Savani, S. Aravinda, R. Rai, V. K. Singh, *J. Mol. Struct.*, **2021**, 1230, 129858; (b) Turner, M. J.; McKinnon, J. J.; Wolff, S. K.; Grimwood, D. J.; Spackman, P. R.; Jayatilaka, D.; Spackman, M. A. CrystalExplorer17. The University of Western Australia **2017**.

[19] R. Kadu, V. K. Singh, S. K. Verma, P. Raghavaiah, M. M. Shaikh, *J. Mol. Struct*., **2013**, 1033, 298.

[20] M. J. Frisch, G. W. Trucks, H. B. Schlegel, G. E. Scuseria, M. A. Robb, J. R. Cheeseman, G. Scalmani, V. Barone, G. A. Petersson, H. Nakatsuji, X. Li, M. Caricato, A. V. Marenich, J. Bloino, B. G. Janesko, R. Gomperts, B. Mennucci, H. P. Hratchian, J. V. Ortiz, A. F. Izmaylov, J. L. Sonnenberg, D. Williams-Young, F. Ding, F. Lipparini, F. Egidi, J. Goings, B. Peng, A. Petrone, T. Henderson, D. Ranasinghe, V. G. Zakrzewski, J. Gao, N. Rega, G. Zheng, W. Liang, M. Hada, M. Ehara, K. Toyota, R. Fukuda, J. Hasegawa, M. Ishida, T. Nakajima, Y. Honda, O. Kitao, H. Nakai, T. Vreven, K. Throssell, J. A. Montgomery, Jr, J. E. Peralta, F. Ogliaro, M. J. Bearpark, J. J. Heyd, E. N. Brothers, K. N. Kudin, V. N. Staroverov, T. A. Keith, R. Kobayashi, J. Normand, K. Raghavachari, A. P. Rendell, J. C. Burant, S. S. Iyengar, J. Tomasi, M. Cossi, J. M. Millam, M. Klene, C. Adamo, R. Cammi, J. W. Ochterski, R. L. Martin, K. Morokuma, O. Farkas, J. B. Foresman, D. J. Fox, Gaussian, Inc. Wallingford CT, **2016**.

[21] H. Helen, M. Paul, J. Elmar, M. Veldwijk, European Patent, No. EP 2 497 775 A1, **2012**.

[22] (a) Y. Zhang, K. T. Zhao, S. G. Fox, J. Kim, D. R. Kirsch, R. J. Ferrante, R. I. Morimoto, R. B. Silverman, *J. Med. Chem*., **2015**, 58, 5942; (b) V. K. Singh, R. Kadu, H. Roy, Eur. J. Med. Chem. 2014, 74, 552; (c) S. Luo, P. Li, S. Li, Z. Du, X. Hu, Y. Fu, Z. Zhang, *Mol. Pharmaceutics.* **2017,** 14, 1771.

[23] (a) S. N. Rao, D. C. Mohan, S. Adimurthy, *RSC Adv*., **2015**, 5, 95, 313; (b) X. Peng, Z. Sun, P. Kuang, L. Li, J. Chen, *J. Chen, Org. Lett*. **2020**, 22, 5789.

[24] V. K. Singh, R. Kadu, H. Roy, P. Raghavaiah, M. M. Shaikh, *Dalton Trans*., **2016**, 45, 1443.

[25] E. Hillard, A. Vessieres, L. Thouin, G. Jaouen, C. Amatore, *Angew. Chem*. **2006**, 118, 291.

[26] C. J. Schlesener, C. Amatore, J. K. Kochi, *J. Phys. Chem*., **1986**, 90, 3747.

[27] A. Sacchi, A. Gasparri, C. Gallo-Stampino, S. Toma, F. Curnis, A. Corti, Clin. *Cancer Res.*, **2006**, 12, 175.

[28] R. A. Laskowski, M. B. *J. Chem. Inf. Model.*, **2011**, 10, 2778.

[29] G. Zhang, S. Guo, H. Cui, J. Qi, *Molecules.* **2018**, 23, 524.

## 3.6 Annexures

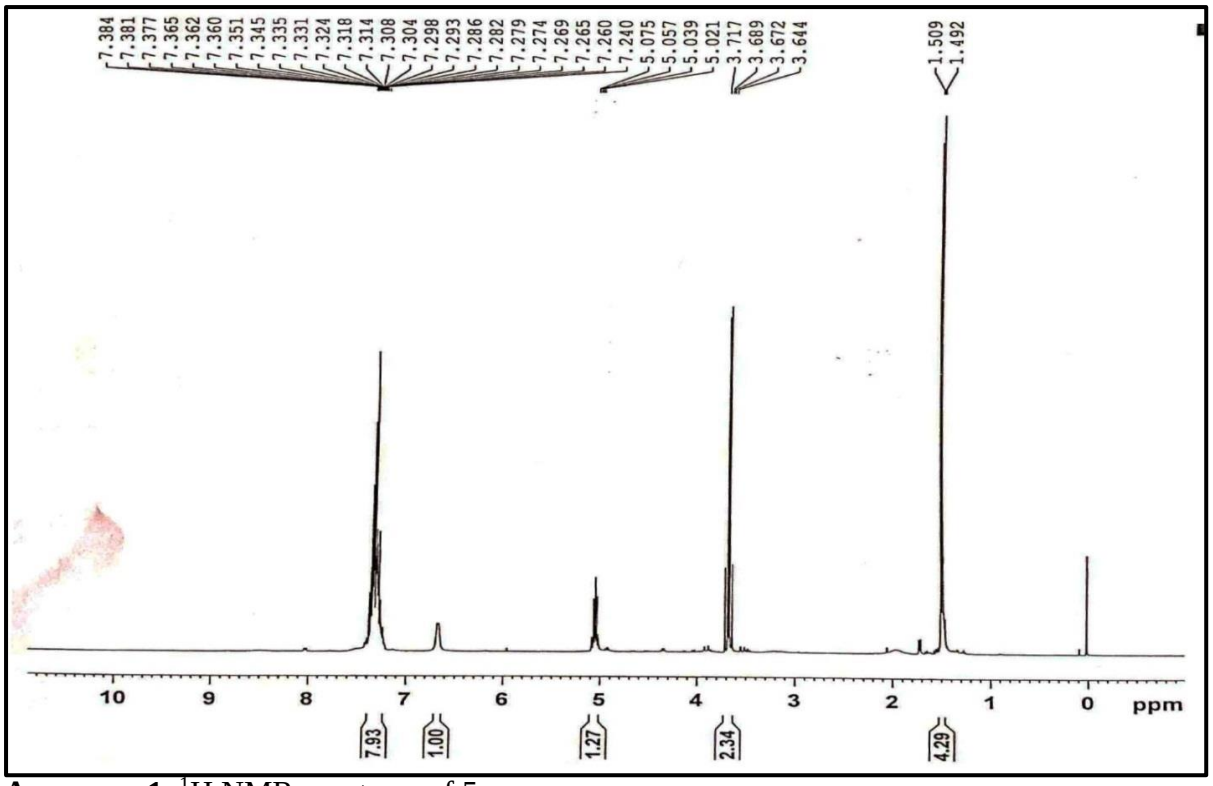


**Annexure 1**. $^{1}H$ NMR spectrum of 5.

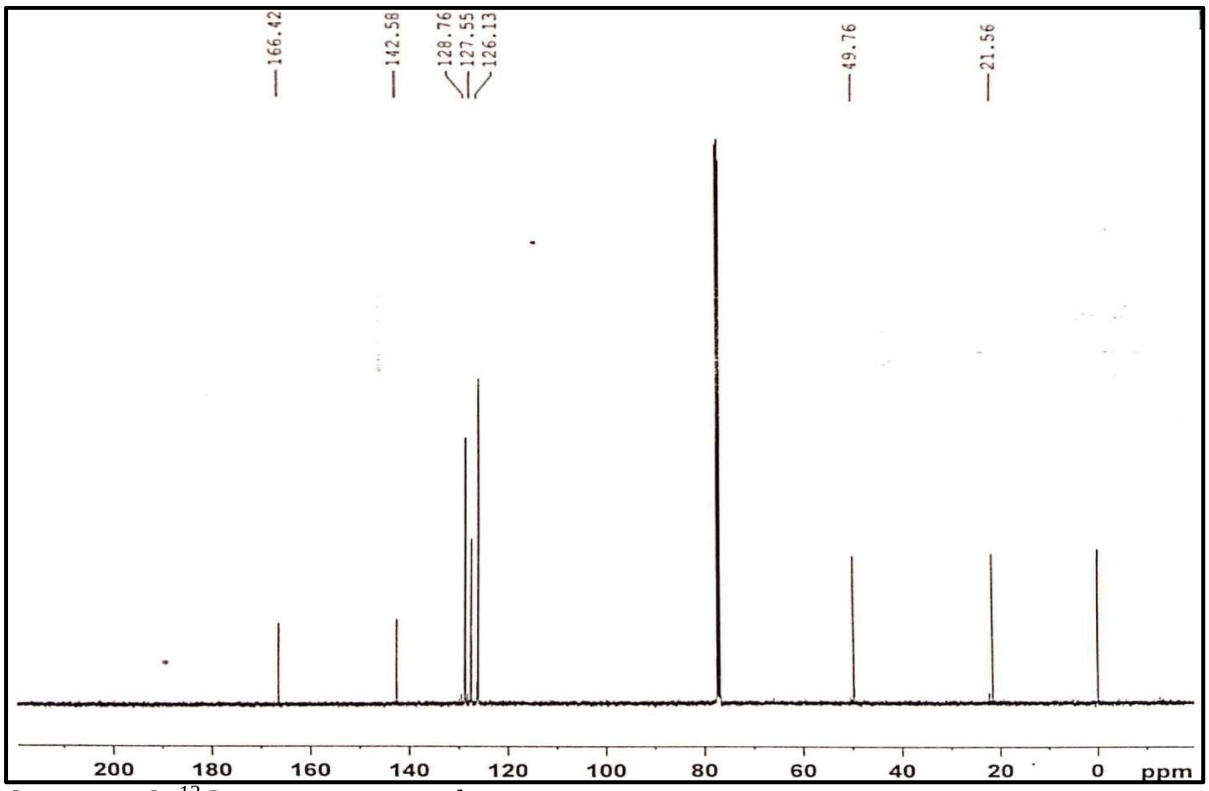


**Annexure 2.** $^{13}C$ NMR spectrum of 5.

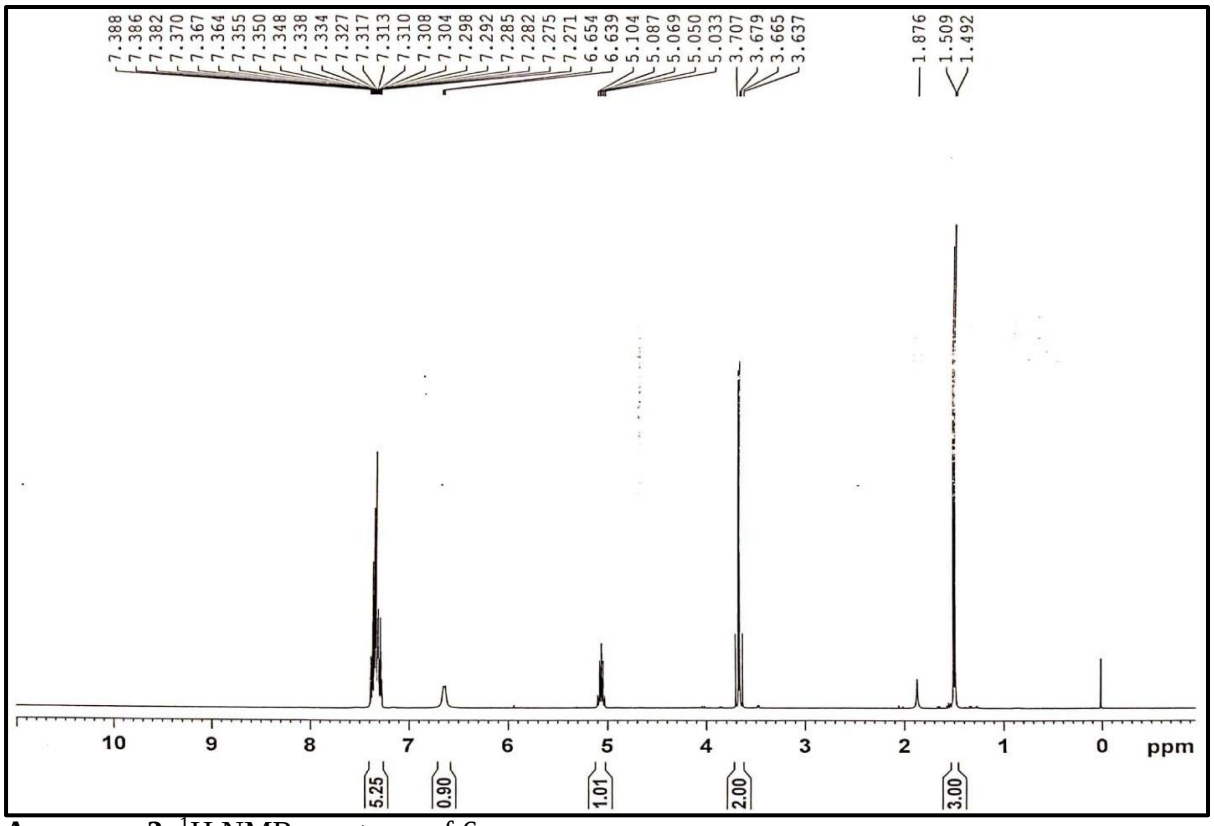


**Annexure 3**. $^{1}$H NMR spectrum of 6.

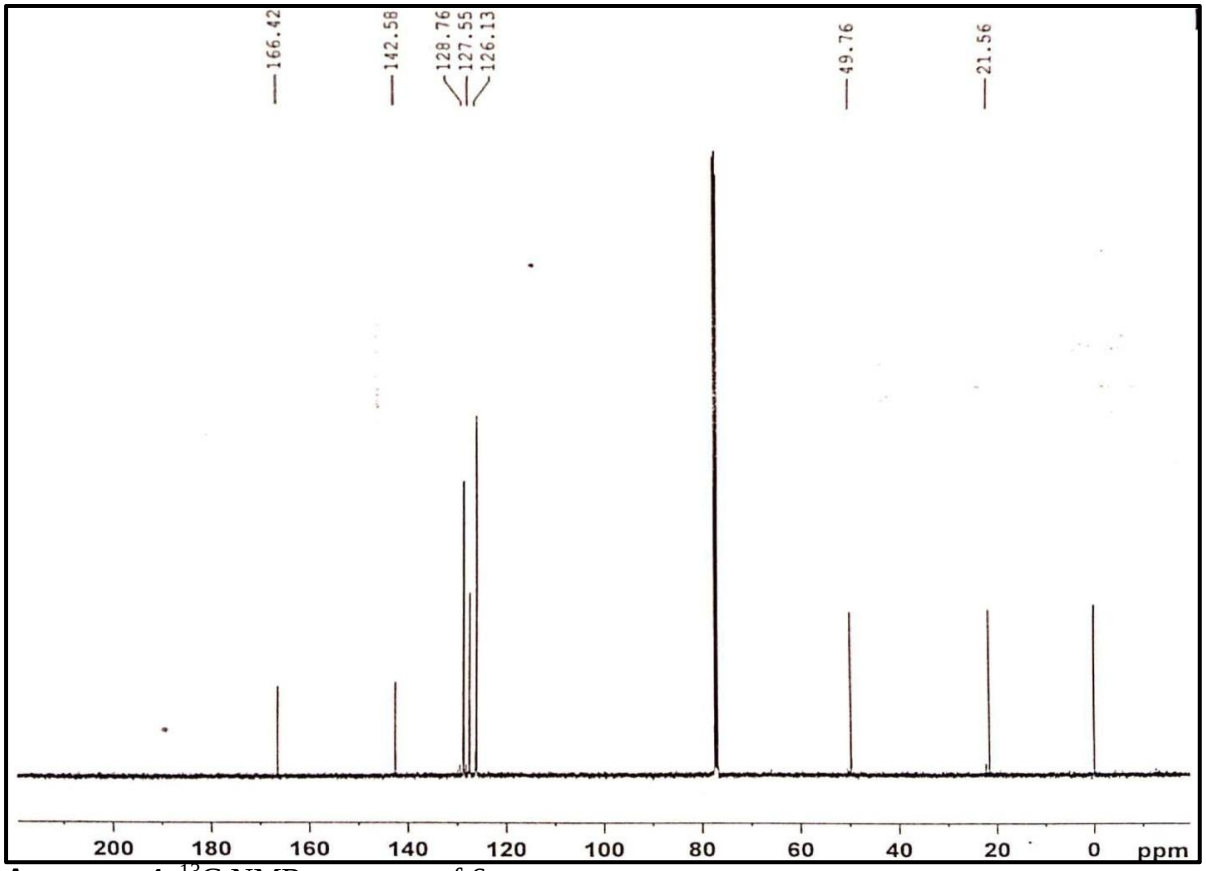


**Annexure 4.** $^{13}$C NMR spectrum of 6.

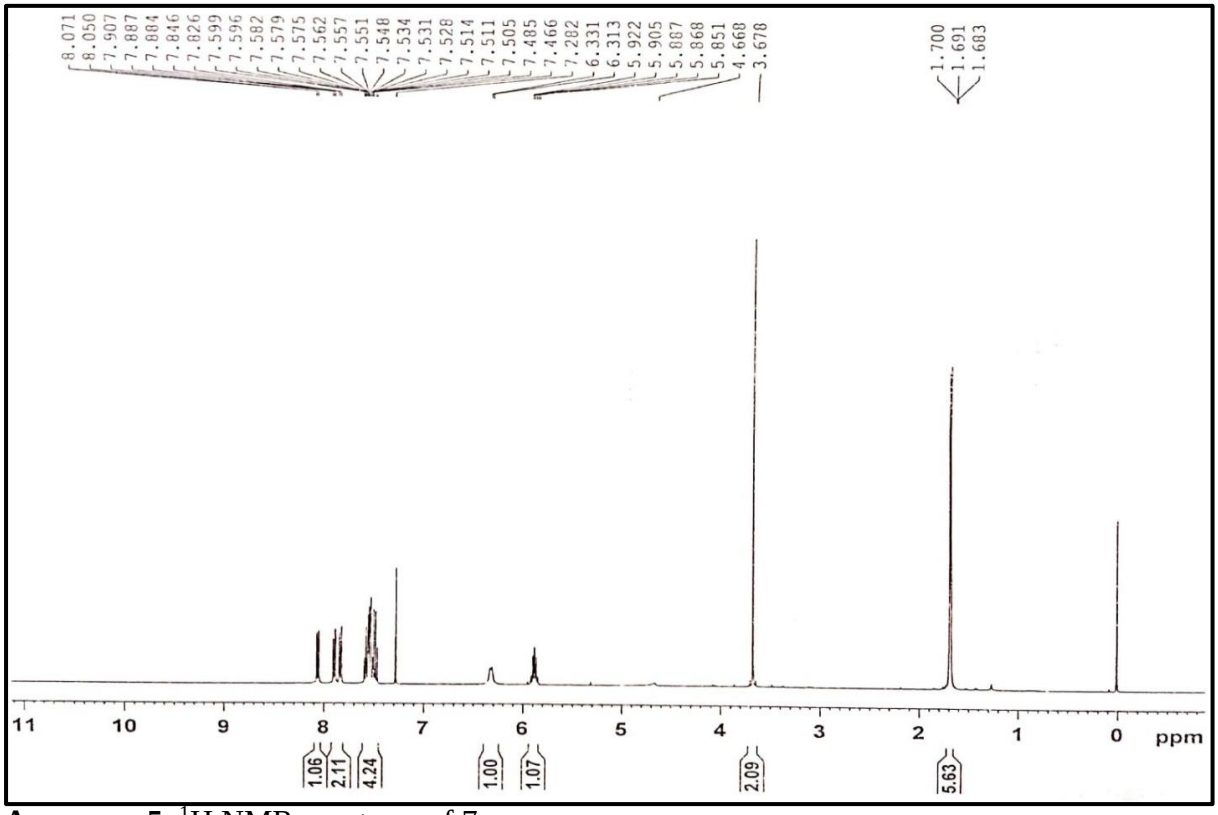


**Annexure 5.** $^{1}$H NMR spectrum of 7.

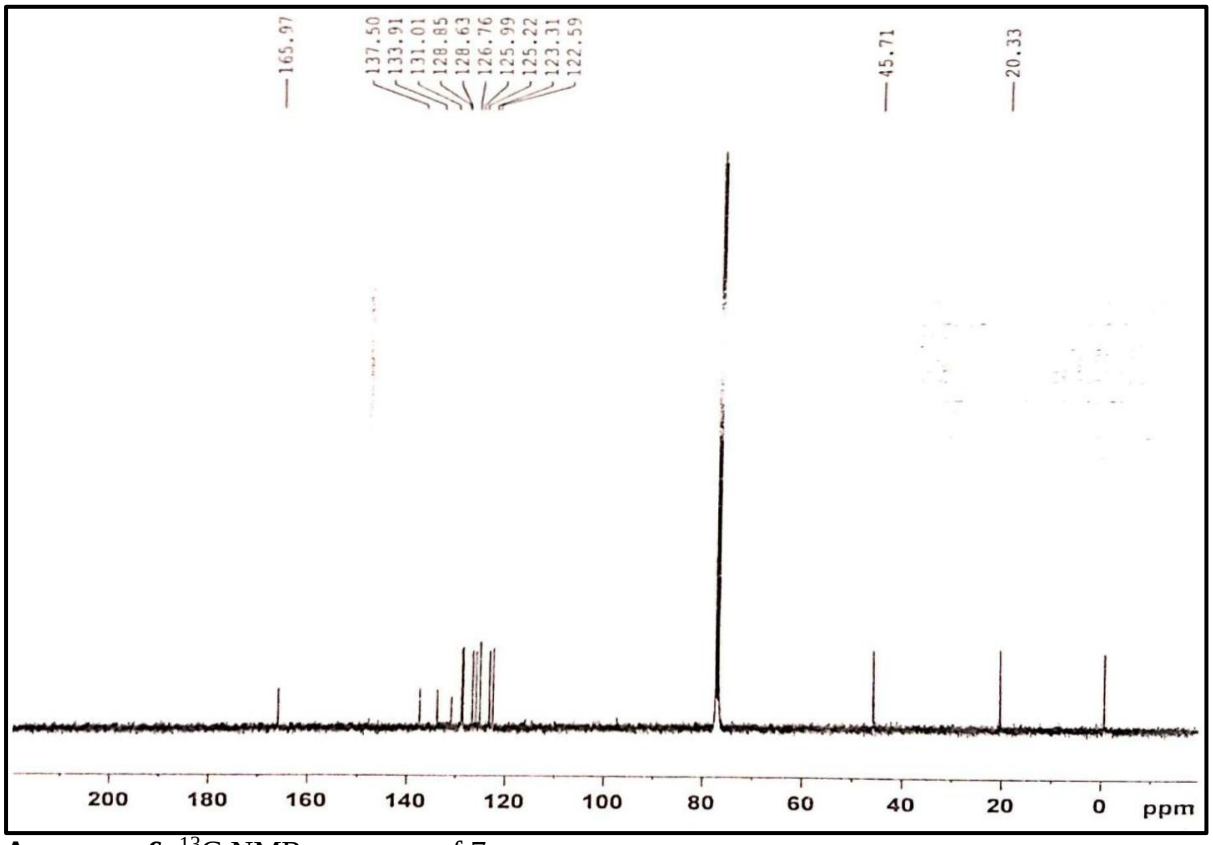


**Annexure 6**. $^{13}$C NMR spectrum of 7.

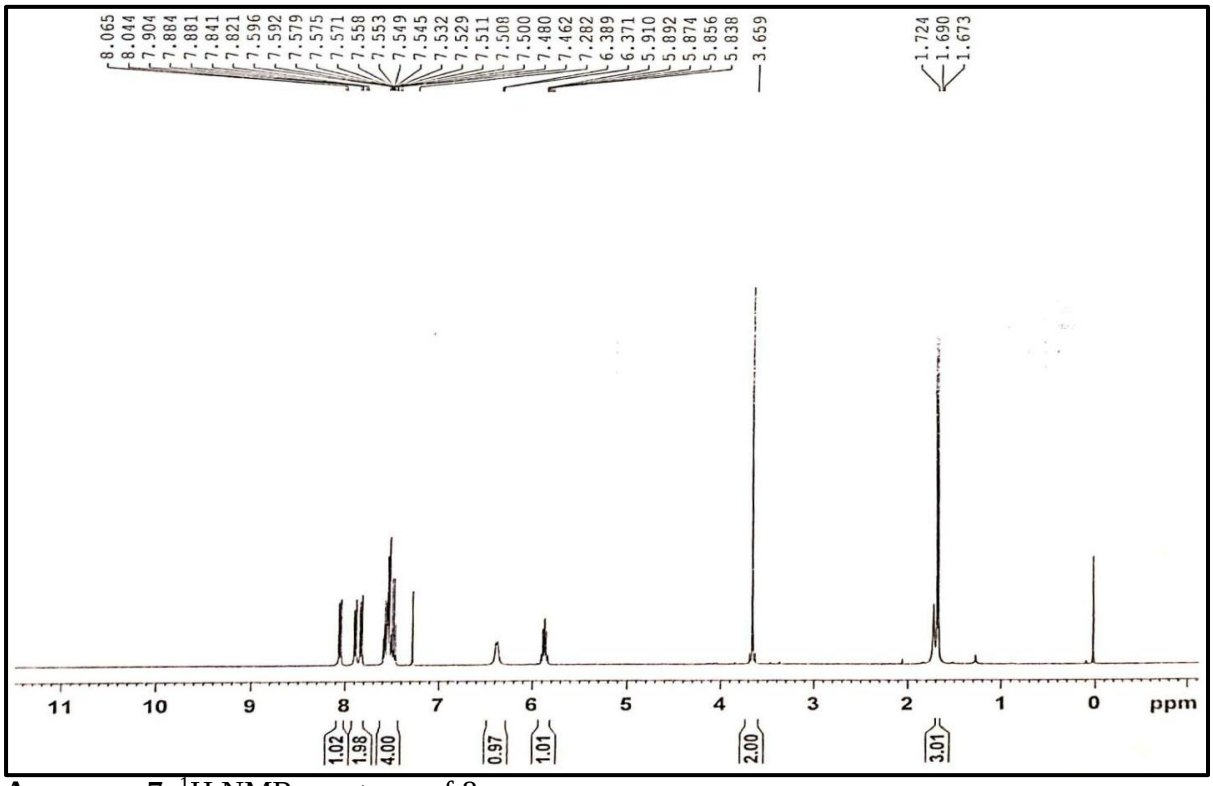


**Annexure 7.** $^{1}$H NMR spectrum of 8.

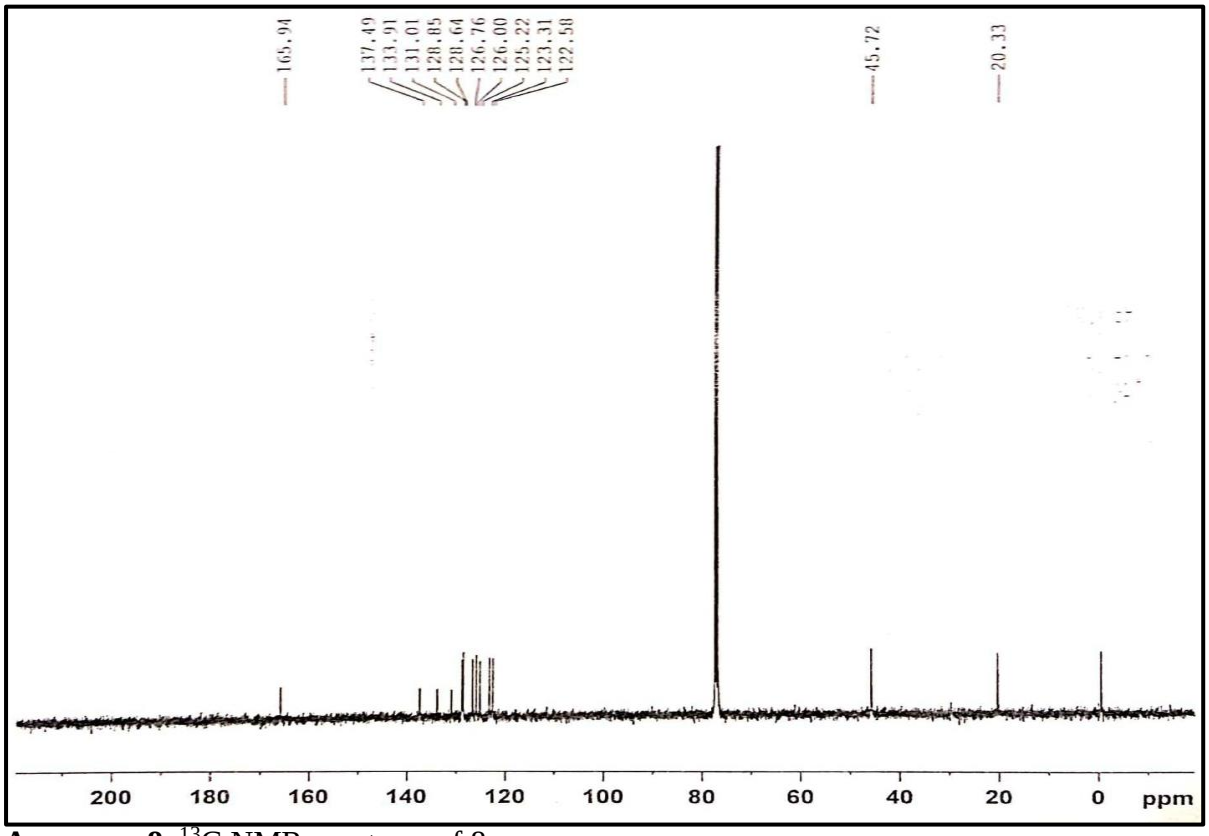


**Annexure 8**. $^{13}$C NMR spectrum of 8

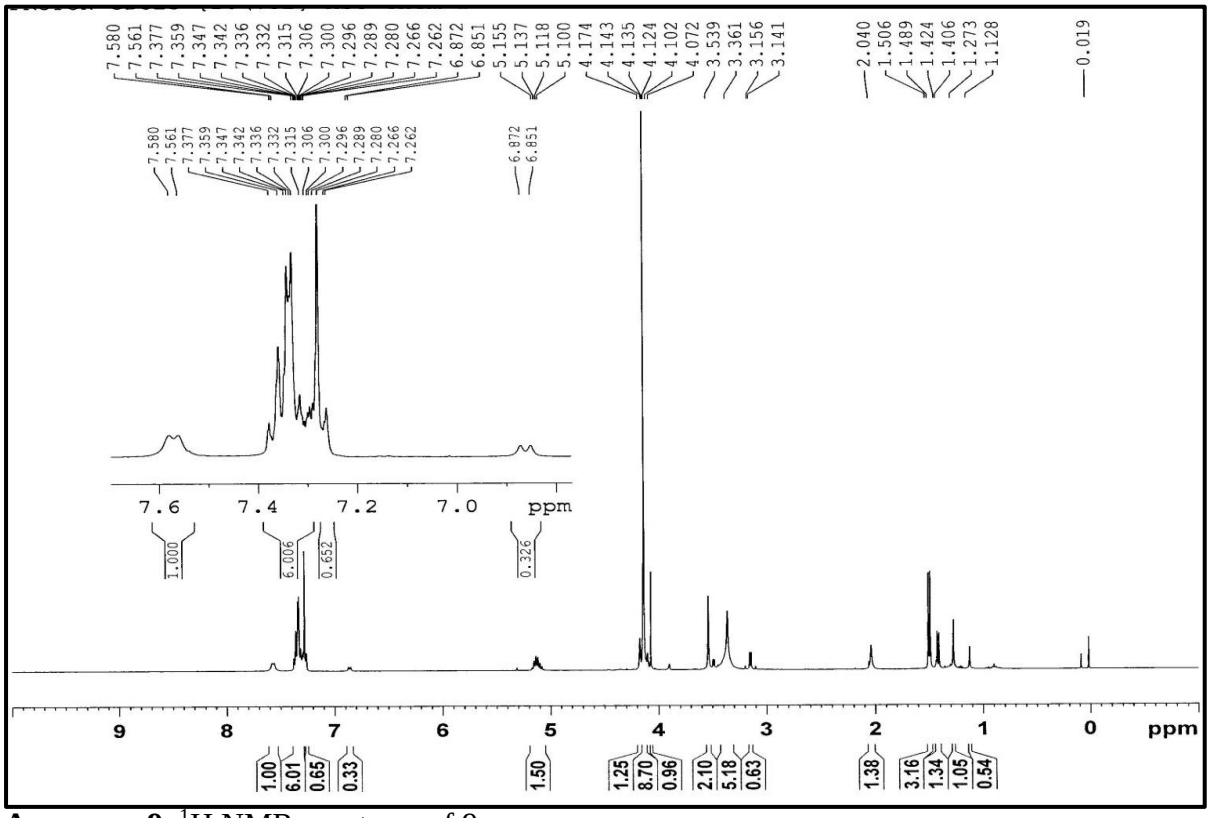


**Annexure 9**. $^{1}$H NMR spectrum of 9.

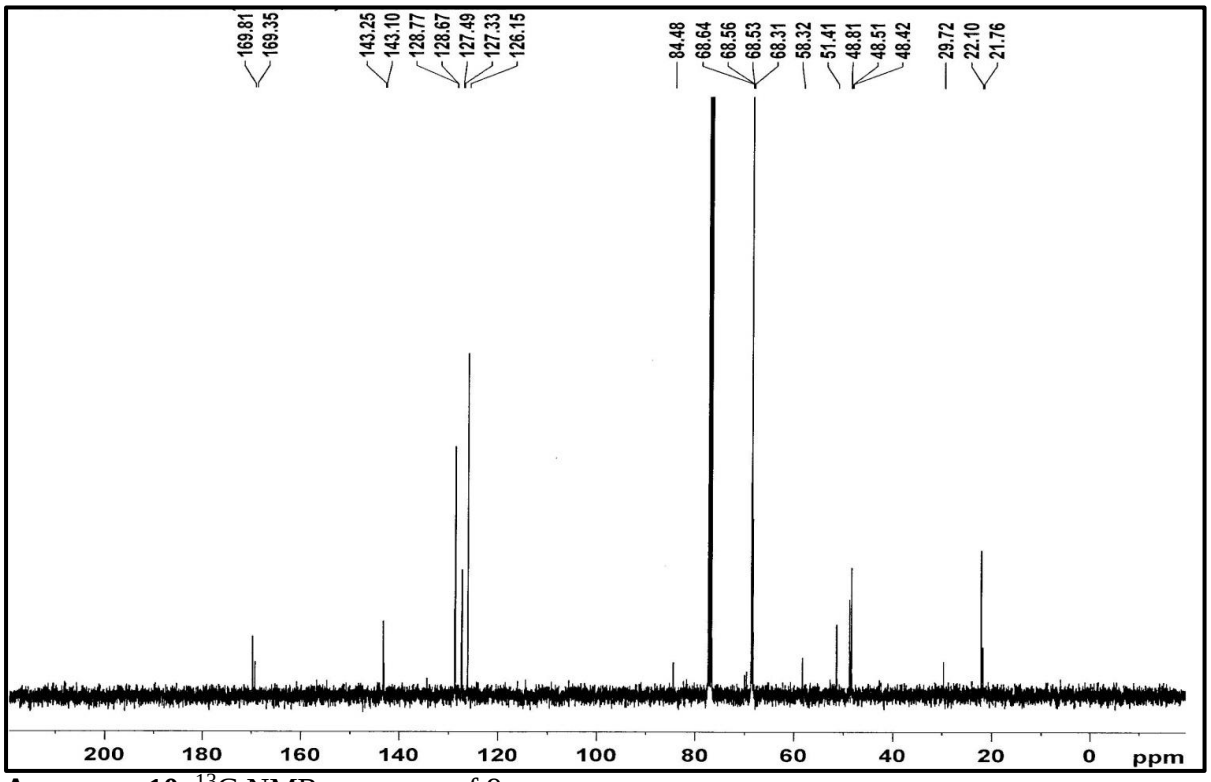


**Annexure 10.** $^{13}$C NMR spectrum of 9.

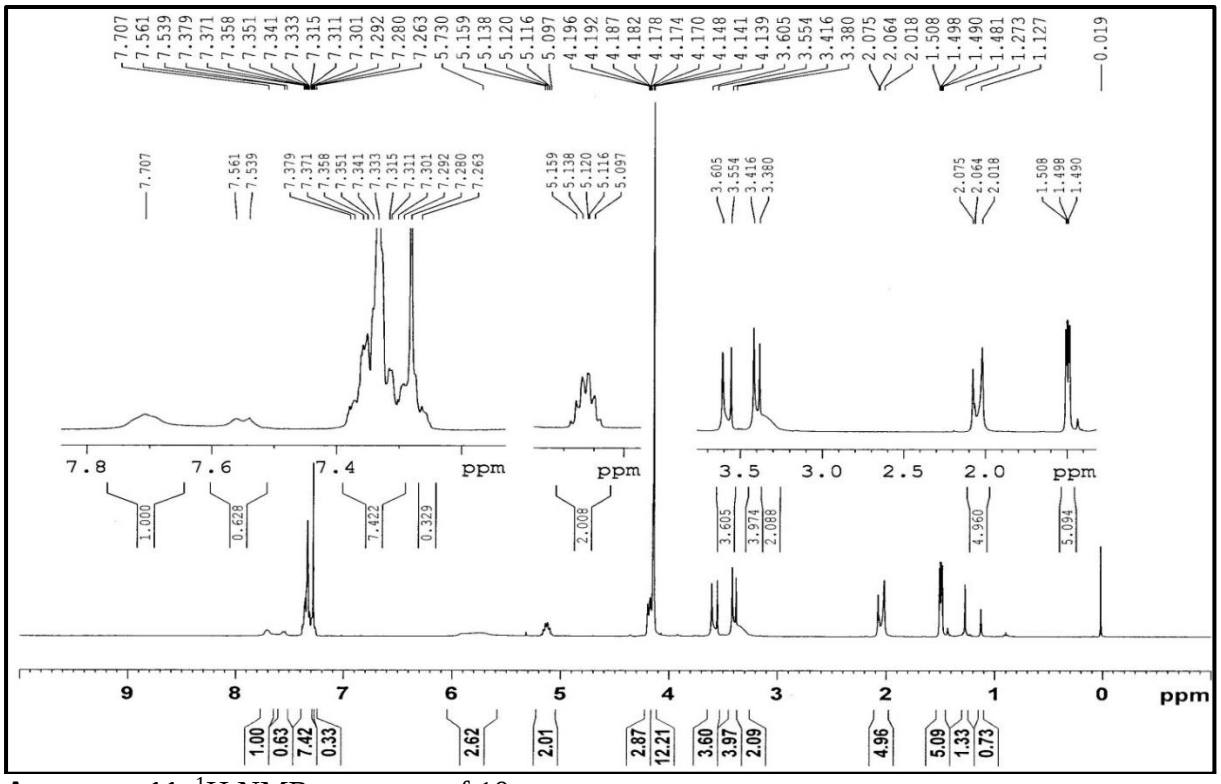

**Annexure 11**. $^{1}$H NMR spectrum of 10.

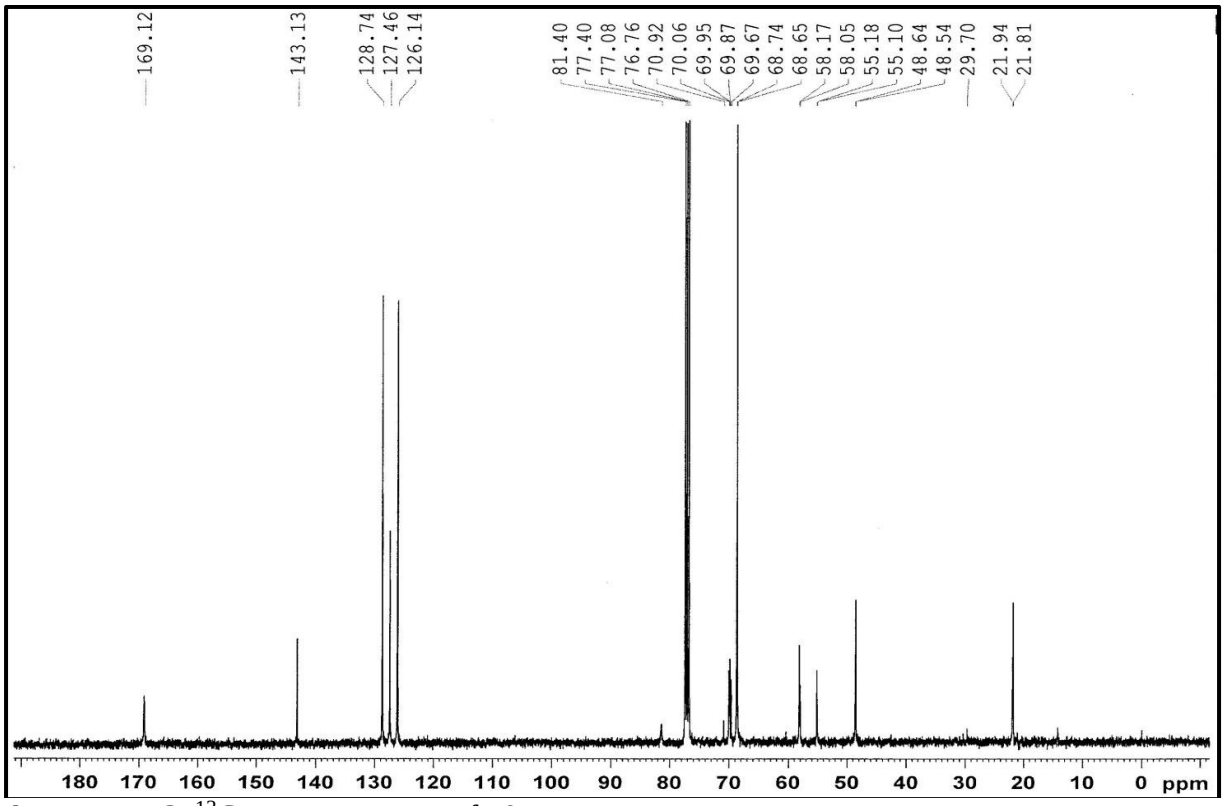

**Annexure 12.** $^{13}$C NMR spectrum of 10.

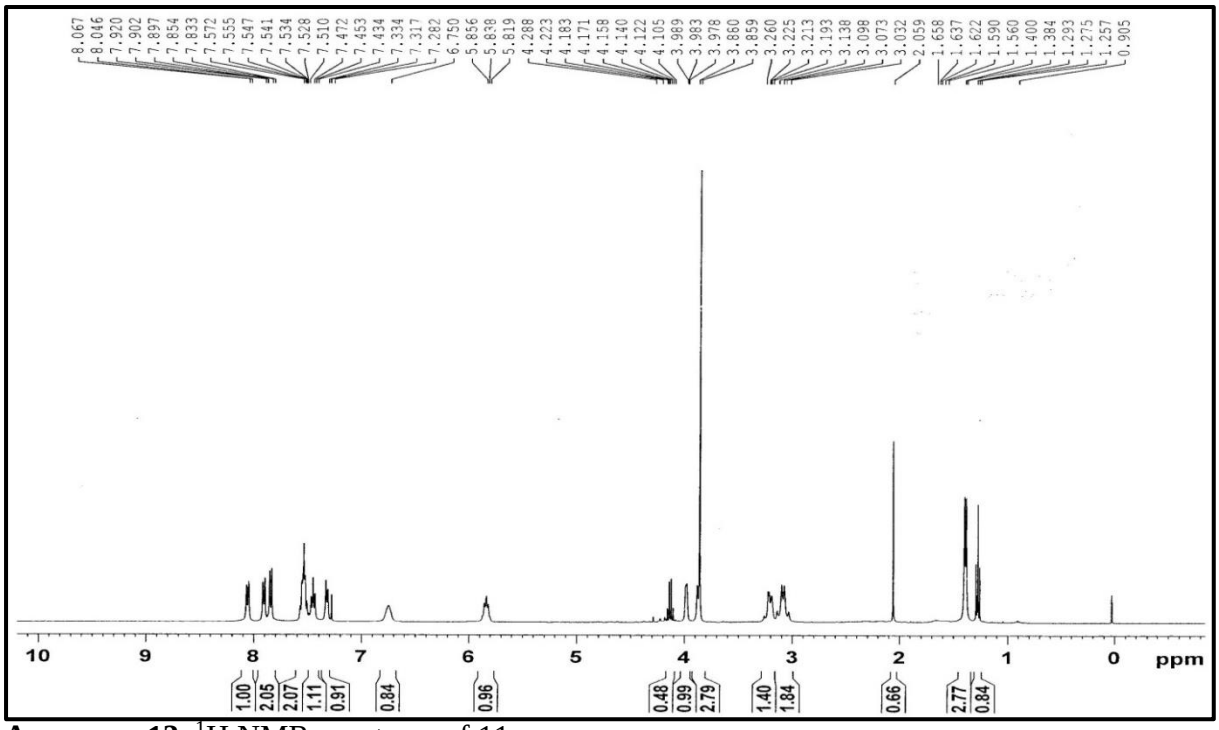


**Annexure 13.** $^{1}$H NMR spectrum of 11.

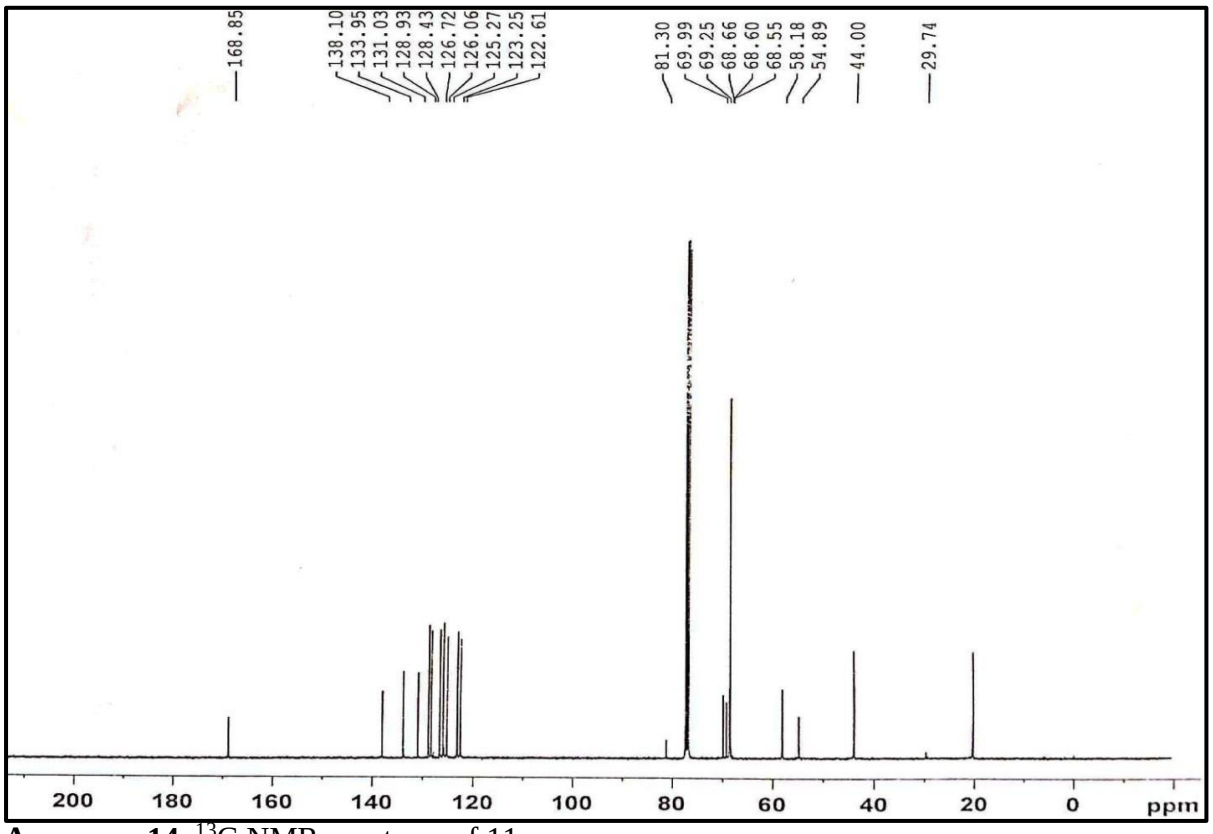


**Annexure 14**. $^{13}$C NMR spectrum of 11.

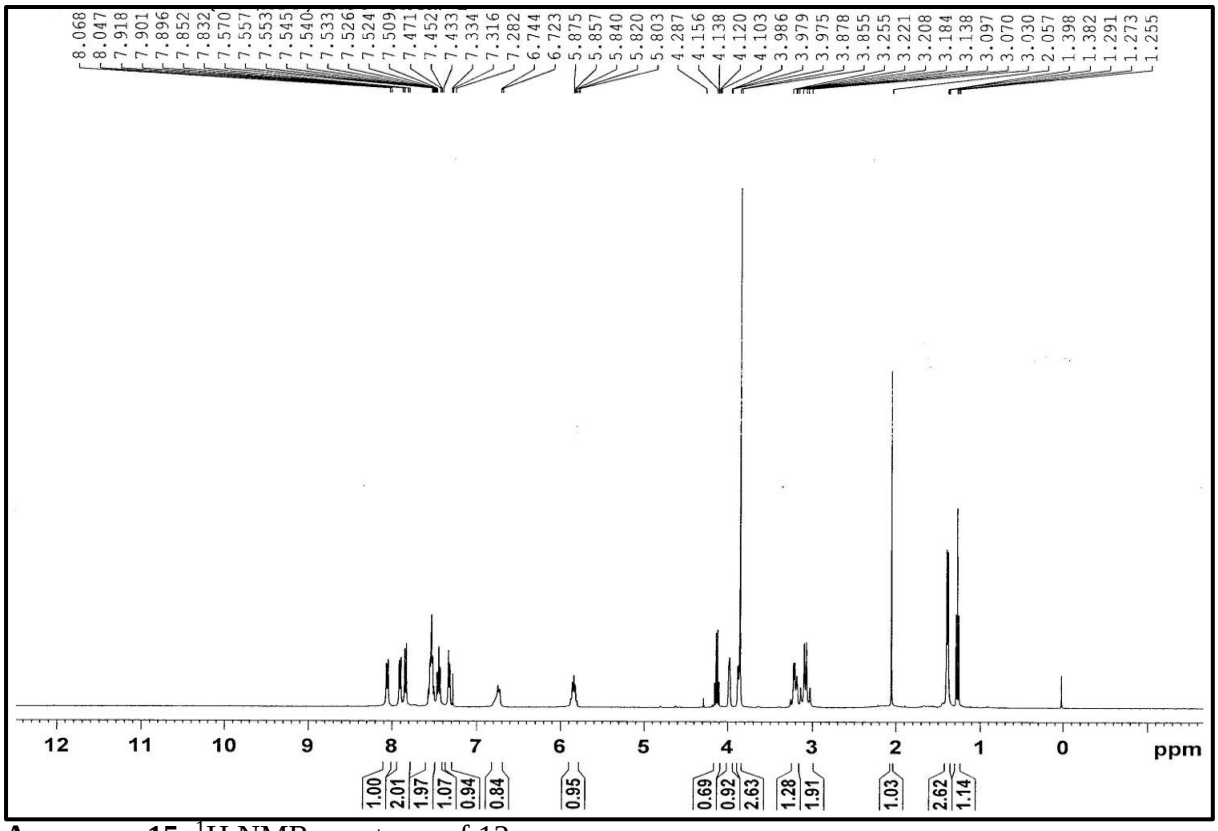


**Annexure 15.** $^{1}$H NMR spectrum of 12.

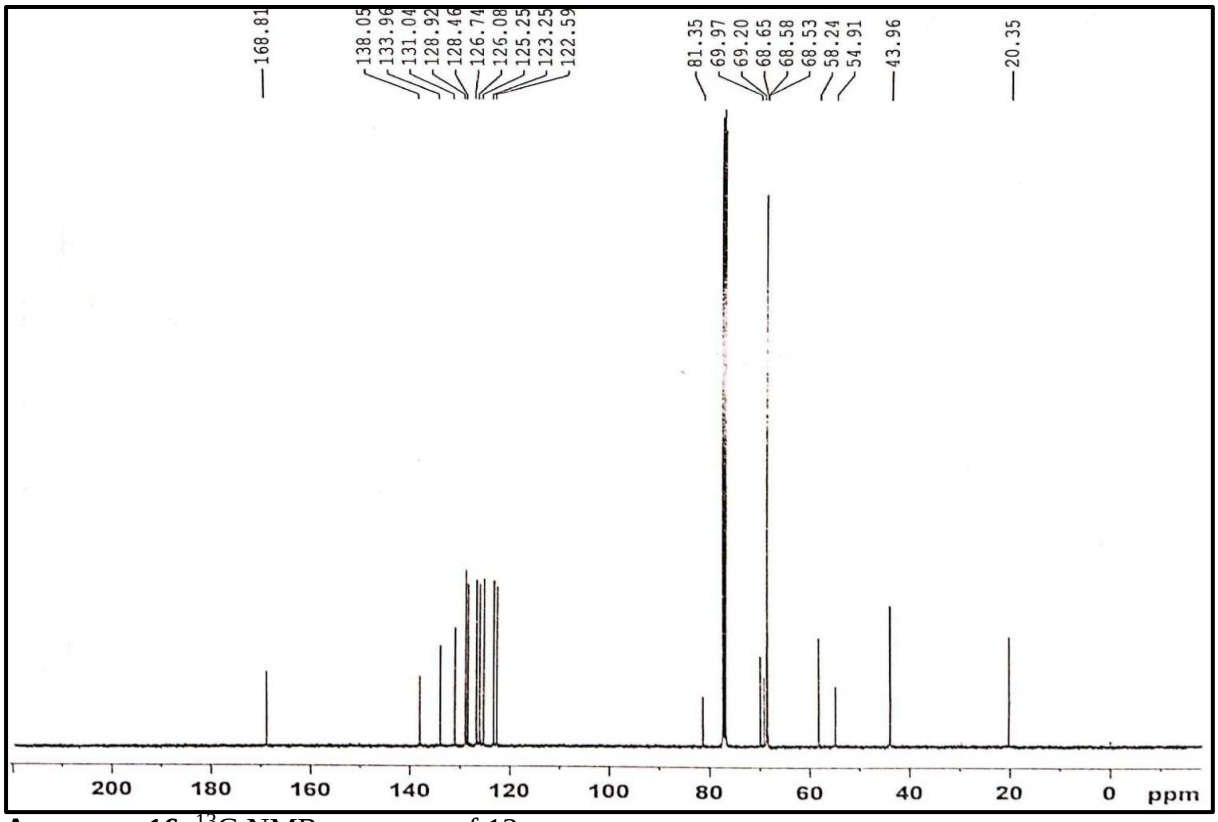


**Annexure 16**. $^{13}$C NMR spectrum of 12.

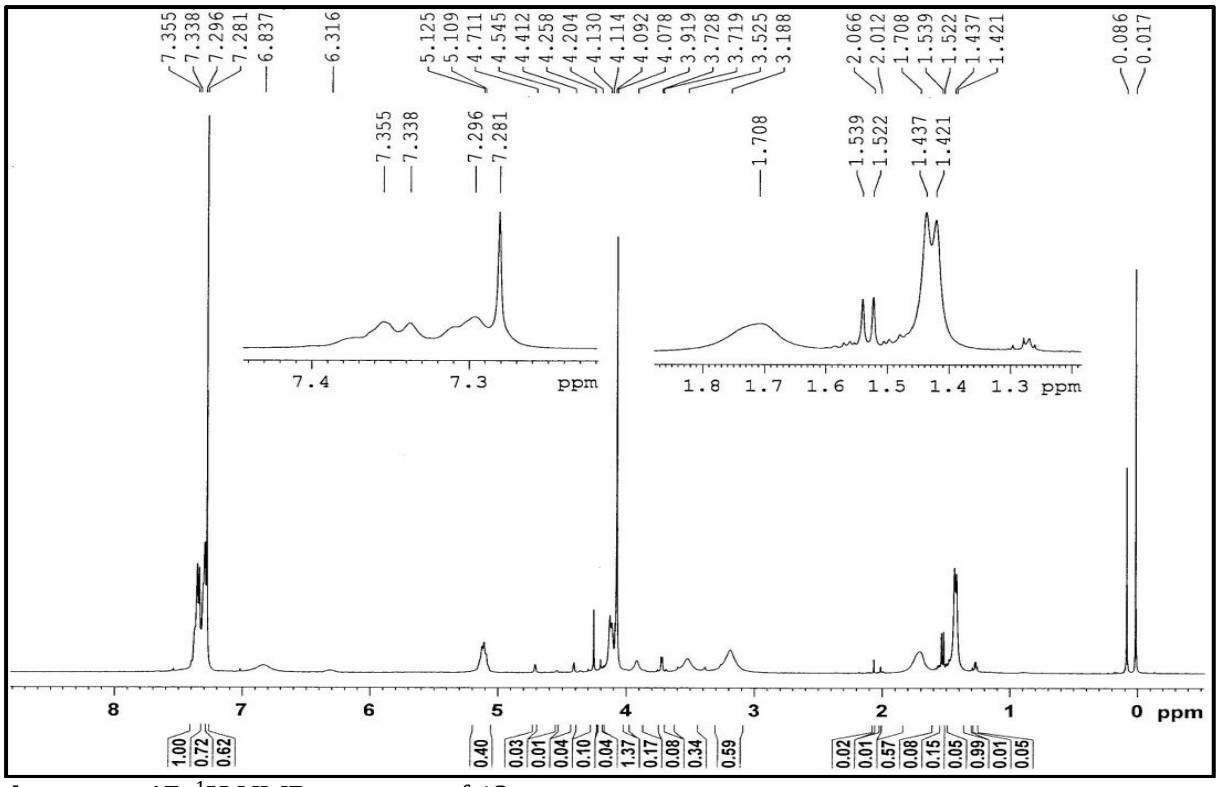


**Annexure 17**. $^{1}$H NMR spectrum of 13.

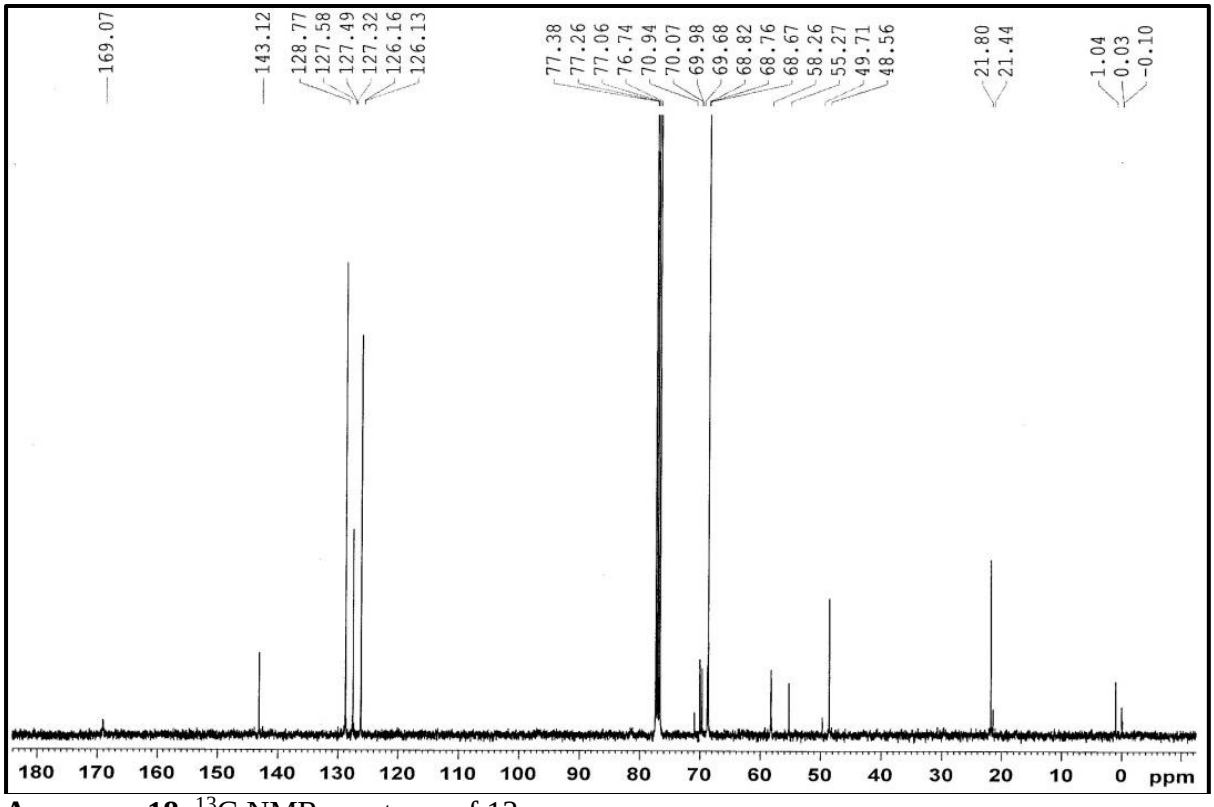


**Annexure 18.** $^{13}$C NMR spectrum of 13.

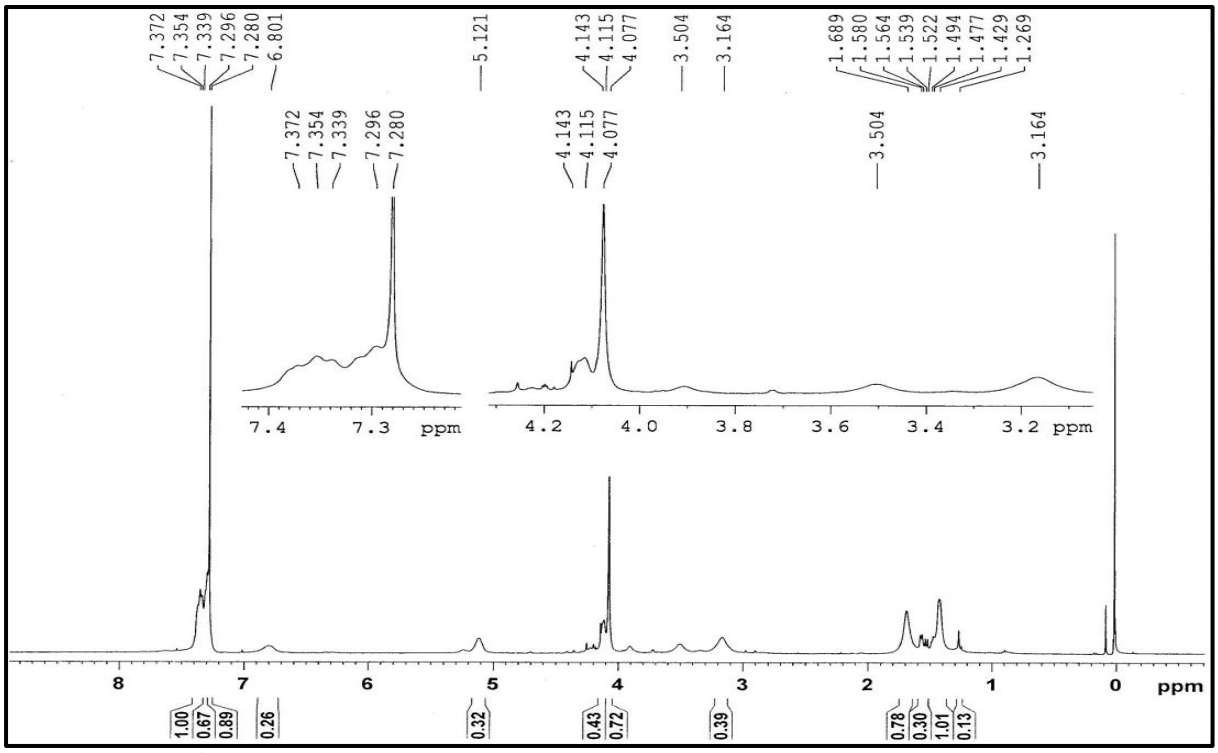


**Annexure 19**. $^{1}$H NMR spectrum of 14.

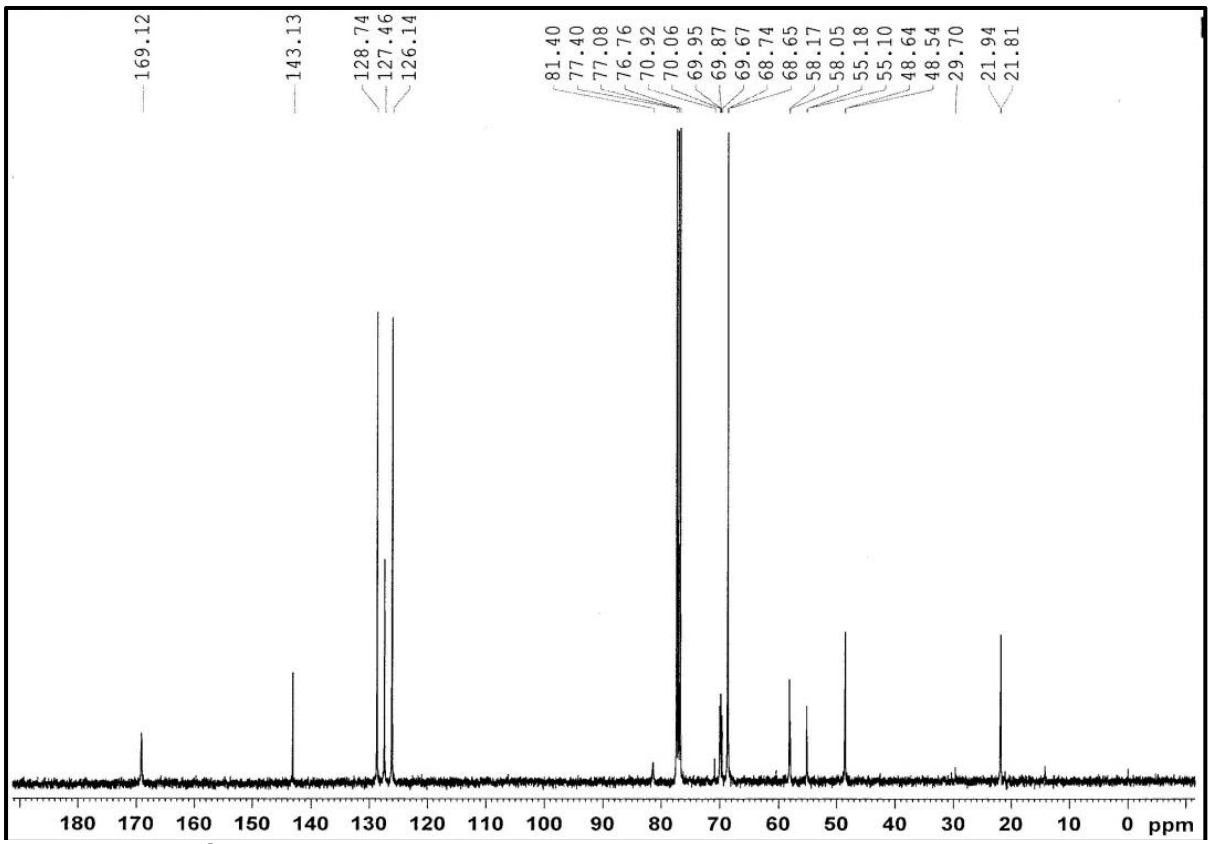


**Annexure 20.** $^{13}$C NMR spectrum of 14.

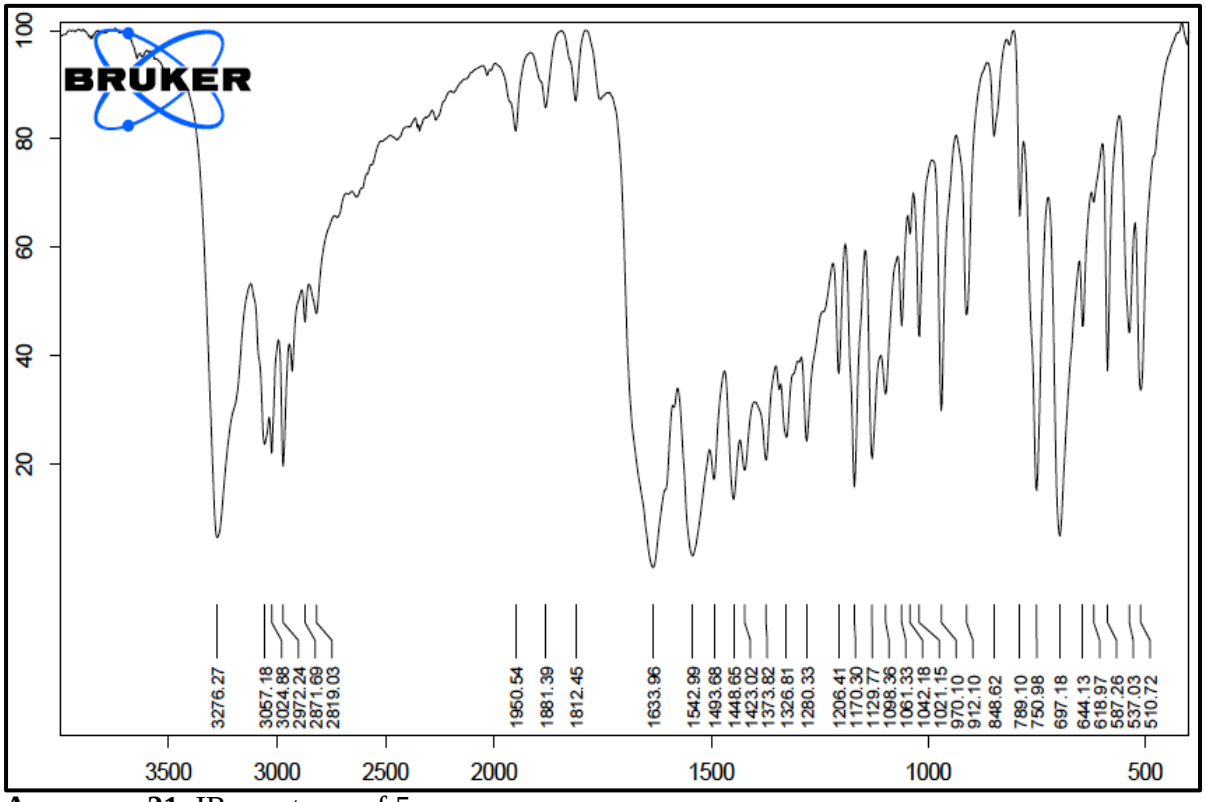


**Annexure 21.** IR spectrum of 5.

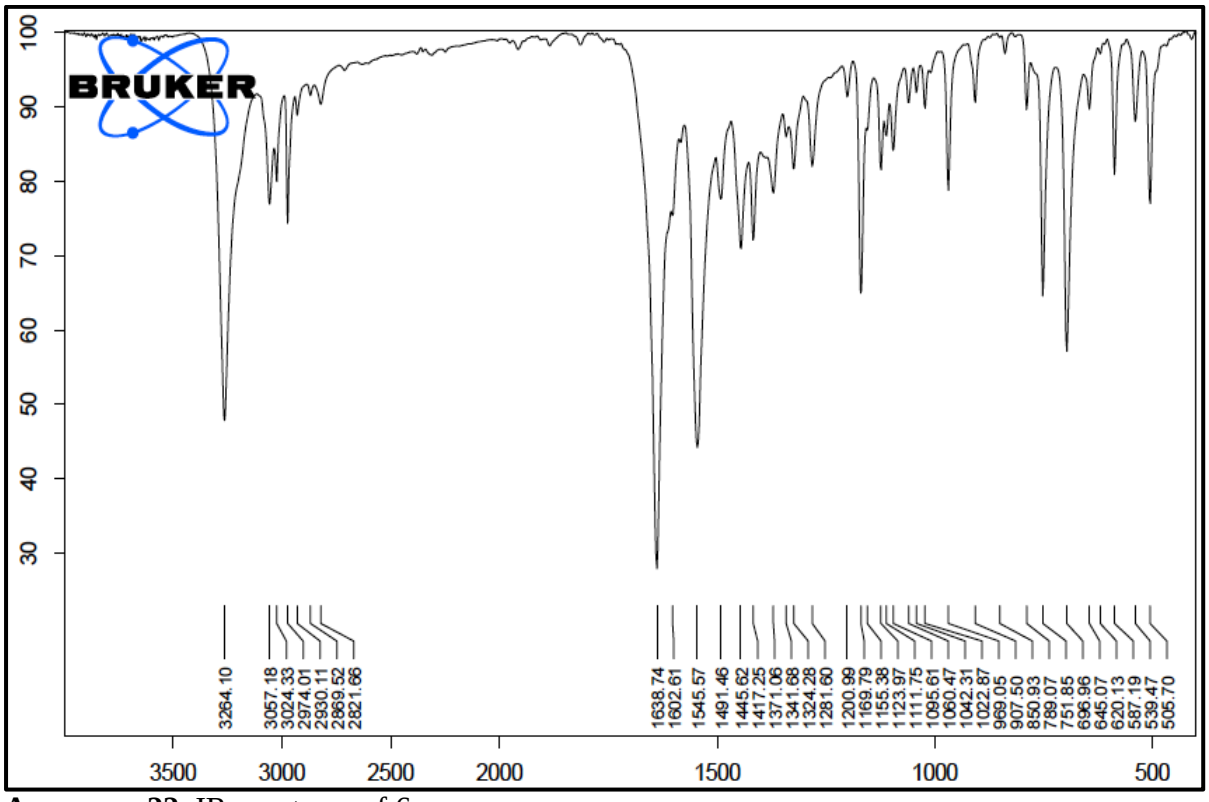


**Annexure 22.** IR spectrum of 6.

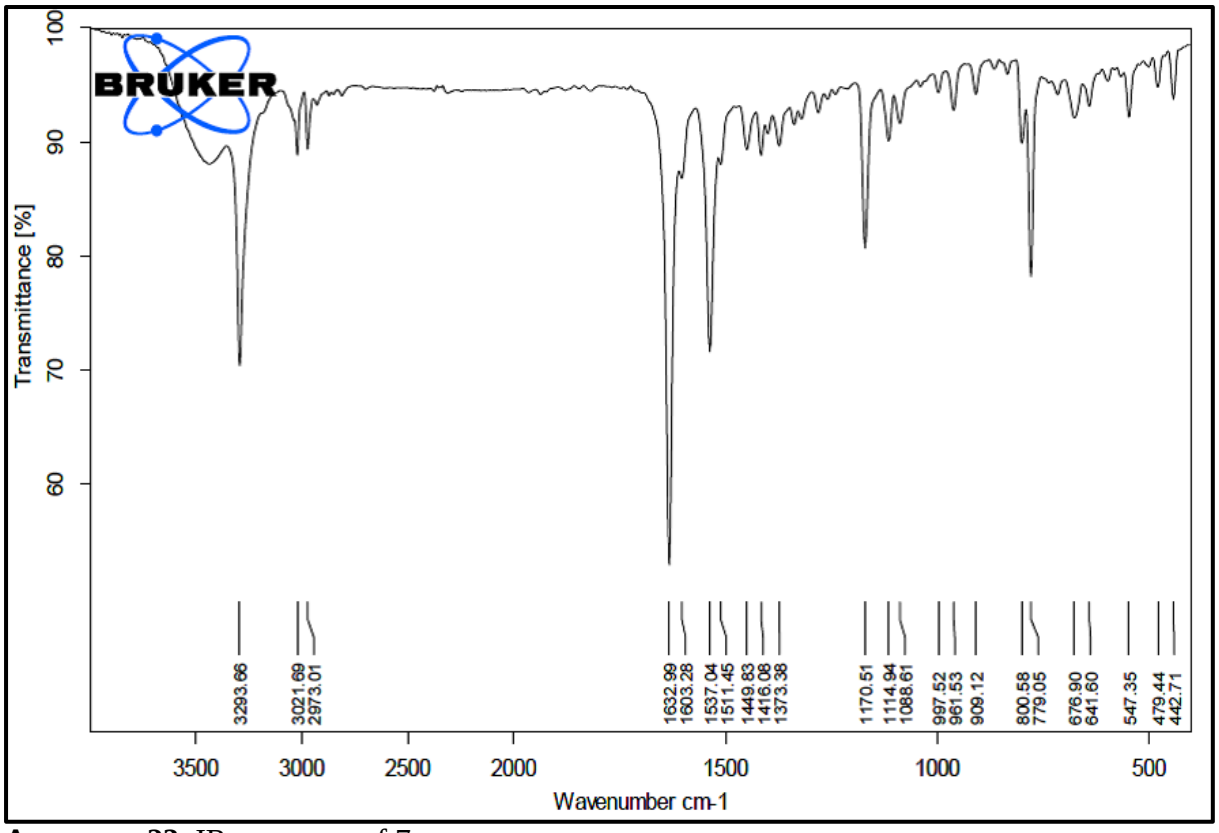


**Annexure 23.** IR spectrum of 7.

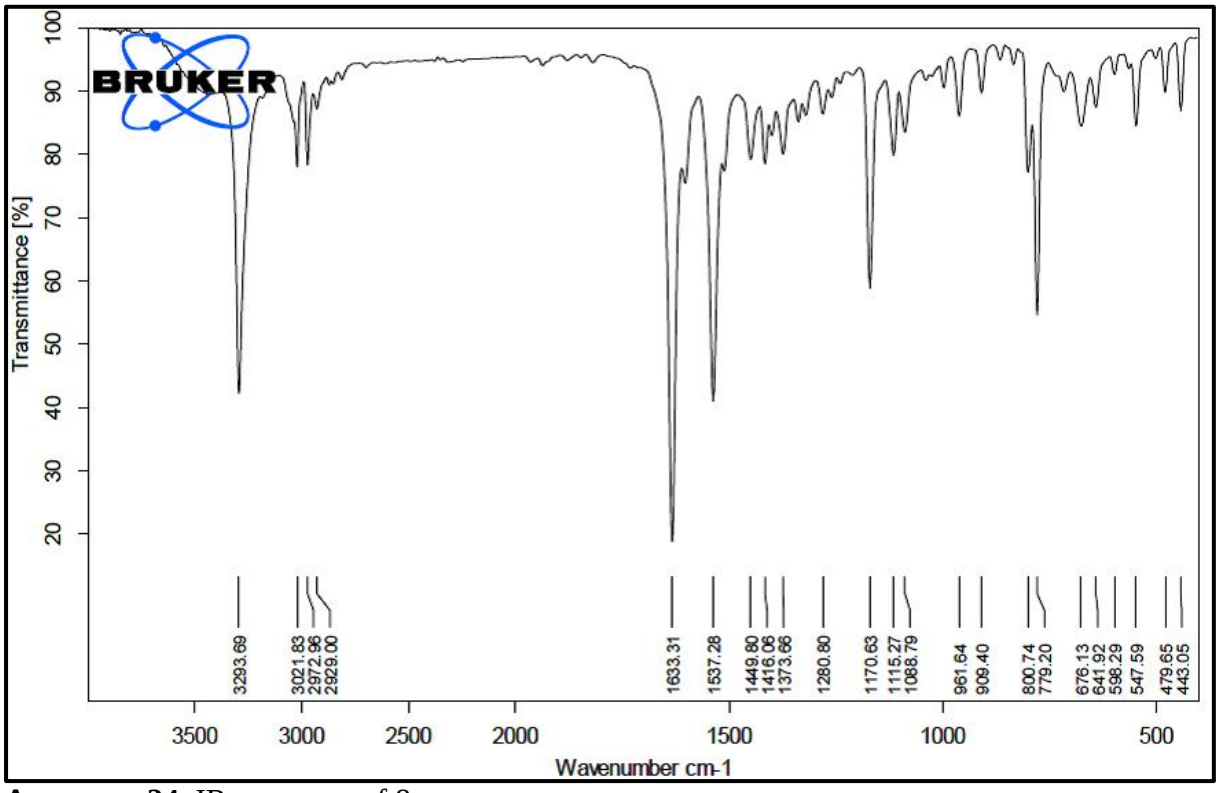


**Annexure 24.** IR spectrum of 8.

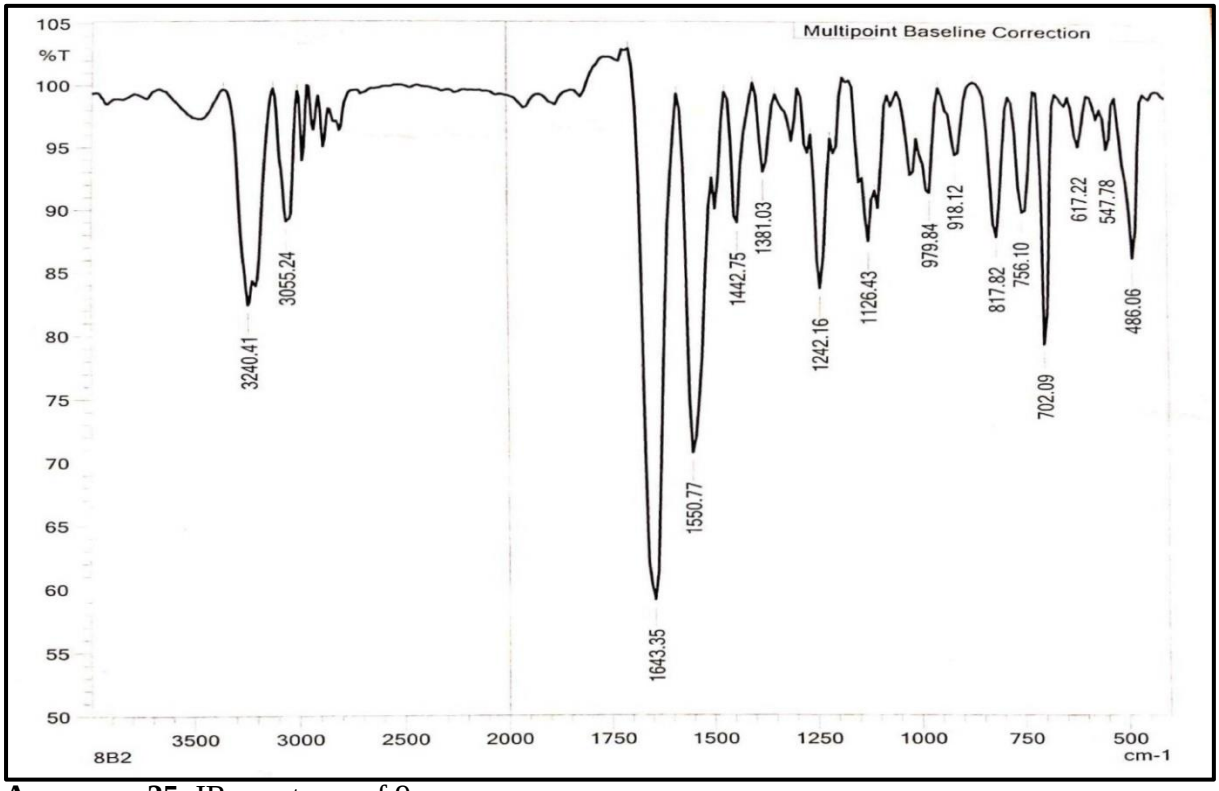


**Annexure 25.** IR spectrum of 9.

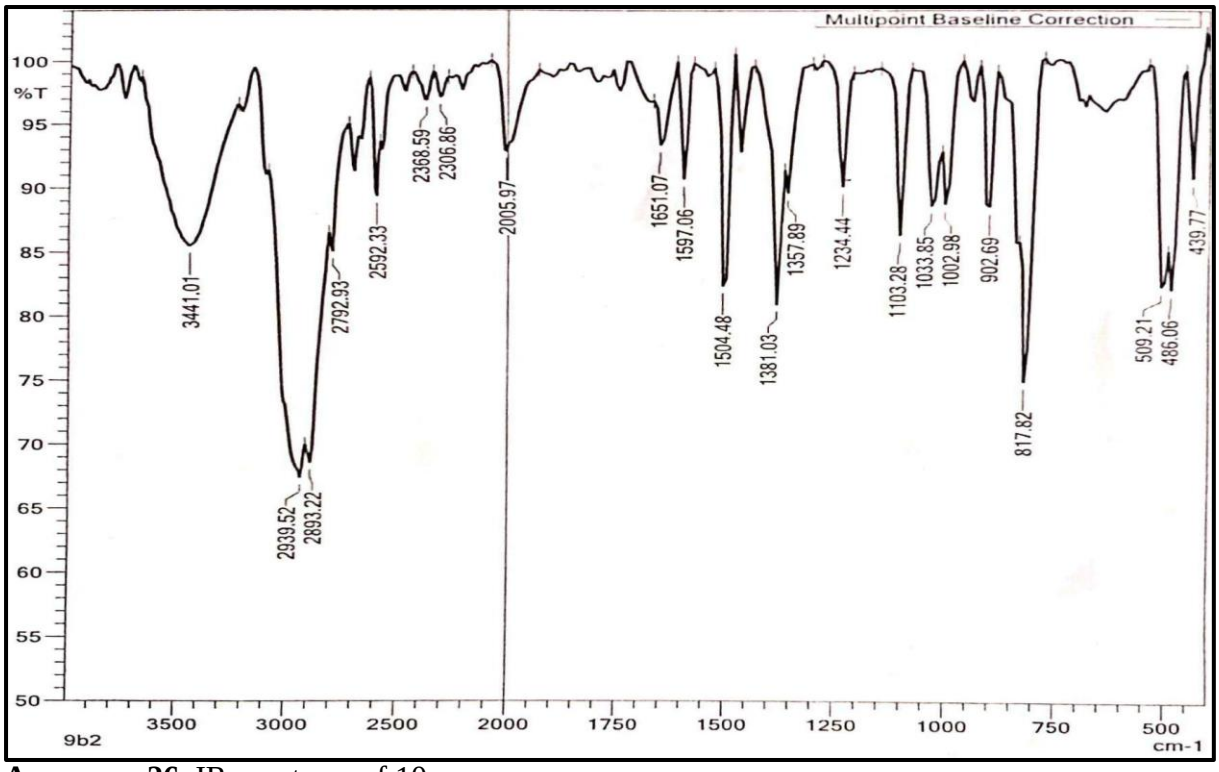


**Annexure 26.** IR spectrum of 10.

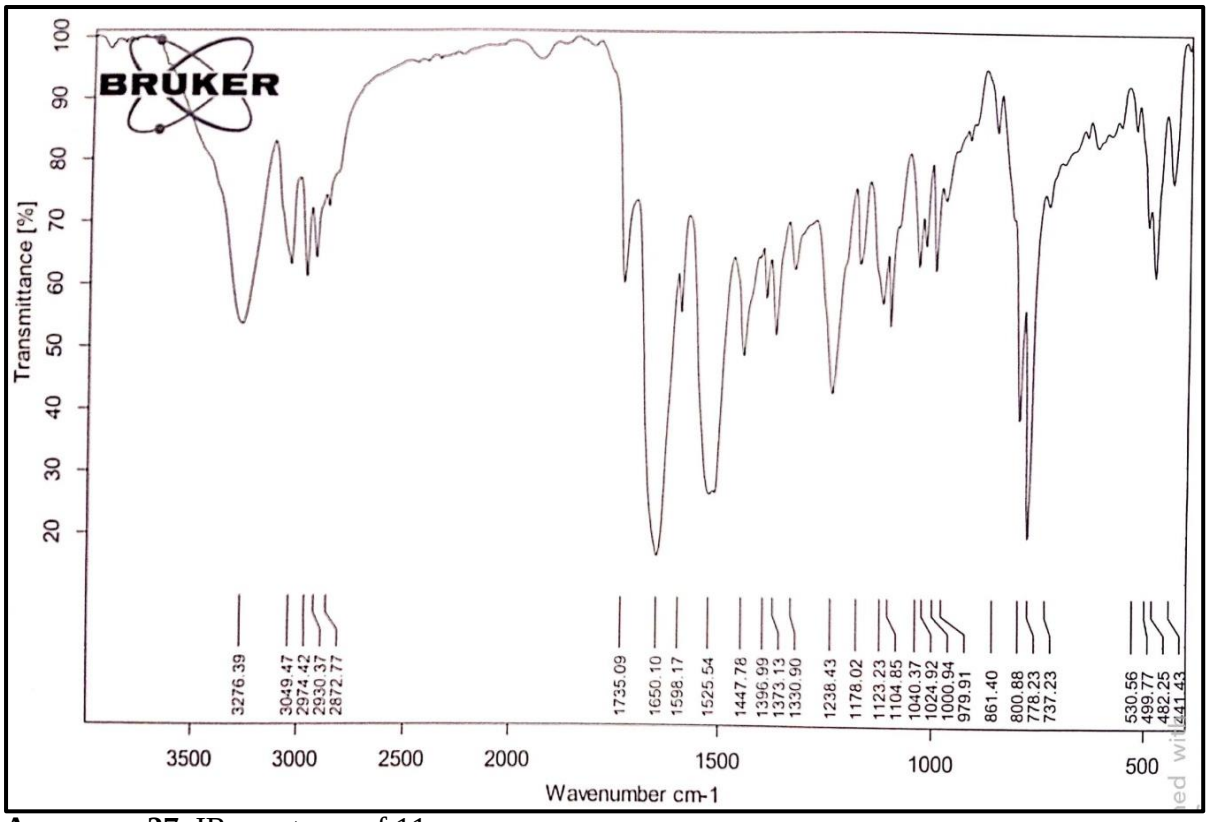


**Annexure 27.** IR spectrum of 11.

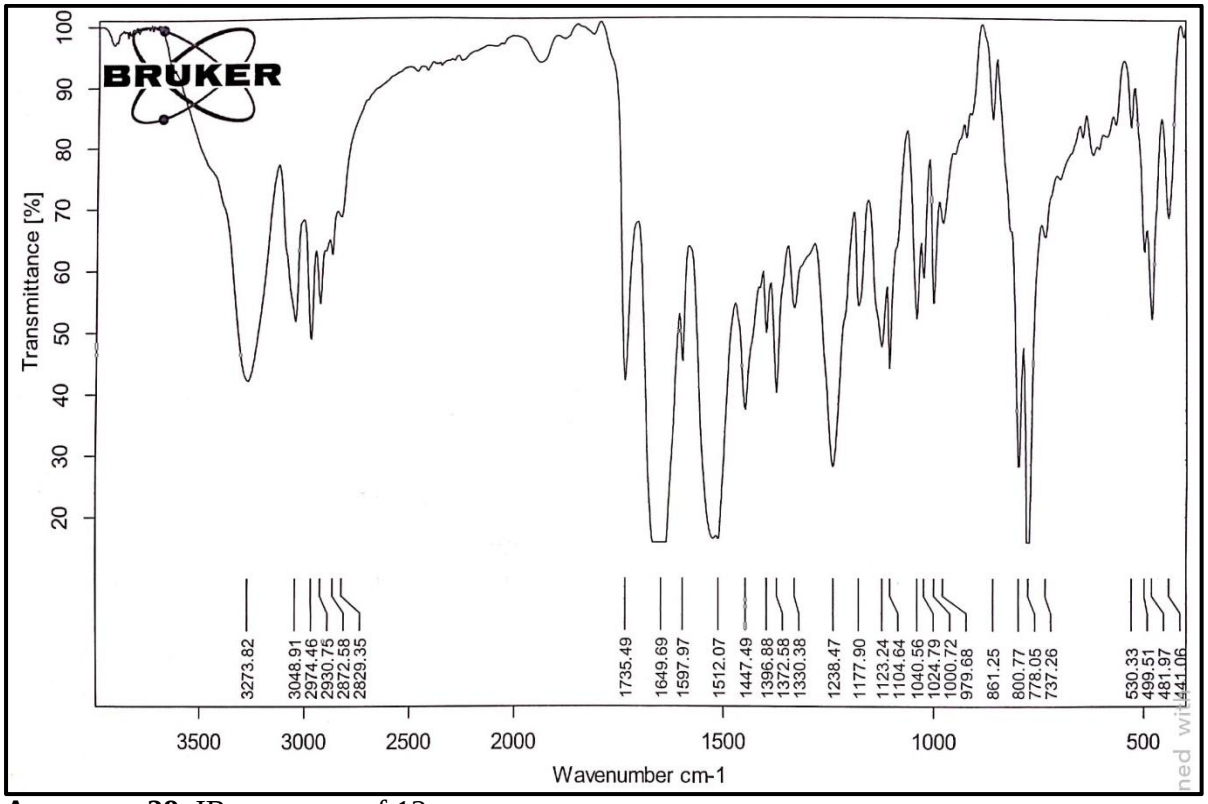


**Annexure 28.** IR spectrum of 12.

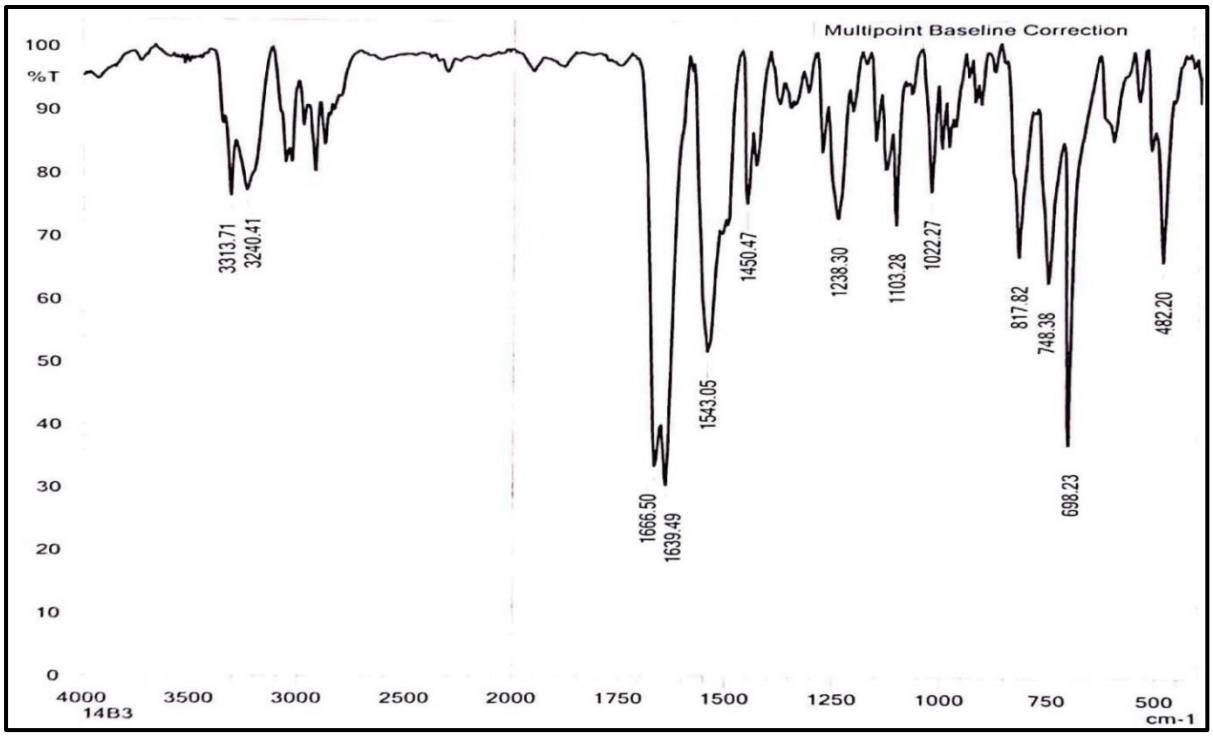


**Annexure 29.** IR spectrum of 13.

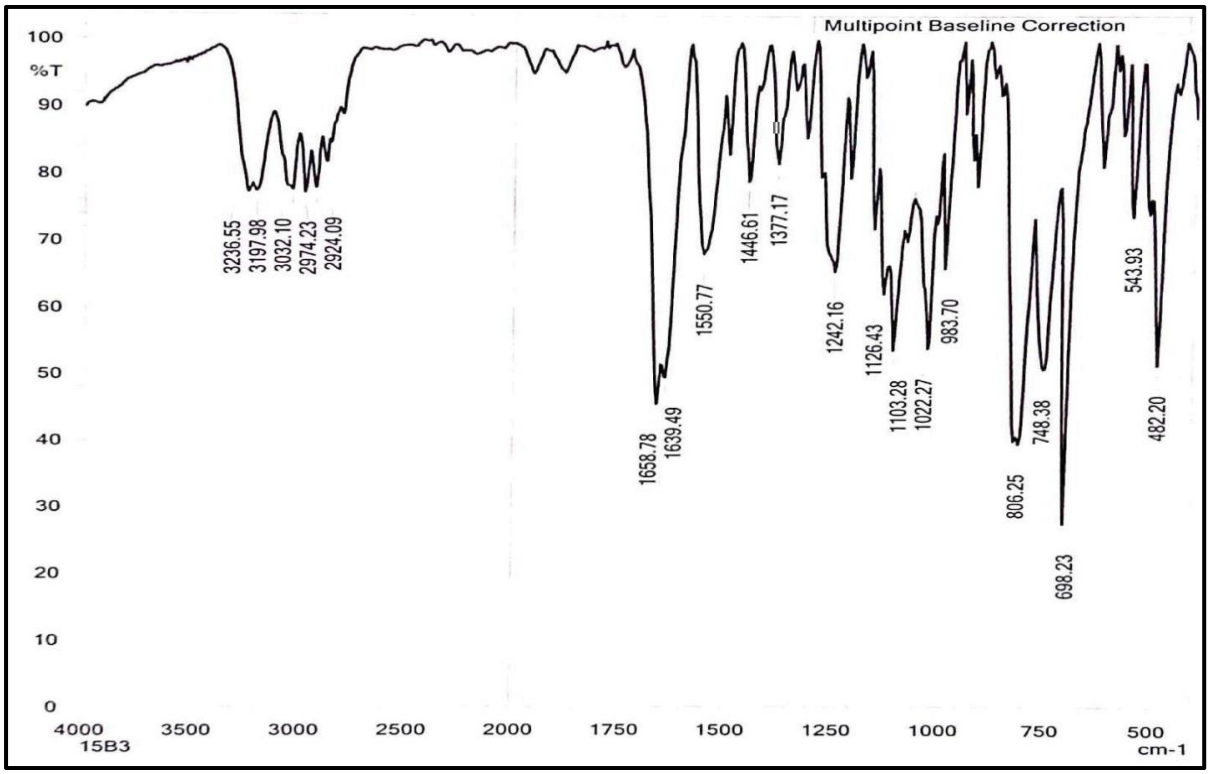


**Annexure 30.** IR spectrum of 14.

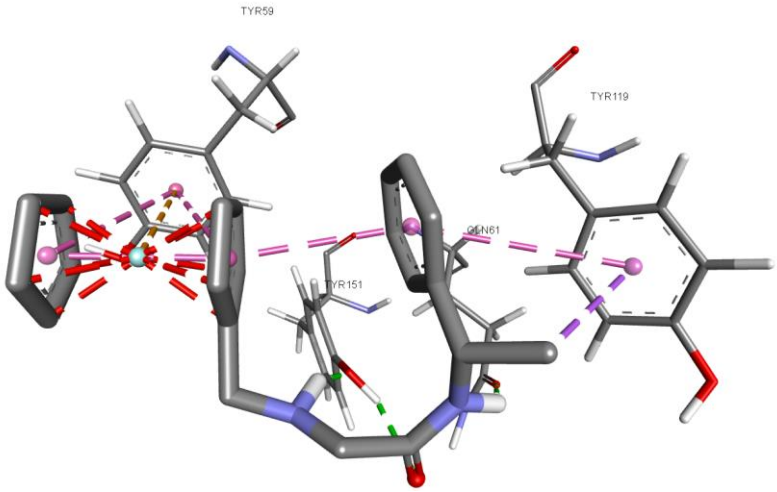


**Annexure 31.** Binding of inhibitors S-(-)-**9** with TNFα receptor using ICM-browser. Non-Bonding interactions elucidated using & Discovery Studios Visualizer 21.0.

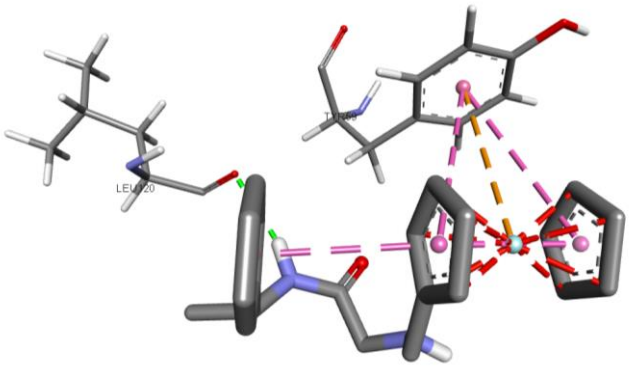

**Annexure 32.** Binding of inhibitors R-(+)-10 with TNFα receptor using ICM-browser. Non-Bonding interactions elucidated using & Discovery Studios Visualizer 21.0.

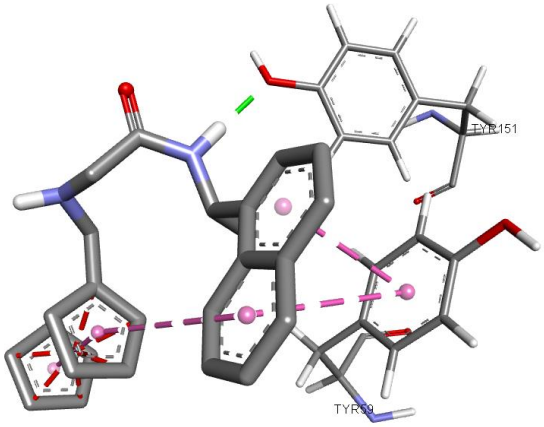


**Annexure 33.** Binding of inhibitors S-(-)-11 with TNFα receptor using ICM-browser. Non-Bonding interactions elucidated using & Discovery Studios Visualizer 21.0.

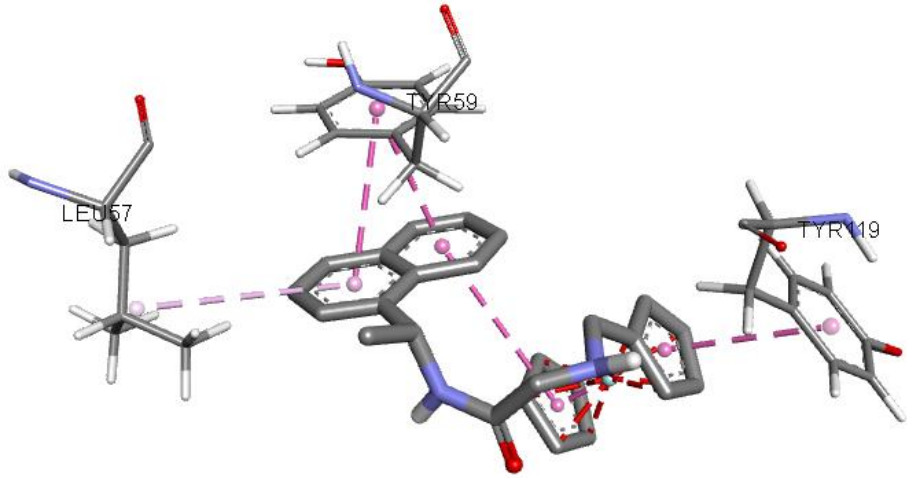


**Annexure 34.** Binding of inhibitors R-(+)-12 with TNFα receptor using ICM-browser. Non-Bonding interactions elucidated using & Discovery Studios Visualizer 21.0.

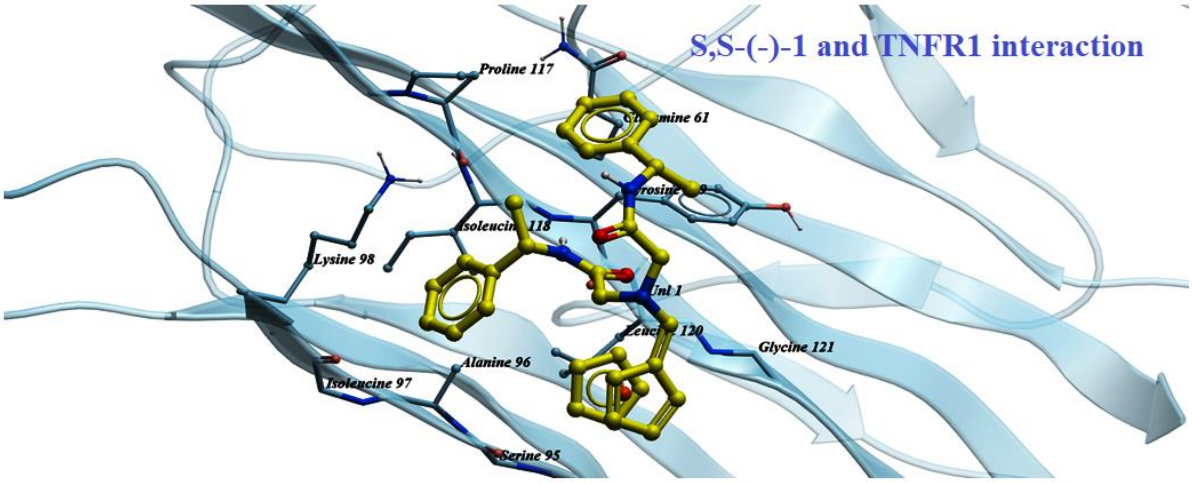


| | Name | Visible | Color | Parent | Distance | Category | Types | From | From Chemistry | To | To Chemistry |
|---|---|---|---|---|---|---|---|---|---|---|---|
| 1 | A:GLY121:N - :UNL1:C | Yes | | Ligand Non-bond Monitor | 3.33252 | Hydrogen Bond | Conventional Hydrogen Bond | A:GLY1... | H-Donor | :UNL... | H-Acceptor |
| 2 | :UNL1:C - :UNL1 | Yes | | Ligand Non-bond Monitor | 3.66973 | Electrostatic | Pi-Cation | :UNL1:C | Positive | :UNL1 | Pi-Orbitals |
| 3 | :UNL1:C - :UNL1 | Yes | | Ligand Non-bond Monitor | 4.68158 | Electrostatic | Pi-Cation | :UNL1:C | Positive | :UNL1 | Pi-Orbitals |
| 4 | A:LEU120:CD1 - :UNL1 | Yes | | Ligand Non-bond Monitor | 3.54925 | Hydrophobic | Pi-Sigma | A:LEU1... | C-H | :UNL1 | Pi-Orbitals |
| 5 | :UNL1 - :UNL1 | Yes | | Ligand Non-bond Monitor | 3.45113 | Hydrophobic | Pi-Pi Stacked | :UNL1 | Pi-Orbitals | :UNL1 | Pi-Orbitals |
| 6 | :UNL1 - A:PRO117 | Yes | | Ligand Non-bond Monitor | 4.85816 | Hydrophobic | Pi-Alkyl | :UNL1 | Pi-Orbitals | A:PR... | Alkyl |
| 7 | :UNL1 - A:PRO117 | Yes | | Ligand Non-bond Monitor | 5.32927 | Hydrophobic | Pi-Alkyl | :UNL1 | Pi-Orbitals | A:PR... | Alkyl |
| 8 | :UNL1 - A:ALA96 | Yes | | Ligand Non-bond Monitor | 4.2815 | Hydrophobic | Pi-Alkyl | :UNL1 | Pi-Orbitals | A:AL... | Alkyl |
| 9 | :UNL1 - A:LYS98 | Yes | | Ligand Non-bond Monitor | 4.79948 | Hydrophobic | Pi-Alkyl | :UNL1 | Pi-Orbitals | A:LY... | Alkyl |
| 10 | :UNL1 - A:ILE118 | Yes | | Ligand Non-bond Monitor | 4.54844 | Hydrophobic | Pi-Alkyl | :UNL1 | Pi-Orbitals | A:ILE... | Alkyl |
| 11 | :UNL1 - A:LEU94 | Yes | | Ligand Non-bond Monitor | 4.91871 | Hydrophobic | Pi-Alkyl | :UNL1 | Pi-Orbitals | A:LE... | Alkyl |
| 12 | :UNL1 - A:ALA96 | Yes | | Ligand Non-bond Monitor | 5.39974 | Hydrophobic | Pi-Alkyl | :UNL1 | Pi-Orbitals | A:AL... | Alkyl |

**Annexure 35.** Binding of inhibitors S,S-(-)-**13** with TNFα receptor using ICM-browser. Non-Bonding interactions elucidated using & Discovery Studios Visualizer 21.0.

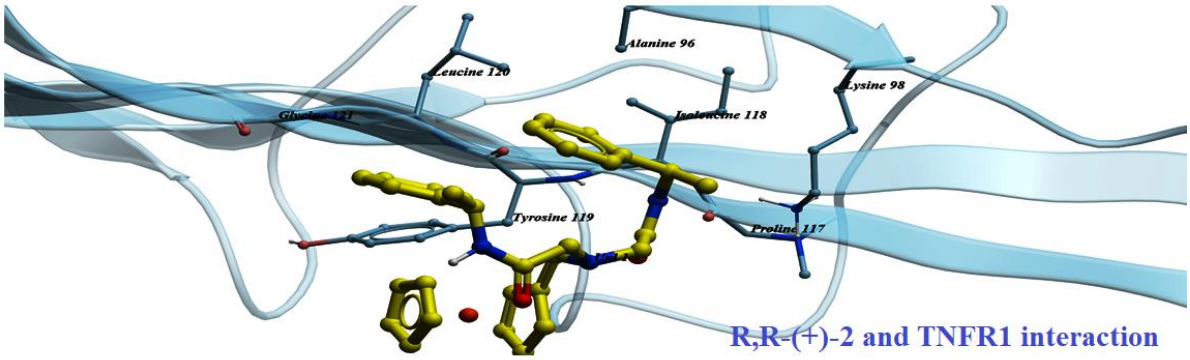


| | Name | Visible | Color | Parent | Distance | Category | Types | From | From Chemistry | To | To Chemistry |
|---|---|---|---|---|---|---|---|---|---|---|---|
| 1 | A:LYS98:HZ1 - :UNL1:H | Yes | | Ligand Non-bond Monitor | 2.72377 | Hydrogen Bond | Conventional Hydrogen Bond | A:LYS98:HZ1 | H-Donor | :UNL1:H | H-Acceptor |
| 2 | A:TYR119:HN - :UNL1:H | Yes | | Ligand Non-bond Monitor | 2.3137 | Hydrogen Bond | Conventional Hydrogen Bond | A:TYR119:HN | H-Donor | :UNL1:H | H-Acceptor |
| 3 | :UNL1:O - :UNL1:C | Yes | | Ligand Non-bond Monitor | 3.34029 | Hydrogen Bond | Conventional Hydrogen Bond | :UNL1:O | H-Donor | :UNL1:C | H-Acceptor |
| 4 | :UNL1:O - :UNL1:C | Yes | | Ligand Non-bond Monitor | 2.97298 | Hydrogen Bond | Conventional Hydrogen Bond | :UNL1:O | H-Donor | :UNL1:C | H-Acceptor |
| 5 | :UNL1:O - A:PRO117:O | Yes | | Ligand Non-bond Monitor | 2.90628 | Hydrogen Bond | Conventional Hydrogen Bond | :UNL1:O | H-Donor | A:PRO117:O | H-Acceptor |
| 6 | A:ILE118:CA - :UNL1:H | Yes | | Ligand Non-bond Monitor | 2.49137 | Hydrogen Bond | Carbon Hydrogen Bond | A:ILE118:CA | H-Donor | :UNL1:H | H-Acceptor |
| 7 | :UNL1:N - :UNL1 | Yes | | Ligand Non-bond Monitor | 4.44434 | Electrostatic | Pi-Cation | :UNL1:N | Positive | :UNL1 | Pi-Orbitals |
| 8 | :UNL1:C - :UNL1 | Yes | | Ligand Non-bond Monitor | 3.66878 | Electrostatic | Pi-Cation | :UNL1:C | Positive | :UNL1 | Pi-Orbitals |
| 9 | :UNL1:C - :UNL1 | Yes | | Ligand Non-bond Monitor | 4.25963 | Electrostatic | Pi-Cation | :UNL1:C | Positive | :UNL1 | Pi-Orbitals |
| 10 | A:ALA96:CB - :UNL1 | Yes | | Ligand Non-bond Monitor | 3.89606 | Hydrophobic | Pi-Sigma | A:ALA96:CB | C-H | :UNL1 | Pi-Orbitals |
| 11 | :UNL1 - :UNL1 | Yes | | Ligand Non-bond Monitor | 3.45074 | Hydrophobic | Pi-Pi Stacked | :UNL1 | Pi-Orbitals | :UNL1 | Pi-Orbitals |
| 12 | :UNL1 - :UNL1 | Yes | | Ligand Non-bond Monitor | 4.78696 | Hydrophobic | Pi-Pi Stacked | :UNL1 | Pi-Orbitals | :UNL1 | Pi-Orbitals |
| 13 | :UNL1 - :UNL1 | Yes | | Ligand Non-bond Monitor | 4.55968 | Hydrophobic | Pi-Pi T-shaped | :UNL1 | Pi-Orbitals | :UNL1 | Pi-Orbitals |

**Annexure 36.** Binding of inhibitors R,R-(+)-**14** with TNFα receptor using ICM-browser. Non-Bonding interactions elucidated using & Discovery Studios Visualizer 21.0.

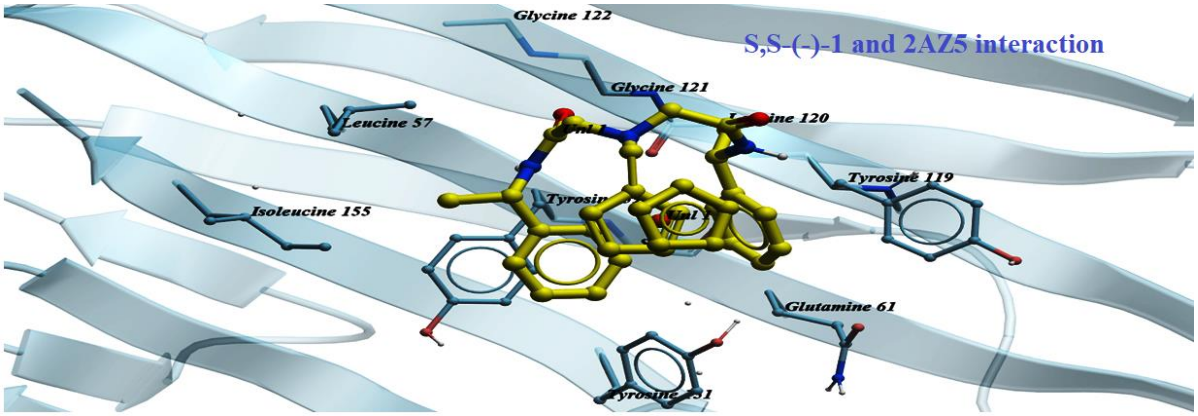


| | Name | Visible | Color | Parent | Distance | Category | Types | From | From Chemistry | To | To Chemistry |
|---|---|---|---|---|---|---|---|---|---|---|---|
| 1 | A:TYR59 - :UNL1 | Yes | | Ligand Non-bond Monitor | 3.79617 | Hydrophobic | Pi-Pi Stacked | A:TYR59 | Pi-Orbitals | :UNL1 | Pi-Orbitals |
| 2 | :UNL1 - :UNL1 | Yes | | Ligand Non-bond Monitor | 3.45097 | Hydrophobic | Pi-Pi Stacked | :UNL1 | Pi-Orbitals | :UNL1 | Pi-Orbitals |
| 3 | :UNL1 - :UNL1 | Yes | | Ligand Non-bond Monitor | 3.96916 | Hydrophobic | Pi-Pi Stacked | :UNL1 | Pi-Orbitals | :UNL1 | Pi-Orbitals |
| 4 | :UNL1 - :UNL1 | Yes | | Ligand Non-bond Monitor | 4.89776 | Hydrophobic | Pi-Pi T-shaped | :UNL1 | Pi-Orbitals | :UNL1 | Pi-Orbitals |
| 5 | :UNL1:C - A:LEU57 | Yes | | Ligand Non-bond Monitor | 3.92845 | Hydrophobic | Alkyl | :UNL1:C | Alkyl | A:LE... | Alkyl |
| 6 | :UNL1:C - A:ILE155 | Yes | | Ligand Non-bond Monitor | 4.79294 | Hydrophobic | Alkyl | :UNL1:C | Alkyl | A:ILE... | Alkyl |
| 7 | A:TYR59 - :UNL1:C | Yes | | Ligand Non-bond Monitor | 4.7321 | Hydrophobic | Pi-Alkyl | A:TYR59 | Pi-Orbitals | :UNL... | Alkyl |

**Annexure 37.** Binding of inhibitors S,S-(-)-**13** with 2AZ5 receptor using ICM-browser. Non-Bonding interactions elucidated using & Discovery Studios Visualizer 21.0.

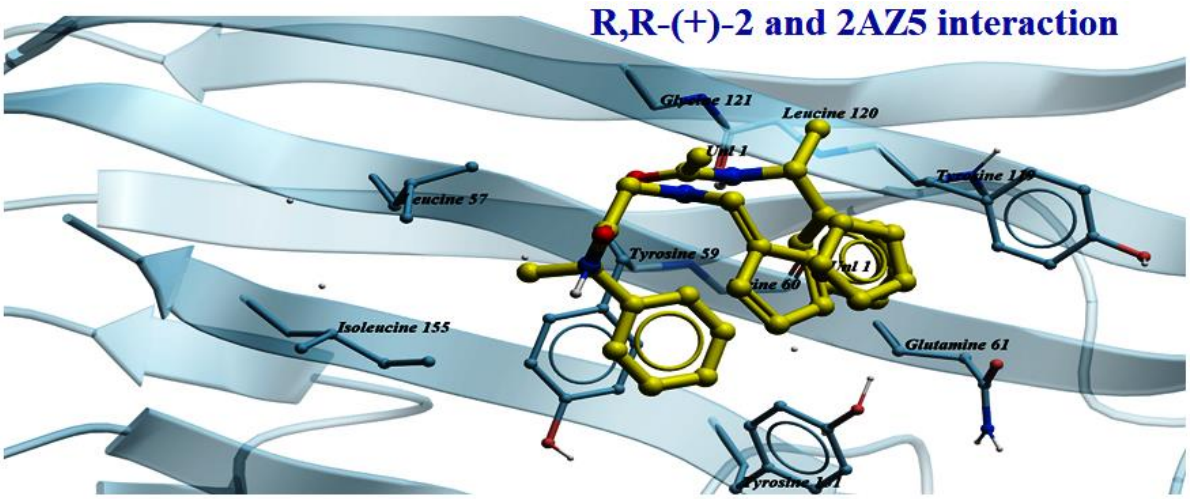


| | Name | Visible | Color | Parent | Distance | Category | Types | From | From Chemistry | To | To Chemistry |
|---|---|---|---|---|---|---|---|---|---|---|---|
| 1 | :UNL1:H - A:LEU120:O | Yes | | Ligand Non-bond Monitor | 2.41179 | Hydrogen Bond | Conventional Hydrogen Bond | :UNL1:H | H-Donor | A:LEU120:O | H-Acceptor |
| 2 | A:GLY121:CA - :UNL1:O | Yes | | Ligand Non-bond Monitor | 3.39494 | Hydrogen Bond | Carbon Hydrogen Bond | A:GLY121:CA | H-Donor | :UNL1:O | H-Acceptor |
| 3 | :UNL1:C - :UNL1:O | Yes | | Ligand Non-bond Monitor | 3.31156 | Hydrogen Bond | Carbon Hydrogen Bond | :UNL1:C | H-Donor | :UNL1:O | H-Acceptor |
| 4 | A:TYR59 - :UNL1 | Yes | | Ligand Non-bond Monitor | 3.75229 | Hydrophobic | Pi-Pi Stacked | A:TYR59 | Pi-Orbitals | :UNL1 | Pi-Orbitals |
| 5 | A:TYR119 - :UNL1 | Yes | | Ligand Non-bond Monitor | 4.83438 | Hydrophobic | Pi-Pi Stacked | A:TYR119 | Pi-Orbitals | :UNL1 | Pi-Orbitals |
| 6 | :UNL1 - :UNL1 | Yes | | Ligand Non-bond Monitor | 3.45125 | Hydrophobic | Pi-Pi Stacked | :UNL1 | Pi-Orbitals | :UNL1 | Pi-Orbitals |
| 7 | :UNL1 - :UNL1 | Yes | | Ligand Non-bond Monitor | 4.11964 | Hydrophobic | Pi-Pi Stacked | :UNL1 | Pi-Orbitals | :UNL1 | Pi-Orbitals |
| 8 | :UNL1 - :UNL1 | Yes | | Ligand Non-bond Monitor | 4.89398 | Hydrophobic | Pi-Pi T-shaped | :UNL1 | Pi-Orbitals | :UNL1 | Pi-Orbitals |
| 9 | :UNL1 - :UNL1 | Yes | | Ligand Non-bond Monitor | 5.24399 | Hydrophobic | Pi-Pi T-shaped | :UNL1 | Pi-Orbitals | :UNL1 | Pi-Orbitals |
| 10 | :UNL1:C - A:LEU57 | Yes | | Ligand Non-bond Monitor | 3.50066 | Hydrophobic | Alkyl | :UNL1:C | Alkyl | A:LEU57 | Alkyl |
| 11 | :UNL1:C - A:ILE155 | Yes | | Ligand Non-bond Monitor | 4.57013 | Hydrophobic | Alkyl | :UNL1:C | Alkyl | A:ILE155 | Alkyl |
| 12 | A:TYR59 - :UNL1:C | Yes | | Ligand Non-bond Monitor | 4.38343 | Hydrophobic | Pi-Alkyl | A:TYR59 | Pi-Orbitals | :UNL1:C | Alkyl |

**Annexure 38.** Binding of inhibitors R,R-(+)-**14** with 2AZ5 receptor using ICM-browser. Non-Bonding interactions elucidated using & Discovery Studios Visualizer 21.0.

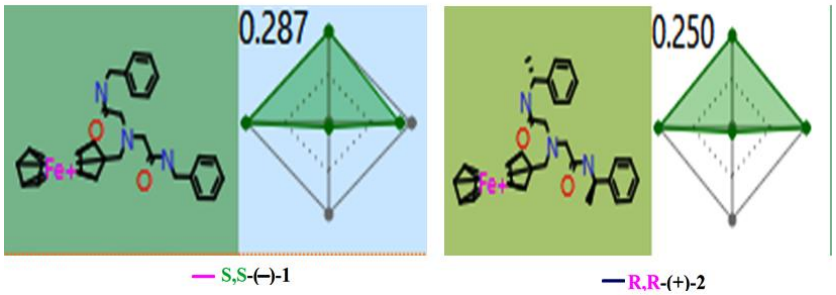


**Annexure 39.** Radial Plot of molecular properties of S,S-(-)-13**,** R,R-(+)-14 using Flare.

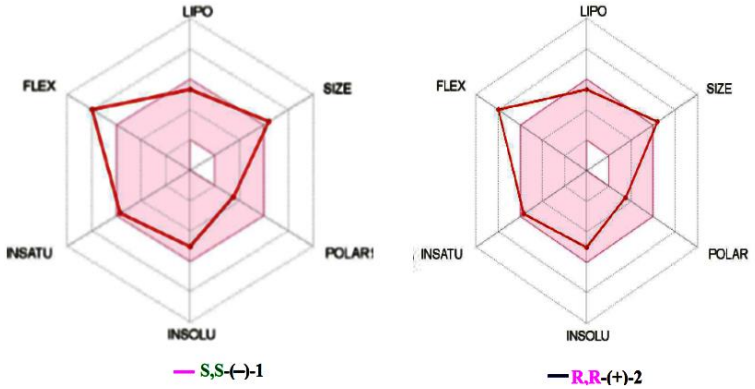


**Annexure 40.** Radial Plot of molecular properties of S,S-(-)-13**,** R,R-(+)-14 using Swiss ADME

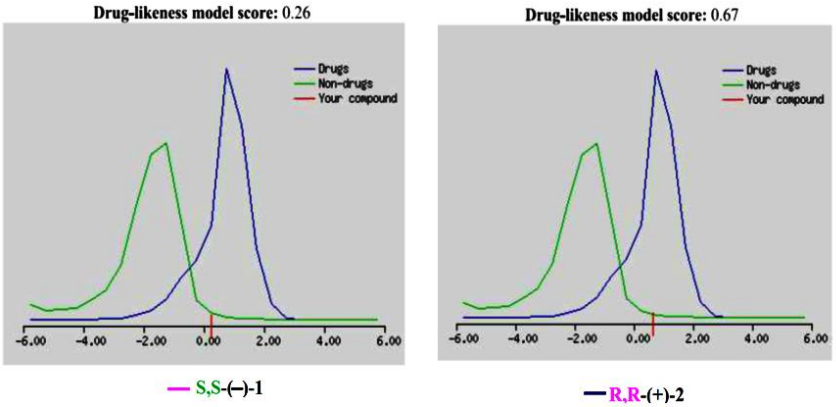


**Annexure 41.** Drug Likeness model evaluation of compounds using Molsoft Webserver:

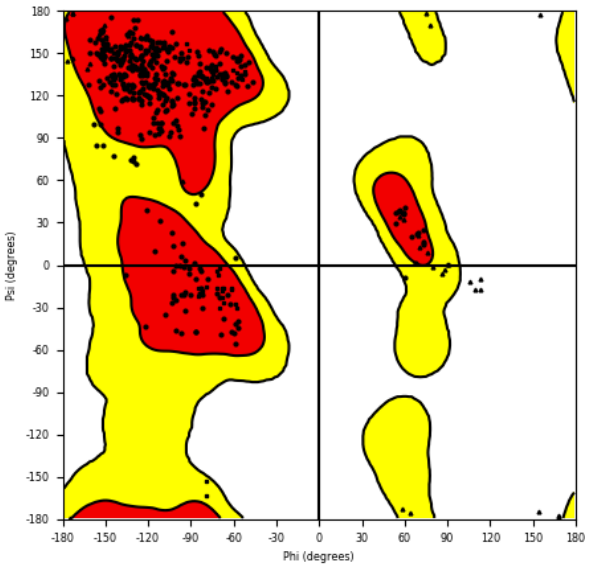


**Annexure 42.** Ramachandran Plot of 1TNF.

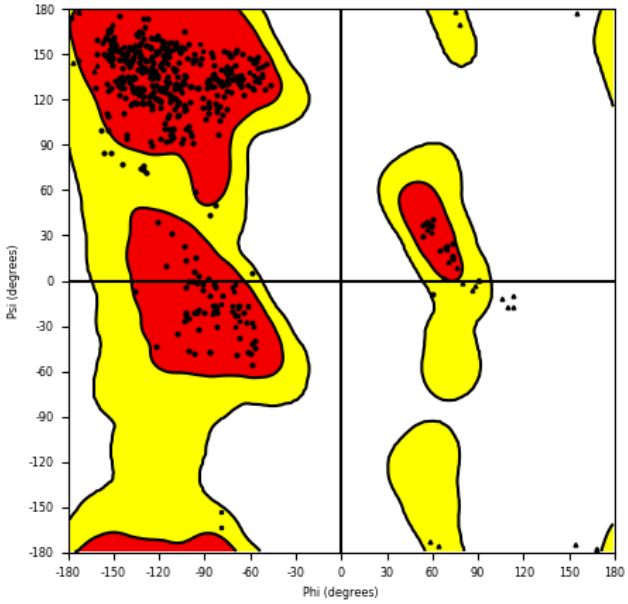


**Annexure 43.** Ramachandran Plot of 2AZ5.